Oxygen Transport Membranes:
A Material Science and Process Engineering Approach

CO_2 O_2

N_2 O_2

O^{2-}

e^{-}

N_2

CO_2

Wei Chen

Oxygen transport membranes:
A material science and process engineering approach

Wei Chen

Graduation committee

Chairman:

     Prof. dr. G. Mul   University of Twente

Promotors:

     Prof. dr. ir. A. Nijmeijer   University of Twente

     Prof. dr. A. J. A. Winnubst   University of Science and Technology of China /

                                          University of Twente

 Committee members:

     Prof. dr. J. Caro   Leibniz University of Hanover

     Prof. dr. C-S. Chen   University of Science and Technology of China

     Prof. dr. ir. M. van Sint-Annaland   Eindhoven University of Technology

     Prof. dr. ing. A. J. H. M. Rijnders   University of Twente

     Dr. ir. A. G. J. van der Ham   University of Twente

OXYGEN TRANSPORT MEMBRANES: A MATERIAL SCIENCE AND PROCESS ENGINEERING APPROACH

DISSERTATION

to obtain

the degree of doctor at the University of Twente,

on the authority of the rector magnificus,

prof. dr. H. Brinksma,

on account of the decision of the graduation committee,

to be publicly defended

on Friday, 16th of May, 2014 at 14:45

by

Wei Chen

born on 19th of December, 1982

in Biyang county, Henan Province, P.R. China

This dissertation has been approved by promotors:

Prof. dr. ir. A. Nijmeijer

Prof. dr. A.J.A. Winnubst

Table of contents

Chapter 1 Introduction

1.1 CO_2 capture and storage

A general consensus exists that the earth is experiencing rapid climate changes, which may cause a redistribution of the global climates. Although it is unknown whether this is beneficial or disastrous for human beings, it will undoubtedly affect human civilization. For example, global warming may cause ice melting in Antarctica and Greenland, which leads to a rise of the sea level and eventually some low altitude cities and countries may disappear.

Although there is no universal agreement about the cause of global warming, many climate scientists assume that the anthropogenic emission of carbon dioxide (CO_2) into the atmosphere is one of the main reasons. In order to reduce CO_2 emissions, it is recommended to apply CO_2 capture and storage (CCS) techniques at large CO_2 point sources. An example of such a source is a fossil fuel-fired power plant. Combined, these fossil fuel-fired power plants account for some 30 % of the worldwide CO_2 emissions. A way of CCS is to compress (100 bar - 150 bar) and transport CO_2 to a storage site, where it is deposited into an underground geological formation for permanent storage. A simple scheme of this process is shown in Figure 1.1.
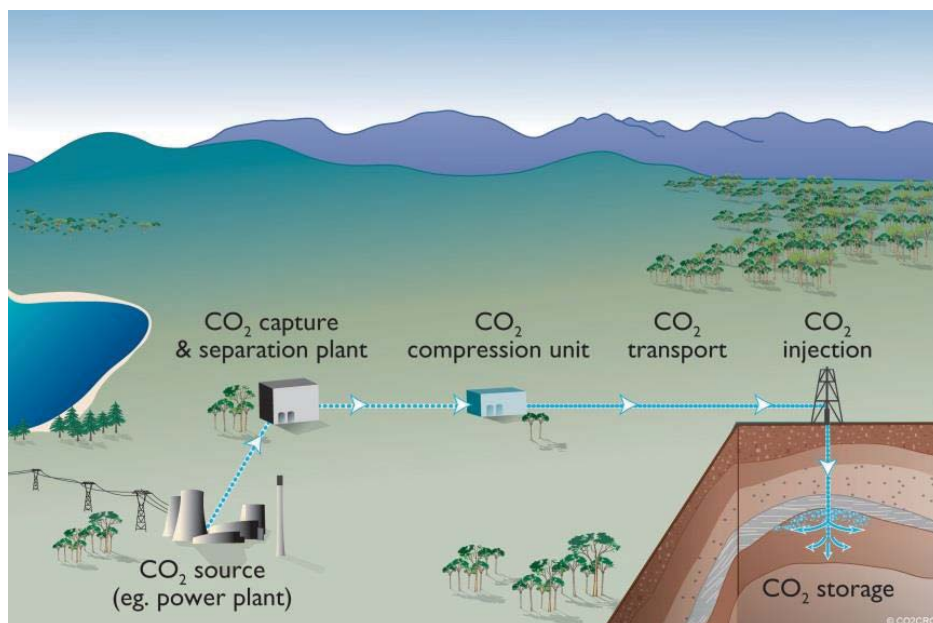
Figure 1.1. Overview of CO_2 capture and storage.

In the past twenty years, many techniques have been developed and demonstrated for CO_2 capture in fossil fuel-fired power plants. Generally, these techniques can be divided into three categories: post-combustion CO_2 capture, oxy-fuel combustion and pre-combustion CO_2 capture.

1.1.1 Post-combustion CO_2 capture

Post-combustion CO_2 capture involves the removal of CO_2 from the flue gas of a combustion process. The advantage of post-combustion CO_2 capture is that it can be implemented to an existing combustion process (as e.g. in a power plant) without making many changes to the plant layout. A disadvantage is that the CO_2 concentration in the flue gas is very low (usually less than 15 mole %) because the main component is N_2 and that the flue gas is at near atmospheric pressure. Several techniques are developed for the separation of CO_2 from the flue gas such as absorption/desorption, membrane separation and cryogenic distillation [1-4].

The most mature technique in the post-combustion CO_2 capture area is the absorption/desorption method as schematically shown in Figure 1.2. CO_2, as present in the flue gas, is chemically bound to a solvent between 40 ºC and 60 ºC. The CO_2 enriched solvent is pumped to a stripper where the temperature is increased to 110 - 130 ºC in order to remove the absorbed CO_2. After desorption the lean solvent is cooled and recycled to the absorption stage via a lean-rich solvent heat exchanger and a cooler to bring the temperature down to the optimal absorption temperature. Many candidates are available to be used as solvent in this process. Monoethanolamine (MEA) is already for many years one of the mostly used solvent to separate CO_2 on an industrial scale. However, with a MEA solution containing 70 wt% of water with high specific heat capacity and latent heat, the CO_2 absorption (at 40 °C) and desorption (at 120 °C) cycles with the MEA solvent are not very energy efficient. The overall energy consumption in this process is $\sim$ 450 kWh/t_{CO_2} (including the CO_2 compression), which accounts to a drop of $\sim$ 30 % in net

efficiency of the power plant.
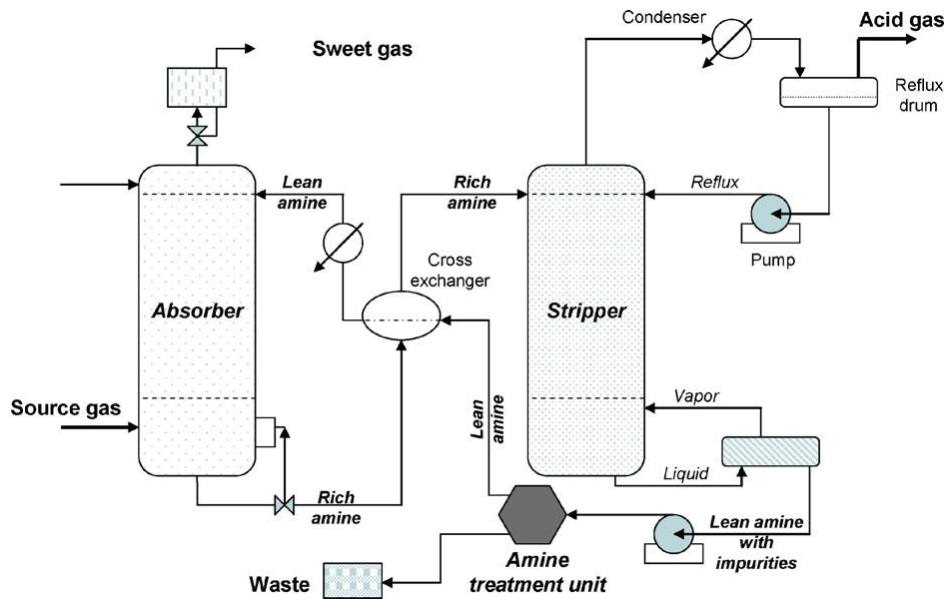
Figure 1.2. A typical monoethanolamine (MEA) absorption process for CO_2 capture from the flue gas [5].

1.1.2 Oxy-fuel combustion

The separation of CO_2 from N_2 as described in section on post-combustion CO_2 capture is avoided in an oxy-fuel combustion process, because here pure oxygen instead of air is used to combust the fossil fuel (see Figure 1.3). In this way the flue gas mainly consists of CO_2 and water vapor. This water vapor is removed by cooling and knocking out the free water, after which the flue gas contains 80-98% CO_2, resulting in an efficient CO_2 capture process. Since the combustion of fossil fuel with pure oxygen can generate temperatures up to 3500 ^oC, which is too high for typical power plant burners, pure oxygen is usually mixed with a part of the flue gas to decrease the oxygen concentration in the burner. It is reported that a composition of 35 % (v/v) oxygen with 65 % (v/v) CO_2 is needed in order to have a similar flame temperature as when air is used [6].
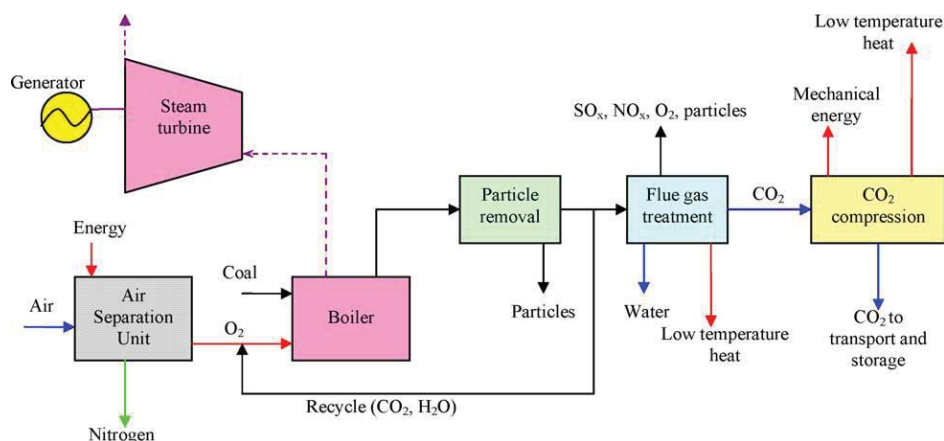
Figure 1.3. Basic principle of oxy-fuel technology [7].

In most cases the oxygen, required for an oxy-fuel combustion process is produced by cryogenic distillation of air, as this technique currently is the only mature way for air separation on a large scale. The energy consumption for oxygen production by means of cryogenic distillation is reported to be 200-240 kWh/t_{O_2} (gaseous oxygen at 1 atmosphere and 15 °C) [8]. This amount of energy results in a decrease of ~10 % in the net efficiency of the power plant. This efficiency drop is much less than that in the MEA based post-combustion CO_2 capture process.

1.1.3 Pre-combustion CO_2 capture

Pre-combustion CO_2 capture is a process that produces a carbon-free fuel before combustion. This process comprises two main steps: fuel reforming and H_2/CO_2 separation, as shown in Figure 1.4.
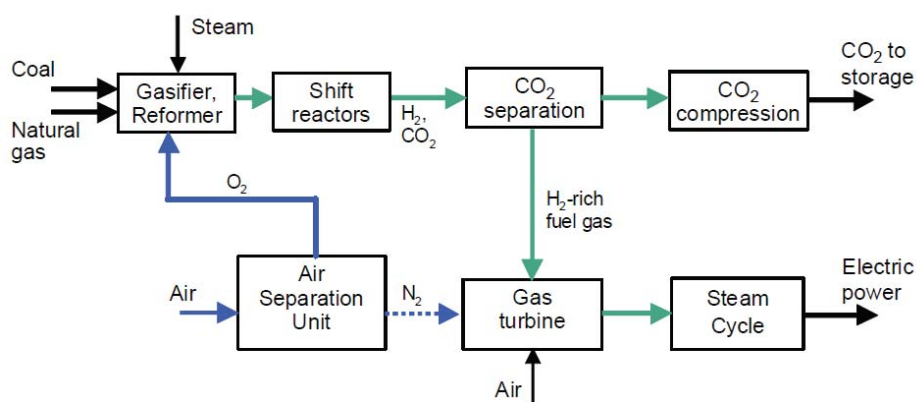
Figure 1.4. Basic principle of pre-combustion process [9].

In the first step fuel is reformed by steam or oxygen or both, and a mixture of H_2

and CO (syngas) is obtained, as shown in eq. (1.1) to (1.3) for methane or coal (assuming that there is only carbon present in the coal). In any case, the produced syngas undergoes a water gas shift reaction where CO is converted to CO_2 and more H_2 is produced, as shown in eq. (1.4).

Steam reforming of methane

$$CH_4 + H_2O \leftrightarrow CO + 3H_2 \qquad \Delta H_r^o = 250 \text{ kJ/mol} \qquad (1.1)$$

Partial oxidation of methane

$$CH_4 + O_2 \leftrightarrow CO + 2H_2 \qquad \Delta H_r^o = -36 \text{ kJ/mol} \qquad (1.2)$$

Coal gasification

$$4C + 2H_2O + O_2 \leftrightarrow 4CO + 2H_2 \qquad \Delta H_r^o = 130 \text{ kJ/mol} \qquad (1.3)$$

Water gas shift reaction

$$CO + H_2O \leftrightarrow CO_2 + H_2 \qquad \Delta H_r^o = 2.8 \text{ kJ/mol} \qquad (1.4)$$
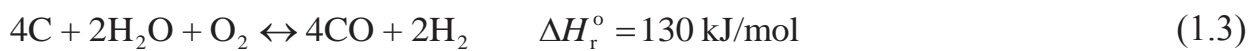
After these reactions H_2 must be separated from CO_2. This separation can either be done by a conventional CO_2 absorption (solvent based) or adsorption (pressure swing adsorption) method or by using H_2- or CO_2 selective membranes. In the case of membrane separation, the separation process can be coupled with the water gas shift reaction in one membrane reactor. In this way the reaction, as shown in eq. (1.4), can be shifted to the right by simultaneously removing the produced H_2 or CO_2.

After the gas separation step, the produced H_2 is combusted with air in a gas turbine to generate electricity, and the exhaust gas is used to heat a steam turbine cycle for further electricity generation. This process is called integrated gasification combined cycle (IGCC) with CO_2 capture if coal is used as the fuel, and natural gas combined cycle (NGCC) with CO_2 capture if natural gas is used as the fuel.

One may note that an air separation unit is also needed in some of the pre-combustion CO_2 capture line-ups, which is similar to an oxy-fuel combustion process. The difference between these two processes is that the amount oxygen needed, e.g., the oxygen necessary for partial oxidation of methane to CO and H_2 is

only 25 % of that in a complete oxidation of methane to CO_2 and H_2O.

1.2 Oxygen transport membranes integrated in oxy-fuel combustion

As mentioned above, the oxygen needed for the oxy-fuel combustion process is produced by cryogenic distillation of air, which is an energy-intensive process. In order to reduce the energy consumption for oxygen production, it has been proposed to use dense ceramic oxygen transport membranes and it is assumed that the energy consumption in this process can be significantly reduced [10].

1.2.1 Oxygen transport through a dense ceramic membrane

A dense ceramic oxygen transport membrane comprises different metal oxides. A key feature of these metal oxides is that they are not stoichiometric at room or elevated temperature. Some of the oxygen sites in the crystal structure are not occupied, which are called oxygen vacancies. The lattice oxygen around the oxygen vacancies may hop randomly from their original sites to the oxygen vacancies if they possess sufficient thermal energy to overcome the energy barrier.

If the two sides of the membrane are exposed to different oxygen partial pressures (P_{O_2}), the random hopping of oxygen ions has a statistical direction from the high P_{O_2} side to the low P_{O_2} side. Since oxygen ions are negatively charged, a counter-transport of electronic charge carriers is required to maintain charge neutrality in the membrane. This electronic current can be realized either by an external circuit if the membrane material is purely ionic conducting or by simultaneous transport of electrons if the membrane material is mixed ionic-electronic conducting. These two routes are schematically shown in Figure 1.5. Some research is performed on the first configuration [11, 12], but most studies on oxygen transport membranes are focused on the second configuration, because here no external electrical circuit is required, resulting in a far more simple membrane system [13]. In this thesis, the discussion on oxygen transport is based on these mixed ion-

electron conducting (MIEC) membranes without further notation.
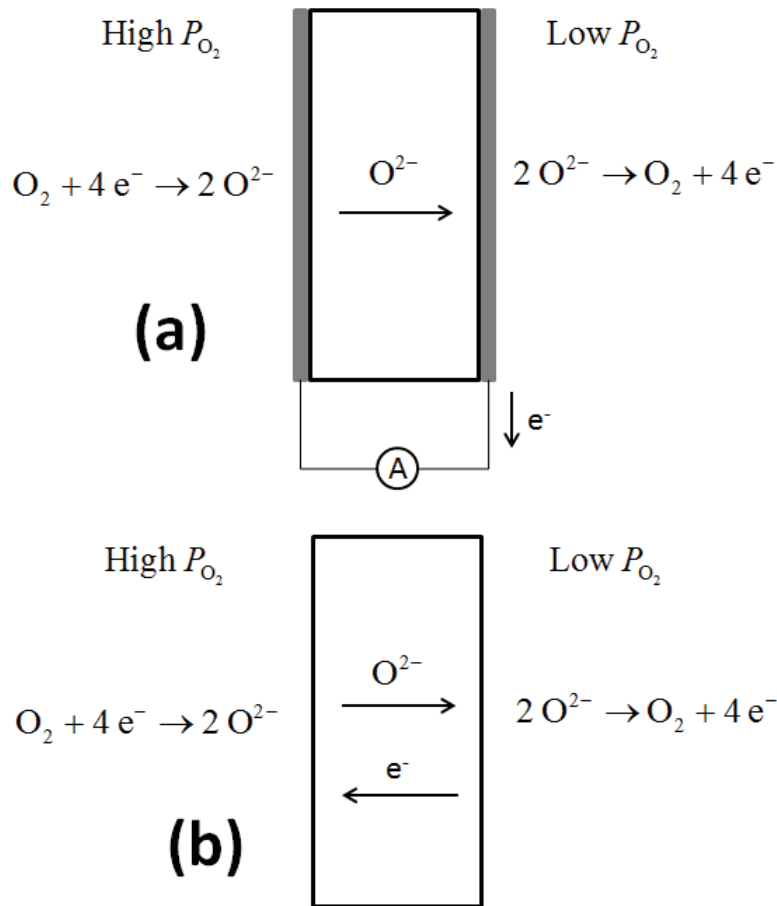
Figure 1.5. Configuration of oxygen transport membrane with (a) and without (b) an external circuit.

The oxygen transport through a MIEC membrane comprises of 3 steps, i.e.: (1) the surface-exchange reaction on the membrane surface at the high P_{O_2} side; (2) the simultaneous diffusion of charged species in the bulk phase and (3) the surface-exchange reaction on the membrane surface at the low P_{O_2} side. The slowest of these three steps determines the overall oxygen flux, which is called rate limiting step. The rate limiting step depends on membrane material, operating conditions and membrane geometry. Bouwmeester et al. [14] use the concept of critical thickness (L_c) to distinguish the rate limiting steps:

$$L_{\mathrm{c}} = \frac{D_{\mathrm{i}}}{k} \tag{1.5}$$

where D_{i} is the self-diffusion coefficient of oxygen anions and k is the surface exchange coefficient. When the membrane thickness (L) is much higher than L_{c}, bulk diffusion dominates oxygen transport; when L is much lower than L_{c}, surface-exchange reactions are important.

If the oxygen transport through the membrane is controlled by bulk diffusion, the oxygen flux can be described by the Wagner equation [15]:

$$j_{\mathrm{O}_2} = -\frac{RT}{(4F)^2 L} \int_{\ln P'_{\mathrm{O}_2}}^{\ln P''_{\mathrm{O}_2}} \frac{\sigma_{\mathrm{el}}\sigma_{\mathrm{ion}}}{\sigma_{\mathrm{el}} + \sigma_{\mathrm{ion}}} d \ln P_{\mathrm{O}_2} \tag{1.6}$$

where j_{O_2} is the oxygen permeation flux, R the gas constant, T absolute temperature, F Faraday constant, L membrane thickness, σ_{ion} oxygen ionic conductivity, σ_{el} electronic conductivity and P_{O_2} is the oxygen partial pressure. For most MIEC membranes, the electronic conductivity σ_{el} is often two orders of magnitude higher than σ_{ion}. Therefore eq. 1.6 can be rewritten as:

$$j_{\mathrm{O}_2} = -\frac{RT}{(4F)^2 L} \int_{\ln P'_{\mathrm{O}_2}}^{\ln P''_{\mathrm{O}_2}} \sigma_{\mathrm{ion}} \, d \ln P_{\mathrm{O}_2} \tag{1.7}$$

If the oxygen surface exchange is the rate limiting step, i.e. $L \ll L_{\mathrm{c}}$, only some empirical relations have been found to predict the oxygen flux [16], namely:

$$J_{\mathrm{O}_2} = \alpha(P'^{5/8}_{\mathrm{O}_2} - P''^{5/8}_{\mathrm{O}_2}) \tag{1.8}$$

or

$$J_{\mathrm{O}_2} = \alpha(P'^{1/4}_{\mathrm{O}_2} - P''^{1/4}_{\mathrm{O}_2}) \tag{1.9}$$

These equations have been successfully used to describe the oxygen flux within the erbia-stabilized bismuth oxide system although physical meaning is not very clear [16].

1.2.2 Integration of oxygen transport membranes in the oxy-fuel combustion process

The integration of oxygen transport membranes in the oxy-fuel combustion process can be applied in two ways, as illustrated in Figure 1.6. In the first way (Figure 1.6a), air is used as the feed gas, nitrogen is retained and pure oxygen is produced. There are three gas streams in this operation mode, and thus it is called 3-end mode. In the second way (Figure 1.6b), a sweep gas is used to carry away the permeated oxygen, and there are four gas streams in this operation mode, so it is called 4-end mode.
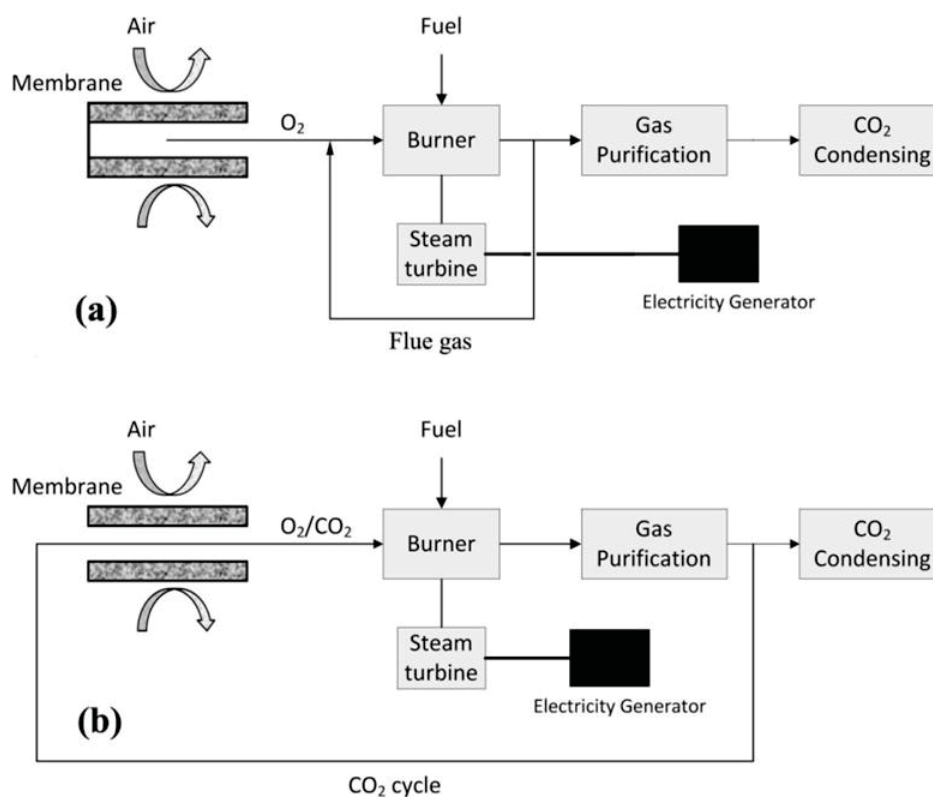
Figure 1.6. Illustration of membrane-integrated oxy-fuel combustion process in 3-end (a) and 4-end mode (b).

In the 3-end mode either the feed (air) side of the membrane is compressed or at the permeate side of the membrane a vacuum is applied or a combination of these two methods. In this way a P_{O_2} gradient is created across the membrane. Pure oxygen, as separated by the membrane, is diluted by recycled flue gas to avoid extremely high temperatures during of fuel combustion.

In the 4-end mode, a sweep gas is used to carry the permeated oxygen and also to decrease the P_{O_2} at the sweep side for creating a P_{O_2} gradient across the membrane. In this 4-end mode a higher P_{O_2} gradient can be created if compared with the 3-end mode. For example, assume, for both modes, that the total pressure is 10 bar at the feed side (air) and 1 bar at the permeate side of the membrane. The P_{O_2} at

the feed side is identical for both cases, i.e. ~2.1 bar. While the P_{O_2} at the permeate side is different. In the 3-end mode, the P_{O_2} is equal to the total pressure, i.e. 1 bar. In the 4-end mode the P_{O_2} is lower than the total pressure because there is also sweep gas. Assume that the oxygen mole fraction is 0.5, then the P_{O_2} is only 0.5 bar. Thus the P_{O_2} difference in 3-end mode is 1.1 bar, while 1.6 bar in the 4-end mode. This difference leads to a fact that the required pressure for air compression is lower in the 4-end mode, which is one of the biggest advantages of the 4-end mode.

1.3 State of the art membranes for oxy-fuel combustion

There are two general requirements for the membranes to be used in the oxy-fuel combustion process: stability and permeability.

In the 3-end mode membranes are only exposed to nitrogen and oxygen, and most of the MIEC membranes are chemically stable in these gases. Besides chemical stability phase stability has to be considered when using MIEC membranes. The phase stability is affected by temperature and P_{O_2}. $Ba_{0.5}Sr_{0.5}Co_{0.8}Fe_{0.2}O_{3-\delta}$ (BSCF) and $SrCo_{0.8}Fe_{0.2}O_{3-\delta}$ (SCF) are considered for air separation application because of their high oxygen fluxes [17-20]. Oxygen flux values for BSCF are reported as high as ~1.6 ml/min under a P_{O_2} gradient of 0.21/0.05 bar at 950 ºC, with a membrane thickness of 1.5 mm [20]. Similar oxygen flux data are given for SCF. BSCF suffers from a slow phase transition from a pure cubic structure to a mixture of a cubic and a hexagonal structure below ~825 ºC [21, 22], which causes a decline in oxygen flux with time. For SCF a transition from the cubic perovskite to the lower conducting orthorhombic brownmillerite phase has been found when the temperature is below 790 ºC and the P_{O_2} is less than 10^{-2} bar [18, 23, 24]. Therefore, in order to use these membranes, the operation temperature should be above the phase transition temperature, i.e. 825 ºC and 790 ºC for resp. BSCF and SCF. An alternative way is to

stabilize the high-conducting perovskite phase to a lower temperature by doping. Yakovlev et al. reported that doping of 3 mol% Zr- at the B-site (Co/Fe site) of BSCF can stabilize the cubic structure down to 800 °C [25]. Chen et al. [26] have also found that ~4 mol% Zr-doping at the B-site can stabilize SCF to ~700 °C in a P_{O_2} of 10^{-4} bar.

For membranes, to be used in the 4-end mode, one of the options is to use CO_2, which is known as an acid gas, as the sweep gas. As most of the MIEC oxides contain alkaline-earth elements (Ca, Sr or Ba) a carbonation reaction occurs when these membranes are exposed to a CO_2-containing atmosphere. This reaction results in the formation of an alkaline-earth carbonate layer, which is impermeable for oxygen, on the membrane surface, resulting in a decline in oxygen flux or even to a non-permeating membrane. Changing the sweep gas from helium to CO_2 results in an immediate stagnation of the oxygen flux for BSCF membranes [27]. It is also found that the oxygen flux of SCF membrane decreases to almost zero in 80 hours when CO_2 is used as sweep [28]. In recent years, more and more research has been focused on the development of CO_2-resistant membranes. Kilner et al. reported that $La_{0.6}Sr_{0.4}Co_{0.2}Fe_{0.8}O_{3-\delta}$ (LSCF) membranes have a high CO_2 resistance [29]. In [30] it is reported that LSCF-based hollow fibre membranes (membrane thickness ~200 μm) show a stable oxygen flux of ~0.8 ml/min at 950 °C when CO_2 is used as sweep gas. Wei et al. have developed K_2NiF_4-type $(Pr_{0.9}La_{0.1})_2(Ni_{0.74}Cu_{0.21}Ga_{0.05})O_{4+\delta}$ (PLNCG) membranes which show good CO_2 resistance and similar oxygen flux as LSCF membranes [31, 32]. Chen et al. fabricated several dual phase membranes such as $La_{0.8}Sr_{0.2}MnO_{3-\delta}$ (LSM)-$Zr_{0.84}Y_{0.16}O_{1.92}$ (YSZ) and LSM-$Ce_{0.8}Sm_{0.2}O_{2-\delta}$ (SDC) [33, 34], which show excellent CO_2 resistance but rather low oxygen flux.

Besides the membrane stability, the oxygen permeability of the membranes is also important. A summary on oxygen flux data of different membranes has been given by Sunarso et al [13]. In principle, the higher of the oxygen permeability, the less membrane area is needed for a certain air separation duty, thus the cost for air

separation will be reduced. Generally, there are two ways to increase the oxygen flux if the membrane material has already been chosen, i.e. decrease the membrane thickness or increase the surface exchange rate. According to eq. 1.6, the oxygen flux is inversely proportional to the membrane thickness if bulk diffusion predominates the oxygen transport. For example, a supported BSCF thin film (70 µm thick) shows an oxygen flux of ~ 6 ml/min at 950 °C [35], which is much higher than that of a 1.5 mm thick BSCF membrane (~1.6 ml/min) [20]. One may notice that the decrease in thickness by a factor of ~20 only results in an increase in oxygen flux by a factor of ~4. This relative small increase in oxygen flux is possibly caused by the change in the rate limiting step. At a membrane thickness of 70 µm, or maybe even at a higher thickness, oxygen transport is controlled by the surface exchange reaction. So there is a limit in increasing the oxygen flux by decreasing the membrane thickness. If the flux is controlled by the oxygen surface exchange rate, a porous layer can be applied on the dense membrane to increase the total surface area and thus increase the surface exchange rate. The coated layer can be the same material as the membrane or a different, dedicated, material. In the latter case materials with a higher oxygen exchange rate are usually considered.

1.4 Scope of the thesis

The objective of the research, as described in this thesis, is to investigate the feasibility of integrating MIEC membranes into the oxy-fuel combustion process for CO_2 capture. This includes the fabrication of appropriate membrane materials and the design of a membrane-integrated oxy-fuel process.

Chapter 2 and 3 are focused on the characterization of the membrane properties. In chapter 2, a novel, simple and easy way to determine the oxygen non-stoichiometry of the perovskite materials by a carbonation process is developed. Chapter 3 presents a numerical method to more accurately measure the oxygen ionic conductivity of the MIEC membranes, using data obtained from a standard laboratory permeation set-up. In chapter 4, a CO_2 resistant SCF membrane has been

developed by partial substitution of Co/Fe by Ta, but at the cost of a reduction in oxygen flux by ~ 30%. In chapter 5 it is found that the CO_2 resistance of SCF membranes is greatly affected by the ambient P_{O_2}, and it is possible to avoid CO_2 poisoning of the membrane by increasing the ambient P_{O_2}, rather than by doping. Chapter 6 gives a design of a MIEC membrane based oxy-fuel combustion process as simulated in UniSim®. Finally, in chapter 7, recommendations and outlook for future research work are given.

References

[1] M.J. Tuinier, M. van Sint Annaland, J.A.M. Kuipers, A novel process for cryogenic CO_2 capture using dynamically operated packed beds—An experimental and numerical study, Int J Greenh Gas Con, 5 (2011) 694-701.

[2] T.C. Merkel, H. Lin, X. Wei, R. Baker, Power plant post-combustion carbon dioxide capture: An opportunity for membranes, Journal of Membrane Science, 359 (2010) 126-139.

[3] M.J. Tuinier, M. van Sint Annaland, G.J. Kramer, J.A.M. Kuipers, Cryogenic capture using dynamically operated packed beds, Chem Eng Sci, 65 (2010) 114-119.

[4] J. Blamey, E.J. Anthony, J. Wang, P.S. Fennell, The calcium looping cycle for large-scale CO_2 capture, Progress in Energy and Combustion Science, 36 (2010) 260-279.

[5] L. Dumée, C. Scholes, G. Stevens, S. Kentish, Purification of aqueous amine solvents used in post combustion CO_2 capture: A review, Int J Greenh Gas Con, 10 (2012) 443-455.

[6] E. Croiset, K. Thambimuthu, A. Palmer, Coal combustion in O_2/CO_2 mixtures compared with air, The Canadian Journal of Chemical Engineering, 78 (2000) 402-407.

[7] I. Hadjipaschalis, G. Kourtis, A. Poullikkas, Assessment of oxyfuel power generation technologies, Renewable and Sustainable Energy Reviews, 13 (2009) 2637-2644.

[8] A. Darde, R. Prabhakar, J.-P. Tranier, N. Perrin, Air separation and flue gas compression and purification units for oxy-coal combustion systems, Energy Procedia, 1 (2009) 527-534.

[9] N.A. Røkke, Ø. Langørgen, Enabling pre-combustion plants—the DECARBit project, Energy Procedia, 1 (2009) 1435-1442.

[10] P.N. Dyer, R.E. Richards, S.L. Russek, D.M. Taylor, Ion transport membrane technology for oxygen separation and syngas production, Solid State Ionics, 134 (2000) 21-33.

[11] K. Zhang, L. Liu, Z. Shao, R. Xu, J.C. Diniz da Costa, S. Wang, S. Liu, Robust ion-transporting ceramic membrane with an internal short circuit for oxygen production, Journal of Materials

Chemistry A, 1 (2013) 9150-9156.

[12] K. Zhang, Z. Shao, C. Li, S. Liu, Novel CO_2-tolerant ion-transporting ceramic membranes with an external short circuit for oxygen separation at intermediate temperatures, Energ Environ Sci, 5 (2012) 5257-5264.

[13] J. Sunarso, S. Baumann, J.M. Serra, W.A. Meulenberg, S. Liu, Y.S. Lin, J.C.D. da Costa, Mixed ionic-electronic conducting (MIEC) ceramic-based membranes for oxygen separation, Journal of Membrane Science, 320 (2008) 13-41.

[14] H.J.M. Bouwmeester, H. Kruidhof, A.J. Burggraaf, Importance of the surface exchange kinetics as rate limiting step in oxygen permeation through mixed-conducting oxides, Solid State Ionics, 72 (1994) 185-194.

[15] H.J.M. Bouwmeester, A.J. Burggraaf, The CRC Handbook of Solid State Electrochemistry, 1 ed., CRC Press, 1996.

[16] H.J.M. Bouwmeester, H. Kruidhof, A.J. Burggraaf, P.J. Gellings, Oxygen semipermeability of erbia-stabilized bismuth oxide, Solid State Ionics, 53–56, Part 1 (1992) 460-468.

[17] Z.P. Shao, W.S. Yang, Y. Cong, H. Dong, J.H. Tong, G.X. Xiong, Investigation of the permeation behavior and stability of a $Ba_{0.5}Sr_{0.5}Co_{0.8}Fe_{0.2}O_{3-\delta}$ oxygen membrane, Journal of Membrane Science, 172 (2000) 177-188.

[18] L. Qiu, T.H. Lee, L.M. Liu, Y.L. Yang, A.J. Jacobson, Oxygen Permeation Studies of $SrCo_{0.8}Fe_{0.2}O_{3-\delta}$, Solid State Ionics, 76 (1995) 321-329.

[19] J. Tong, W. Yang, B. Zhu, R. Cai, Investigation of ideal zirconium-doped perovskite-type ceramic membrane materials for oxygen separation, Journal of Membrane Science, 203 (2002) 175-189.

[20] Z. Shao, G. Xiong, H. Dong, W. Yang, L. Lin, Synthesis, oxygen permeation study and membrane performance of a $Ba_{0.5}Sr_{0.5}Co_{0.8}Fe_{0.2}O_{3-\delta}$ oxygen-permeable dense ceramic reactor for partial oxidation of methane to syngas, Sep Purif Technol, 25 (2001) 97-116.

[21] S. Svarcova, K. Wiik, J. Tolchard, H.J.M. Bouwmeester, T. Grande, Structural instability of cubic perovskite $Ba_xSr_{1-x}Co_{1-y}Fe_yO_{3-\delta}$, Solid State Ionics, 178 (2008) 1787-1791.

[22] M. Arnold, T.M. Gesing, J. Martynczuk, A. Feldhoff, Correlation of the Formation and the Decomposition Process of the BSCF Perovskite at Intermediate Temperatures, Chem Mater, 20 (2008) 5851-5858.

[23] H. Kruidhof, H.J.M. Bouwmeester, R.H.E. v. Doorn, A.J. Burggraaf, Influence of order-disorder transitions on oxygen permeability through selected nonstoichiometric perovskite-type oxides, Solid State Ionics, 63–65 (1993) 816-822.

[24] A.A. Yaremehenko, V.V. Kharton, M. Avdeev, A.L. Shaula, F.M.B. Marques, Oxygen permeability, thermal expansion and stability of $SrCo_{0.8}Fe_{0.2}O_{3-\delta}$-$SrAl_2O_4$ Composites, Solid State Ionics, 178 (2007) 1205-1217.

[25] S. Yakovlev, C.-Y. Yoo, S. Fang, H.J.M. Bouwmeester, Phase transformation and oxygen equilibration kinetics of pure and Zr-doped $Ba_{0.5}Sr_{0.5}Co_{0.8}Fe_{0.2}O_{3-\delta}$ perovskite oxide probed by electrical conductivity relaxation, Applied Physics Letters, 96 (2010) -.

[26] W. Chen, Y.B. Zuo, C.S. Chen, A.J.A. Winnubst, Effect of Zr^{4+} doping on the oxygen stoichiometry and phase stability of $SrCo_{0.8}Fe_{0.2}O_{3-\delta}$ oxygen separation membrane, Solid State Ionics, 181 (2010) 971-975.

[27] M. Arnold, H.H. Wang, A. Feldhoff, Influence of CO_2 on the oxygen permeation performance and the microstructure of perovskite-type $(Ba_{0.5}Sr_{0.5})(Co_{0.8}Fe_{0.2})O_{3-\delta}$ membranes, Journal of Membrane Science, 293 (2007) 44-52.

[28] Q. Zeng, Y.B. Zu, C.G. Fan, C.S. Chen, CO_2-tolerant oxygen separation membranes targeting CO_2 capture application, Journal of Membrane Science, 335 (2009) 140-144.

[29] S.J. Benson, D. Waller, J.A. Kilner, Degradation of $La_{0.6}Sr_{0.4}Fe_{0.8}Co_{0.2}O_{3-\delta}$ in carbon dioxide and water atmospheres, J Electrochem Soc, 146 (1999) 1305-1309.

[30] X. Tan, N. Liu, B. Meng, J. Sunarso, K. Zhang, S. Liu, Oxygen permeation behavior of $La_{0.6}Sr_{0.4}Co_{0.8}Fe_{0.2}O_3$ hollow fibre membranes with highly concentrated CO_2 exposure, Journal of Membrane Science, 389 (2012) 216-222.

[31] Y.Y. Wei, J. Tang, L.Y. Zhou, J. Xue, Z. Li, H.H. Wang, Oxygen separation through U-shaped hollow fiber membrane using pure CO_2 as sweep gas, Aiche J, 58 (2012) 2856-2864.

[32] Y. Wei, O. Ravkina, T. Klande, H. Wang, A. Feldhoff, Effect of CO_2 and SO_2 on oxygen permeation and microstructure of $(Pr_{0.9}La_{0.1})_2(Ni_{0.74}Cu_{0.21}Ga_{0.05})O_{4+\delta}$ membranes, Journal of Membrane Science, 429 (2013) 147-154.

[33] W. Li, T.-F. Tian, F.-Y. Shi, Y.-S. Wang, C.-S. Chen, $Ce_{0.8}Sm_{0.2}O_{2-\delta}-La_{0.8}Sr_{0.2}MnO_{3-\delta}$ Dual-Phase Composite Hollow Fiber Membrane for Oxygen Separation, Ind Eng Chem Res, 48 (2009) 5789-5793.

[34] W. Li, J.J. Liu, C.S. Chen, Hollow fiber membrane of yttrium-stabilized zirconia and strontium-doped lanthanum manganite dual-phase composite for oxygen separation, Journal of Membrane Science, 340 (2009) 266-271.

[35] S. Baumann, J.M. Serra, M.P. Lobera, S. Escolástico, F. Schulze-Küppers, W.A. Meulenberg, Ultrahigh oxygen permeation flux through supported $Ba_{0.5}Sr_{0.5}Co_{0.8}Fe_{0.2}O_{3-\delta}$ membranes, Journal of Membrane Science, 377 (2011) 198-205.

Chapter 2 Oxygen non-stoichiometry determination of perovskite materials by a carbonation process

Abstract:

A new and easy method is developed to determine the oxygen non-stoichiometry of perovskite materials under equilibrium conditions. The method is based on the complete decomposition of the powder to stoichiometric metal oxides and/or metal carbonates by using CO_2 as reacting gas. The oxygen non-stoichiometry is calculated from the mass change caused by this reaction. Its applicability is demonstrated by using $SrCoO_{3-\delta}$, $BaCoO_{3-\delta}$, $BaFeO_{3-\delta}$ and $BaCeO_{3-\delta}$ as representative materials. The oxygen non-stoichiometry (δ) values at 950 ˚C in air were determined as 0.48, 0.36, 0.43 and 0.03 respectively. These values can be used as reference points for oxygen non-stoichiometry analysis at other temperatures.

2.1 Introduction

An important issue in defect chemistry is the study of the oxygen non-stoichiometry of metal oxides, especially for materials with high oxygen deficiency [1-3]. Examples are several perovskite systems with general formula $ABO_{3-\delta}$, where δ represents the oxygen non-stoichiometry value. Several methods are developed to measure this oxygen non-stoichiometry as function of temperature and oxygen partial pressure [4]. All these methods are based on the analysis of the change in oxygen non-stoichiometry $\Delta(\delta)$ as function of temperature or oxygen partial pressure, which are briefly reviewed as following.

For the measurement of $\Delta(\delta)$ thermal gravimetric analysis (TGA) is the most popular and frequently used method [5]. In this method it is assumed that the only reason for mass change is the release or incorporation of oxygen at varying temperatures or oxygen partial pressures. The mass change of the sample can then easily be converted to $\Delta(\delta)$. Another technique to measure $\Delta(\delta)$ is coulometric titration [4], where samples are placed in a sealed vessel made from yttria-stabilized zirconia (YSZ). One part of the YSZ (connected with electrolytes) is used as an oxygen pump, while another separate part is used as oxygen sensor. A defined amount of oxygen is pumped out/in quantitatively by applying a fixed electrical potential over the pump part of the vessel. The change in oxygen partial pressure in the vessel is not only related to the amount of oxygen removed by pumping, because oxygen is also released from the powder sample during pumping. From the difference between the measured oxygen partial pressure in the vessel and the amount of oxygen pumped out $\Delta(\delta)$ can be calculated. A method similar to coulometric titration is solid electrolyte coulometry (SEC). The difference however is that in the latter case the experiment can be done in open systems or in a gas flowing mode. Details can be found in Teske, Bode and Vashook's work [6-8].

It should be mentioned that in order to determine the absolute oxygen non-stoichiometry for both the TGA and the coulometric titration method, an absolute

value of δ at a fixed temperature and oxygen partial pressure is necessary (called reference point). A traditional way to obtain such a reference point is iodometric titration [9]. Here samples are dissolved in HCl with the presence of an excess of KI and heated in an oxygen-free (nitrogen) environment. During this process, the transition metal ions (such as Co^{3+}, Co^{4+}, Fe^{3+}, Fe^{4+}) were reduced, and I^- was oxidized to I_2. The amount of I_2 released is quantitatively determined by redox titration using $Na_2S_2O_3$ as the titrant agent. The oxygen non-stoichiometry was calculated based on the amount of I_2 formed. Another way to measure the reference point is hydrogen reduction [10], by making use of the phenomenon that at elevated temperatures (~700 ºC) several cations in oxides will react with hydrogen to the metallic state or to the metal oxides, and the absolute content of oxygen in these oxides is determined by monitoring the mass loss of the sample in a hydrogen containing gas with a TGA setup, while the final products are determined by X-Ray Diffraction (XRD).

In this paper a new and convenient method is reported to measure the absolute oxygen content (3-δ) of perovskite materials at a thermodynamic equilibrium state. Since several metal oxides, especially perovskite structured oxides, contain alkaline earth metals, which are very sensitive to CO_2, these materials easily decompose at elevated temperature in a CO_2 containing atmosphere [11]. After complete reaction and obtaining stoichiometric products the oxygen non-stoichiometry can easily be calculated. To demonstrate this method, $SrCoO_{3-\delta}$, $BaCoO_{3-\delta}$, $BaFeO_{3-\delta}$ and $BaCeO_{3-\delta}$ were chosen as representative materials in this study, because of their relative simple compositions, while products after reaction with CO_2 can easily be identified. However, it is expected that this method can also successfully be applied for other perovskite materials with well-defined reaction products.

2.2 Experimental

$SrCoO_{3-\delta}$, $BaCoO_{3-\delta}$, $BaFeO_{3-\delta}$ and $BaCeO_{3-\delta}$ were synthesized using an EDTA complexation/pyrolysis process as described in detail in [12]. In this work metal

nitrates were dissolved in demineralized water under stirring at a stoichiometric ratio. EDTA, dissolved in ammonia, was added and after chelating for several minutes citric acid was added. The molar ratio of total metal ions : citric acid : EDTA was 1.0 : 1.5 : 1.0. The pH value of the solution was adjusted to 6 by adding ammonia. Subsequently NH_4NO_3 was added as an ignition aid at an amount of 100 g NH_4NO_3 per 0.1 mole of metal ions. This final solution was heated at 120-150 °C under stirring to evaporate water until it changed into a viscous gel, which was transferred to a stainless steel vessel and heated on a hot plate at a temperature of around 500 °C, while a vigorous combustion took place, resulting in a fluffy powder. The powder was collected and calcined in a room furnace at 950 °C for 5 hours at a heating and cooling rate of 3 °C/min.

Isothermal gravimetric analyses were carried out on a Netzsch TG 449 F3 Jupiter®. About 20 mg of powder was weighed in an alumina crucible and placed in the TGA setup. The temperature was increased to 950 °C in flowing air (79 ml/min N_2 and 21 ml/min O_2) at a heating rate of 10 °C/min. The system was isothermally hold in air at 950 °C for 1 hour in order to reach a steady equilibrium state, indicated by a constant mass of the sample at this holding. Subsequently the gas was switched to a CO_2/N_2 mixture (80 ml/min CO_2 and 20 ml/min N_2; N_2 is used as protective gas for the setup). After completion of the reaction between powder and CO_2 (when no mass change was observed), the system was cooled to room temperature in the same CO_2/N_2 mixture at a cooling rate of 10 °C /min. All TGA experiments were based on a correction file measured with a blank crucible to exclude background data. After TGA measurements the samples were ground with a mortar and the phase composition was analyzed by X-ray diffraction (Bruker D2 PHASER with Cu K_α radiation, accelerate voltage 30KV, current 10 mA, step size 0.02, time per step 1s). For comparison the X-ray diffraction patterns of freshly synthesized powders (after calcination) were analyzed as well.

After obtaining the oxygen non-stoichiometry value (δ) in air at 950 °C the

values of δ at other temperatures were determined by simple TGA experiments in air. In these experiments the temperature was stepwise increased from 550 ˚C to 950 ˚C in flowing air (79 ml/min N_2 and 21 ml/min O_2) and hold at intervals of 100 ˚C. Based on the reference point at 950 ˚C, oxygen non-stoichiometry at other temperatures was calculated.

2.3 Results

Isothermal gravimetric analysis is a convenient way to study quantitatively the reaction between perovskite materials and CO_2 [13], and the results are given in Figure 2.1. It can be seen that the reactions are very fast for all four materials, resulting in a final increase in weight of respectively 119.04 %, 114.18 %, 108.92 % and 113.67%. In order to make sure that the reactions were completely finished, the systems were hold for a longer time at 950 ˚C before cooling. During this cooling procedure in the same CO_2/N_2 atmosphere no mass change was observed.
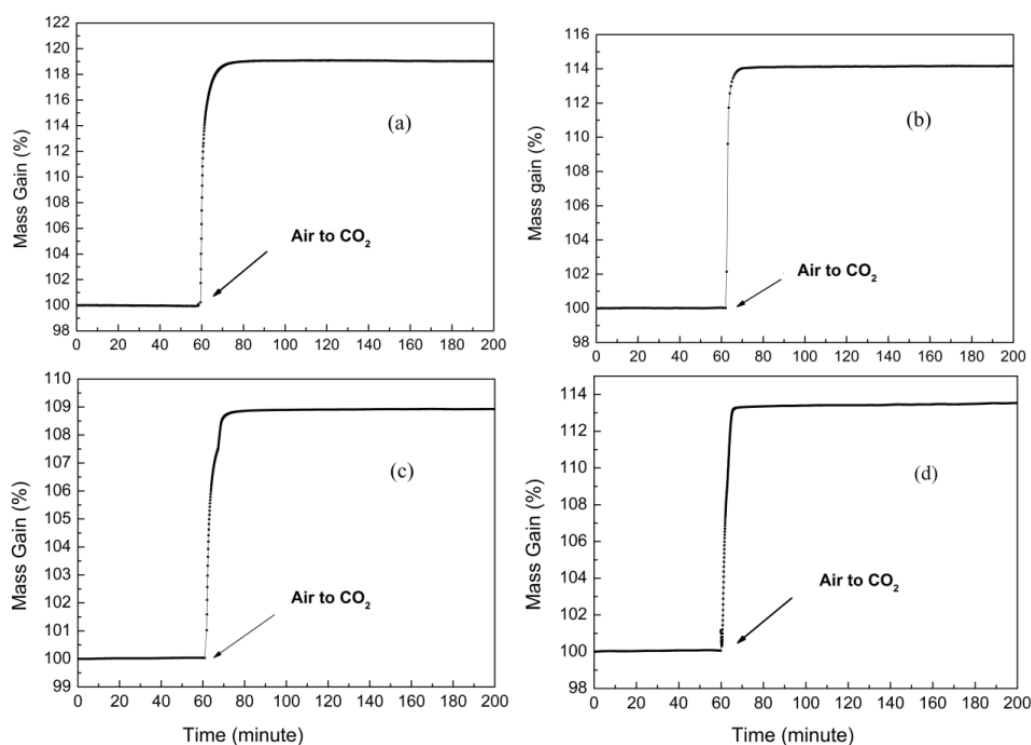
Figure. 2.1. Normalized plot of mass change of (a) $SrCoO_{3-\delta}$, (b) $BaCoO_{3-\delta}$, (c) $BaFeO_{3-\delta}$ and (d) $BaCeO_{3-\delta}$ in air/CO_2 at 950ºC

The phase composition of powder samples before and after TGA experiments

were examined by X-Ray diffraction and the results are shown in Figure 2.2. From this figure it can be seen that the characteristic peaks of the perovskite materials were not present any more after CO_2 exposure, indicating that the decomposition reaction is complete. By indexing the XRD patterns of CO_2-treated powders, products of the carbonation reactions can be determined.
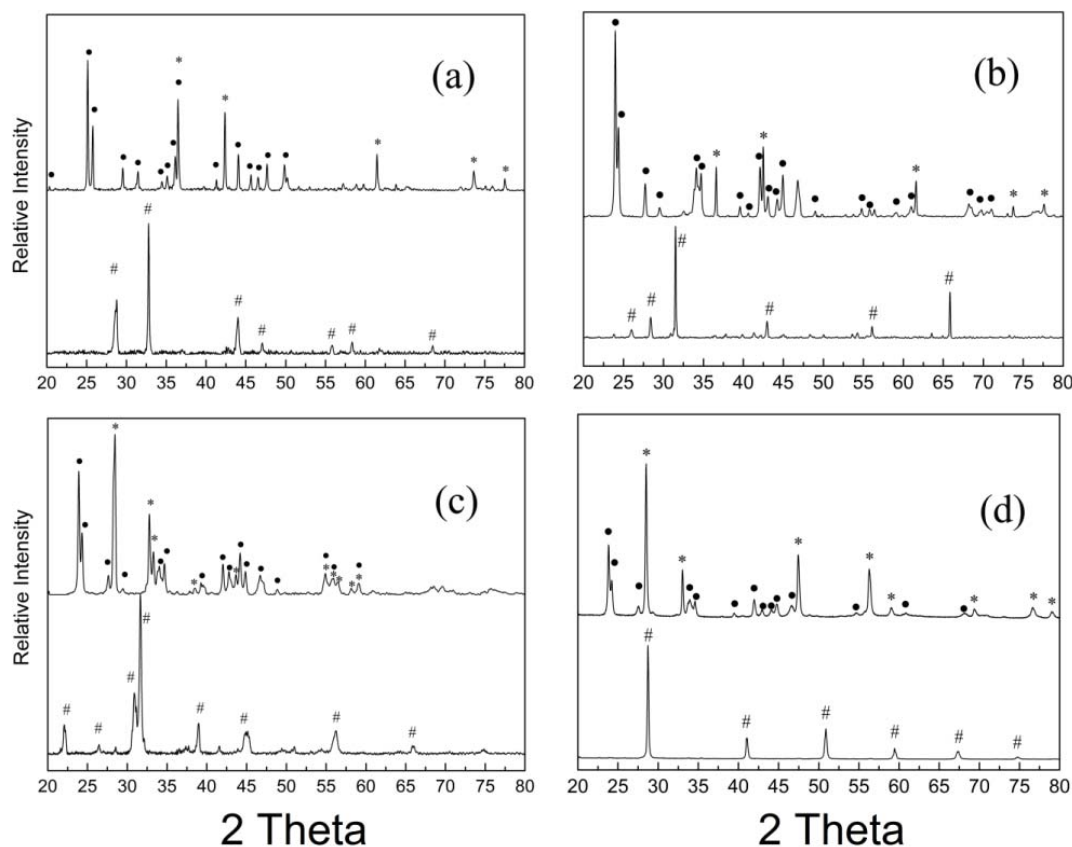
Figure. 2.2. X-Ray Diffraction pattern of (a) $SrCoO_{3-\delta}$, (b) $BaCoO_{3-\delta}$, (c) $BaFeO_{3-\delta}$ and (d) $BaCeO_{3-\delta}$ before (lower) and after (upper) CO_2 treatment at 950 ˚C. #: As prepared samples; ● in (a): $SrCO_3$; ● in (b-d):$BaCO_3$; * in (a-d): CoO, CoO, $BaFe_2O_4$, and CeO_2

Tables 2.1-2.4 summarize the XRD data to prove the degree of matching of the XRD signals of standard materials with those of the products after reaction. In these tables only characteristic peaks are given, however full indexing of the XRD data was performed in this work. From these data it is concluded that the diffraction angles (2θ) match very well. The slight deviations in intensities for some signals might be caused by the overlap of different peaks for the products obtained after the decomposition reaction. For example, in the case of $SrCoO_{3-\delta}$ after reaction with CO_2

(figure 2.2c), the characteristic peaks of CoO (111) and $SrCO_3$ (112) are so close to each other that it is impossible to separate them, which makes the intensity of CoO (111) even higher than that of CoO (200) (see table 2.1).

Table 2.1 Comparison of XRD patterns of $SrCoO_{3-\delta}$ after reaction with CO_2 at 950°C with standard XRD peaks (Cu Kα radiation)

Materials	XRD peaks (2θ)	Normalized peak intensity (Area, %)	Characteristic peaks for pure material (2θ)	Peak intensity for pure material (%)	(h k l)
			ICDD PDF No.: 78-0431		
CoO	36.51	117	36.49	68	(111)
	42.40	100	42.38	100	(200)
	61.50	56	61.49	45	(220)
	73.65	35	73.66	16	(311)
	77.55	25	77.52	11	(222)
			ICDD PDF No.: 05-0418		
SrCO₃	25.16	100	25.17	100	(111)
	25.80	46	25.80	70	(021)
	36.17	35	36.18	34	(112)
	36.51	75	36.53	40	(130)
	44.09	24	44.08	50	(221)
	47.69	20	47.69	35	(132)
	49.89	34	49.92	31	(113)

Table 2.2 Comparison of XRD patterns of $BaCoO_{3-\delta}$ after reaction with CO_2 at 950°C with standard XRD peaks (Cu Kα radiation)

Materials	XRD peaks (2θ)	Normalized peak intensity (Area, %)	Characteristic peaks for pure material (2θ)	Peak intensity for pure material (%)	(h k l)
			ICDD PDF No.: 78-0431		
CoO	36.59	54	36.49	68	(111)
	42.49	100	42.38	100	(200)
	61.58	54	61.49	45	(220)
	73.75	19	73.66	16	(311)
	77.61	27	77.52	11	(222)
			ICDD PDF No.: 71-2394		
BaCO₃	23.98	100	23.90	100	(111)
	24.39	48	24.31	52	(021)
	34.13	25	34.10	21	(112)
	34.70	23	34.61	25	(130)
	42.09	27	42.00	28	(221)
	44.94	22	44.92	23	(132)
	46.78	19	46.80	18	(113)

Table 2.3 Comparison of XRD patterns of $BaFeO_{3-\delta}$ after reaction with CO_2 at 950°C with standard XRD peaks (Cu Kα radiation)

Materials	XRD peaks (2θ)	Normalized peak intensity (Area, %)	Characteristic peaks for pure material (2θ)	Peak intensity for pure material (%)	(h k l)
			ICDD PDF No.: 25-1191		
BaFe₂O₄	28.27	99	28.22	54	(402)
	28.47	100	28.41	100	(212)
	32.79	80	32.70	56	(610)
	33.32	38	33.22	27	(020)
	44.19	50	44.12	21	(422)
			ICDD PDF No.: 71-2394		
BaCO₃	23.90	100	23.90	100	(111)
	24.33	57	24.31	52	(021)
	34.05	28	34.10	21	(112)
	34.64	19	34.61	25	(130)
	42.03	27	42.00	28	(221)
	44.88	22	44.92	23	(132)
	46.70	31	46.80	18	(113)

Table 2.4 Comparison of XRD Patterns of $BaCeO_{3-\delta}$ after reaction with CO_2 at 950°C with Standard XRD Peaks (Cu Kα radiation)

Materials	XRD peaks (2θ)	Normalized peak intensity (Area, %)	Characteristic peaks for pure material (2θ)	Peak intensity for pure material (%)	(h k l)
			ICDD PDF No.: 43-1002		
CeO₂	28.55	100	28.55	100	(111)
	33.08	26	33.08	27	(200)
	47.49	53	47.48	46	(220)
	56.33	48	56.34	34	(311)
	76.66	15	76.70	12	(331)
			ICDD PDF No.: 71-2394		
BaCO₃	23.89	100	23.90	100	(111)
	24.27	73	24.31	52	(021)
	34.02	35	34.10	21	(112)
	34.68	15	34.61	25	(130)
	42.01	21	42.00	28	(221)
	44.95	20	44.92	23	(132)
	46.65	17	46.80	18	(113)

According to the XRD results, the reactions between $SrCoO_{3-\delta}$, $BaCoO_{3-\delta}$, $BaFeO_{3-\delta}$, $BaCeO_{3-\delta}$ and CO_2 at 950 ºC can be described as follow:

$$SrCoO_{3-\delta} + CO_2 \rightarrow SrCO_3 + CoO + \frac{1-\delta}{2}O_2 \tag{2.1}$$

$$BaCoO_{3-\delta} + CO_2 \rightarrow BaCO_3 + CoO + \frac{1-\delta}{2}O_2 \tag{2.2}$$

$$2BaFeO_{3-\delta} + CO_2 \rightarrow BaFe_2O_4 + BaCO_3 + \frac{1-2\delta}{2}O_2 \tag{2.3}$$

$$BaCeO_{3-\delta} + CO_2 \rightarrow BaCO_3 + CeO_2 - \frac{\delta}{2}O_2 \tag{2.4}$$
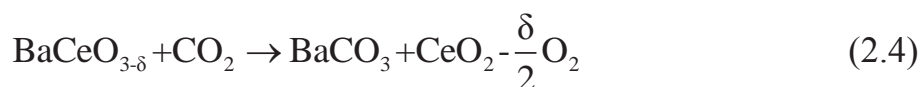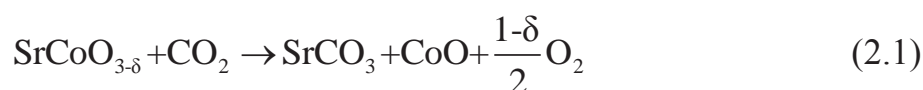
As shown by XRD, in our case the products (CoO, $SrCO_3$, $BaCO_3$, CeO_2 and

$BaFe_2O_4$) are stoichiometric and the reactions are complete. The following equation, describing the mass change during the reaction, can then be established:

$$\frac{m_1}{MW_{ABCoO_{3-\delta}}} = \frac{m_2}{MW_{ss}} \tag{2.5}$$

where m_1 and $MW_{ABCoO_{3-\delta}}$ represent the mass and molecular weight of the samples before the reaction with CO_2; m_2 and MW_{SS} are the mass and the sum of the molecular weights of the products after reaction. For example, MW_{SS} for reaction (1) is the sum of mole weight of $SrCO_3$ and CoO. Since MW_{SS} is known and m_1 and m_2 can be determined from the TGA results, the molecular weight of $ABO_{3-\delta}$ can be calculated according to eq. (2.5) and subsequently the oxygen non-stoichiometry (δ) is determined to be as 0.48, 0.36, 0.43 and 0.03 for $SrCoO_{3-\delta}$, $BaCoO_{3-\delta}$, $BaFeO_{3-\delta}$ and $BaCeO_{3-\delta}$ respectively, which is in agreement with literature [14-16].

Based on the reference point measured at 950 °C in air, oxygen non-stoichiometry (δ) at other temperatures can be acquired according to eq. (2.6).

$$\frac{m_T}{MW_T} = \frac{m_{950}}{MW_{950}} \tag{2.6}$$

where m_T and MW_T represent the mass and molecular weight of $ABO_{3-\delta}$ at temperature T, m_{950} and MW_{950} are the mass and molecular weight at 950 ˚C. In this study, the temperature was stepwise increased to 950°C in air, and at each measuring point (550 ˚C, 650 ˚C, 750 ˚C, 850 ˚C, and 950 ˚C) the temperature was kept constant until a steady state was reached. The results, as given in Figure 2.3, clearly indicate that equilibrium was really obtained during these holding temperatures as no weight loss is observed prior to the next heating step. The oxygen non-stoichiometry was calculated according to eq. (2.6) and results are shown in Figure 2.4. For $BaCeO_{3-\delta}$, due to extremely small mass change during heating, we could not do the same analysis as above with our equipment, so the result for $BaCeO_{3-\delta}$ was not given in this study.
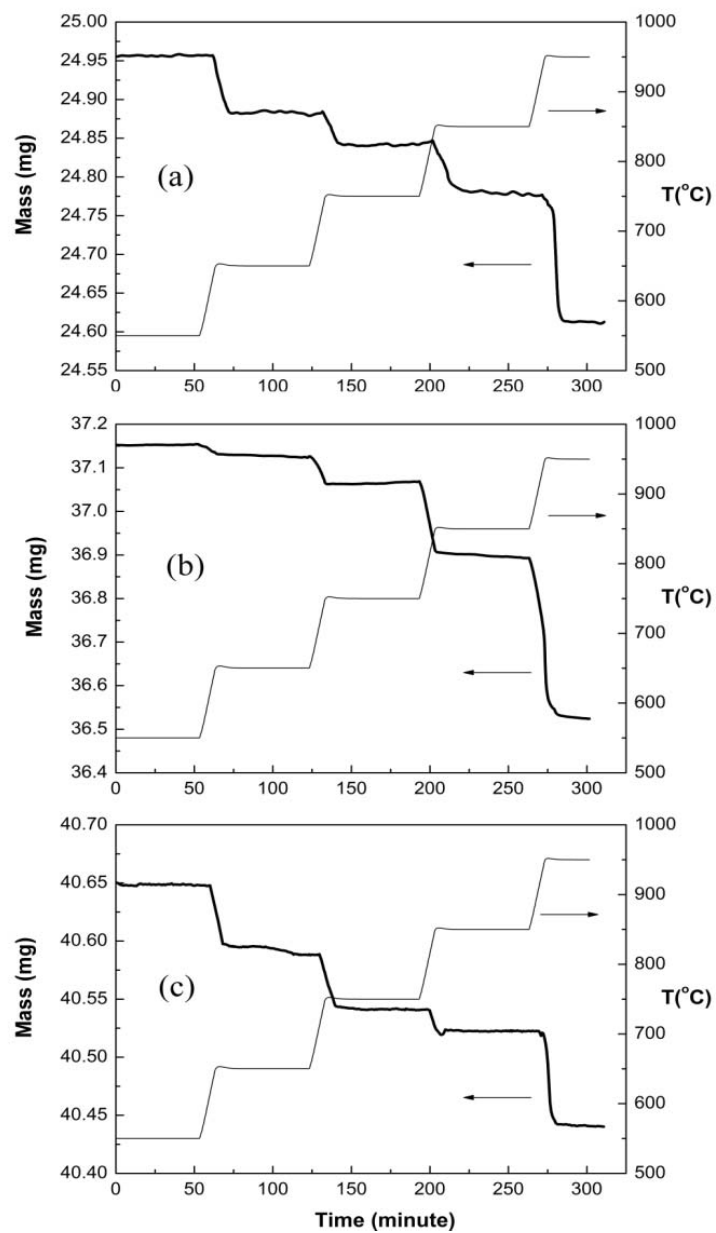
Figure. 2.3. Mass change of powder sample in air as function of temperature; (a) $SrCoO_{3-\delta}$, (b) $BaCoO_{3-\delta}$ and (c) $BaFeO_{3-\delta}$
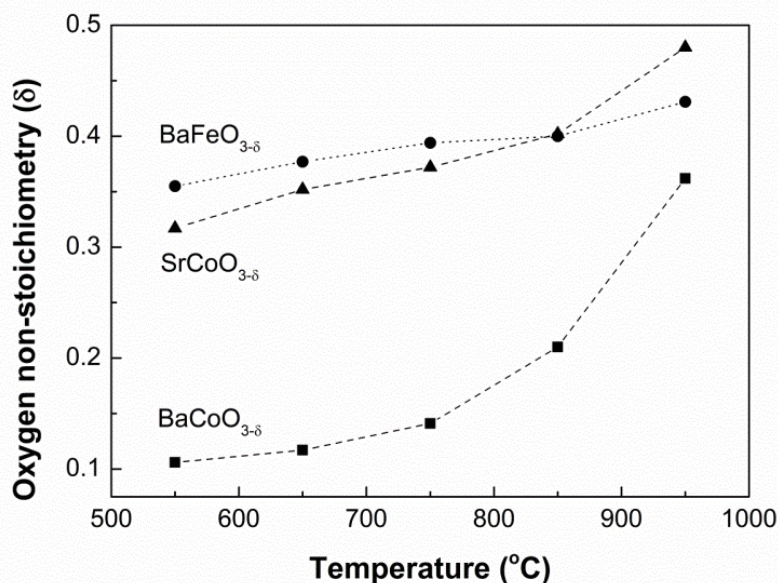
Figure. 2.4. Temperature dependence of oxygen non-stoichiometry (δ) in $SrCoO_{3-\delta}$ ($\blacktriangle$), $BaCoO_{3-\delta}$ ($\blacksquare$) and $BaFeO_{3-\delta}$ ($\bullet$) in air; Dashed lines are guides to the eye

2.4 Discussion

The principle of this method is similar to the hydrogen reduction method, because in both cases the perovskite materials react with a sweeping gas resulting in stoichiometric products; subsequently the oxygen non-stoichiometry is calculated from the mass change. However, the reaction mechanism is completely different, one is reduction and another one is carbonation. Due to this difference, some materials that do not react with CO_2 may react with hydrogen, and some materials that do not react with hydrogen may react with CO_2, which gives the idea that we can choose appropriate method for certain material. For example, $BaCeO_{3-\delta}$ is a well-known perovskite material for hydrogen separation and it is very stable in hydrogen containing atmosphere, indicating that we cannot use hydrogen reduction method to determine its oxygen non-stoichiometry, however this material is very sensitive to CO_2 and we can analyze the oxygen non-stoichiometry by CO_2 method.

An accurate analysis of the phase composition of the reaction products is of great importance, which in this work was examined by room-temperature XRD. It should

be pointed out that there might be some phase transitions during the cooling process, meaning that the phase composition at 950 ˚C could be different. However, as in this work no mass change was observed during cooling, the assumption can be made that the products of the reactions (1-4) at 950 ˚C are the same as those analyzed at room temperature and can be used to calculate the oxygen non-stoichiometry by eq. (2.5). Nevertheless, high temperature XRD in a CO_2 atmosphere is the best way to identify the phase composition. This might be possible, because CO_2 is not explosive and toxic and it is therefore safe to conduct XRD experiments under such conditions, which is not the case for the explosive properties of hydrogen at the higher temperatures of interest.

Evaluation of the accuracy of the method is also important, especially when the oxygen non-stoichiometry change is very small, like for $BaCeO_{3-\delta}$. The cumulative error of this method may arise from different steps in the experiment, but the most important one is weighing part. In this study, the weighing error of our TGA equipment is around 0.01 % (20~50 mg powder was used), and it will cause 0.01 deviation in the oxygen non-stoichiometry calculation. Generally, there are two ways to increase the accuracy of this method. The first one is to increase the accuracy of the TGA setup, however this is limited, due to current technology; e.g.: the best accuracy for an electronic balance is 0.001 mg. Alternatively, one can use more powder to increase the accuracy as well. In some other studies, around 1 g or even 3~4 g was used for TGA measurements [17, 18]. If for example in this study 200 mg powder was used and weighed with the same accuracy, the deviation of 3-δ would be reduced to 0.001.

2.5 Conclusion

A new method to determine the oxygen non-stoichiometry of perovskite materials under equilibrium state has been developed and demonstrated by using $SrCoO_{3-\delta}$, $BaCoO_{3-\delta}$, $BaFeO_{3-\delta}$ and $BaCeO_{3-\delta}$ as representative materials. The oxygen non-stoichiometry (δ) of these 4 materials at 950ºC in air was measured to be 0.48,

0.36, 0.43 and 0.03 respectively. Based on these reference points, the oxygen non-stoichiometry at other temperatures was also measured, while this method is expected to be successful for other perovskite materials as well. This method is not only restricted for analysis of δ in air, large variations in oxygen partial pressures can also be used, because the equilibrium state for all partial pressures can easily be attained at (sufficient) high temperatures.

References

[1]   T. Nagai, W. Ito, T. Sakon, Solid State Ionics 177 (2007) (39-40) 3433.

[2]   V.G. Milt, M.A. Ulla, E.E. Miro, Applied Catalysis B-Environmental 57 (2005) (1) 13.

[3]   J. Suntivich, H.A. Gasteiger, N. Yabuuchi, H. Nakanishi, J.B. Goodenough, Y. Shao-Horn, Nat Chem 3 (2011) (7) 546.

[4]   M.V. Patrakeev, I.A. Leonidov, V.L. Kozhevnikov, J Solid State Electr 15 (2011) (5) 931.

[5]   A.N. Petrov, V.A. Cherepanov, O.F. Kononchuk, L.Y. Gavrilova, Journal of Solid State Chemistry 87 (1990) (1) 69.

[6]   B. M., T. K., U. H., Fachzeitschrift fuer das Laboratorium 38 (1994) 6.

[7]   K. Teske, H. Ullmann, D. Rettig, Journal of Nuclear Materials 116 (1983) (2–3) 260.

[8]   V.V. Vashook, M.V. Zinkevich, H. Ullmann, J. Paulsen, N. Trofimenko, K. Teske, Solid State Ionics 99 (1997) (1–2) 23.

[9]   M. Karppinen, M. Matvejeff, K. Salomaki, H. Yamauchi, J Mater Chem 12 (2002) (6) 1761.

[10]   S. McIntosh, J.F. Vente, W.G. Haije, D.H.A. Blank, H.J.M. Bouwmeester, Solid State Ionics 177 (2006) (19-25 SPEC. ISS.) 1737.

[11]   J. Yi, M. Schroeder, T. Weirich, J. Mayer, Chem Mater 22 (2010) (23) 6246.

[12]   H. Patra, S.K. Rout, S.K. Pratihar, S. Bhattacharya, Powder Technology 209 (2011) (1-3) 98.

[13]   Q. Zeng, Y.B. Zu, C.G. Fan, C.S. Chen, Journal of Membrane Science 335 (2009) (1-2) 140.

[14]   J. Rodríguez, J.M. González-Calbet, Mater Res Bull 21 (1986) (4) 429.

[15]   A.J. Jacobson, J.L. Hutchison, Journal of the Chemical Society, Chemical Communications (1976) (3).

[16]   H.J.V. Hook, The Journal of Physical Chemistry 68 (1964) (12) 3786.

[17]   S. Kim, R. Merkle, J. Maier, Surface Science 549 (2004) (3) 196.

[18]   M. Oishi, K. Yashiro, K. Sato, J. Mizusaki, N. Kitamura, K. Amezawa, T. Kawada, Y. Uchimoto, Solid State Ionics 179 (2008) (15-16) 529.

Chapter 3 A description of oxygen transport in a bench-scale oxygen permeation set-up using computing fluid dynamics

Abstract

Measuring the oxygen permeability of dense ceramic membranes is usually performed with a lab-scale oxygen permeation set-up, in which feed and sweep gas are directly flushed to the membrane surface. Due to concentration gradients within the experimental setup, the oxygen partial pressure (P_{O_2}) measured at the outlet of the set-up is not the same as the P_{O_2} on the membrane surface, which leads to an inaccurate calculation of the oxygen ionic conductivity (a measure of oxygen permeability) of the membranes. In order to overcome this problem, a computational fluid dynamics (CFD) model is developed to describe the oxygen transport in such a set-up and special attention is paid to the exact oxygen partial pressures on the membrane surface. With this CFD model, the oxygen ionic conductivity of a selected model membrane, $SrCo_{0.8}Fe_{0.2}O_{3-\delta}$ (SCF), is calculated. In addition, the influence of several parameters such as the distance from sweep gas inlet to the membrane surface, the sweep gas flow rate and the type of sweep gas on the oxygen partial pressure distribution in the setup is studied.

3.1 Introduction

Dense ceramic membranes made from mixed ionic-electronic conducting (MIEC) oxides have attracted considerable attention in the past decades due to their potential application in oxygen separation from air. The major advantage of oxygen separation by these membranes over other techniques, such as cryogenic distillation and pressure swing adsorption (PSA), lies in their infinite selectivity, i.e. only oxygen can go through the membranes. In addition, the oxygen separation can easily be coupled with other chemical processes where oxygen is required, for example, partial oxidation of methane or oxy-fuel combustion for CO_2 capture [1-3].

The research on MIEC membranes was initiated by Teraoka et al. [4] in the 1980's. After that, a lot of work has been done to improve the performance of the MIEC membranes, for example, to increase the oxygen permeability. A commonly used method to measure the oxygen permeability of a MIEC membrane is a high temperature oxygen permeation experiment, which usually makes use of a bench-scale set-up as schematically shown in Figure 3.1. In most cases air is used as feed gas and an inert gas such as helium or argon is used as sweep gas. The oxygen flux through the membranes can be calculated by analyzing the oxygen concentration at the exit of the set-up, usually by using an oxygen sensor or a gas chromatograph (GC).
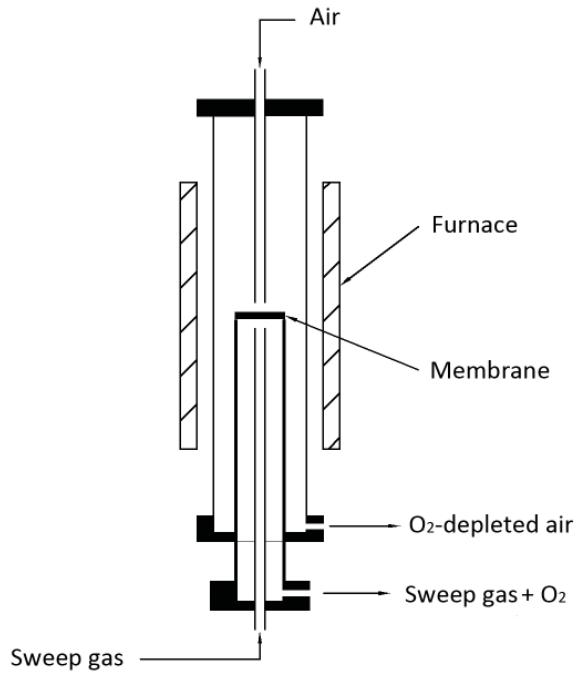
Figure 3.1. Schematic diagram of the high temperature oxygen permeation set-up.

The oxygen flux through a MIEC membrane reflects the oxygen permeability through the membrane. However, the oxygen flux is affected by many parameters, such as membrane thickness, operating temperature and feed/sweep gas flow rate. A better way to evaluate a MIEC membrane is to determine the oxygen ionic conductivity, which is an intrinsic material property of the membrane and can be obtained from the oxygen permeation data by using the following equation, as proposed by Chen et al. [5].

$$\sigma_{ion}(P''_{O_2}) = -\frac{4^2 F^2 L}{RT}\left[\frac{dj_{O_2}}{d\ln P''_{O_2}}\right]_{P'_{O_2}=\text{constant}}$$
(3.1)

where j_{O_2} is oxygen flux, R the gas constant, T absolute temperature, F the Faraday constant, L the membrane thickness, σ_{ion} the oxygen ionic conductivity, P'_{O_2} the oxygen partial pressure at the feed side and P''_{O_2} the oxygen partial pressure at the sweep side of the membrane.

For calculating σ_{ion} of a membrane from oxygen flux data, it is in most cases assumed that the oxygen partial pressure (P_{O_2}) at the outlet (= "sweep gas + O$_2$" in Figure 5.1) has the same value as the oxygen partial pressure at the surface (= P''_{O_2}). In other words it is assumed that the oxygen permeation set-up, as shown in Figure 3.1, works as a Continuous Ideally Stirred-Tank Reactor (CISTR), which means a perfect mixing of both nitrogen/oxygen in the feed (air) compartment and sweep gas/oxygen in the permeate compartment. However, the validity of the CISTR assumption depends on the reactor geometry as well as operating parameters. Very often this CISTR assumption is not true and the gas mixing is incomplete [6], i.e. the P_{O_2} measured at the outlet of the permeation set-up is not equal to the P_{O_2} on the membrane surface, hence the calculation of σ_{ion} based on the CISTR assumption is not accurate. In order to obtain a more accurate value of σ_{ion} for a membrane, it is necessary to know the exact P_{O_2} on the membrane surface. However, direct measuring of P_{O_2} on the membrane surface is experimentally very difficult in such a small device and any probing in the permeation set-up will inevitably affect the flow field.

In this work, a method is developed to determine σ_{ion} of a MIEC membrane more accurately from oxygen permeation experiments with the aid of computational fluid dynamics modeling (CFD). It is also intended to understand the oxygen gradient in the above mentioned reactor and its effect on the oxygen flux through the membrane. For this purpose the COMSOL Multiphysics® program was applied as modeling tool while SrCo$_{0.8}$Fe$_{0.2}$O$_{3-\delta}$ was used as membrane material in this study.

3.2 Experimental and methodological procedure

3.2.1 Membrane fabrication and oxygen permeation experiments

$SrCo_{0.8}Fe_{0.2}O_{3-\delta}$ (SCF) was synthesized using an EDTA complexation/pyrolysis process. Metal nitrates were dissolved in demineralized water under stirring at a stoichiometric ratio. EDTA, dissolved in ammonia, was added and after chelating for several minutes citric acid was added. The molar ratio of total metal ions : EDTA : citric acid was 1.0 : 1.0 : 1.5. The pH of the solution was adjusted to 6 by adding ammonia. Subsequently NH_4NO_3 was added as an ignition aid at an amount of 100 g NH_4NO_3 per 0.1 mole of metal ions. This final solution was heated at 120-150 °C under stirring to evaporate water until it changed into a viscous gel and was transferred to a stainless steel vessel and heated on a hot plate at a temperature of around 500 ˚C, while a vigorous combustion took place, resulting in a fluffy powder. The powder was collected and calcined in a room furnace at 950 °C for 5 hours at a heating and cooling rate of 3 °C/min. The calcined powders were uniaxially pressed at 4 MPa into disk shapes, subsequently cold isostatically pressed at 400 Mpa for 6 minutes and sintered in ambient air at 1200 °C for 10 hours.

The experimental set-up for oxygen permeation measurements is schematically shown in Figure 3.1. Disk-shaped samples with a diameter of 15 mm and a relative density > 90 % were polished to a thickness of 1 mm and ultrasonically cleaned in ethanol. The membranes were sealed to one end of a quartz tube (diameter 12 mm) using gold paste as sealant. After sealing at 1000 °C for 2 hours the temperature was lowered to 950 °C, and air was fed to one side of the sample (100 ml/min), while helium was led at 50 ml/min over the permeate side as sweep gas to carry away the permeated oxygen. The composition of the effluent stream at the permeate side was analyzed by an oxygen sensor (Systech ZR893). A gas chromatograph (Varian CP 4900 equipped with a 5 Å molecular sieve column using helium as carrier gas) was used to check the leakage of the sealing. If there is no nitrogen peak in the GC

spectrum of the permeate gas, it is assumed that the sealing is gas tight.

3.2.2 Oxygen transport through a MIEC membrane

The oxygen flux through a dense ceramic MIEC membrane is generally described by Wagner's equation, assuming bulk oxygen diffusion to be the rate limiting step [7]:

$$j_{O_2} = -\frac{RT}{(4F)^2 d} \int_{\ln pO_2'}^{\ln pO_2''} \frac{\sigma_{el} \sigma_{ion}}{\sigma_{el} + \sigma_{ion}} d\ln pO_2 \tag{3.2}$$

For most MIEC membranes, the electronic conductivity σ_{el} is two orders of magnitude higher than σ_{ion} and therefore eq. (3.2) can be rewritten as:

$$j_{O_2} = -\frac{RT}{(4F)^2 d} \int_{\ln P_{O_2}'}^{\ln P_{O_2}''} \sigma_{ion} \, d\ln P_{O_2} \tag{3.3}$$

If σ_{ion} is dependent of P_{O_2}, the following empirical power law is used to describe the oxygen ionic conductivity σ_{ion} as function of P_{O_2} [7]:

$$\sigma_{ion} = \sigma^0_{ion} (P_{O_2})^n \tag{3.4}$$

where σ^0_{ion} is the conductivity at standard state (P_{O_2} = 1 bar). By integrating eq. (3.3) with (3.4), the following equation for the oxygen flux is obtained

$$j_{O_2} = \frac{RT\sigma^0_{ion}}{(4F)^2 n d} (P_{O_2}'^n - P_{O_2}''^n) \tag{3.5}$$

3.2.3 Design of a numerical model for the oxygen permeation set-up
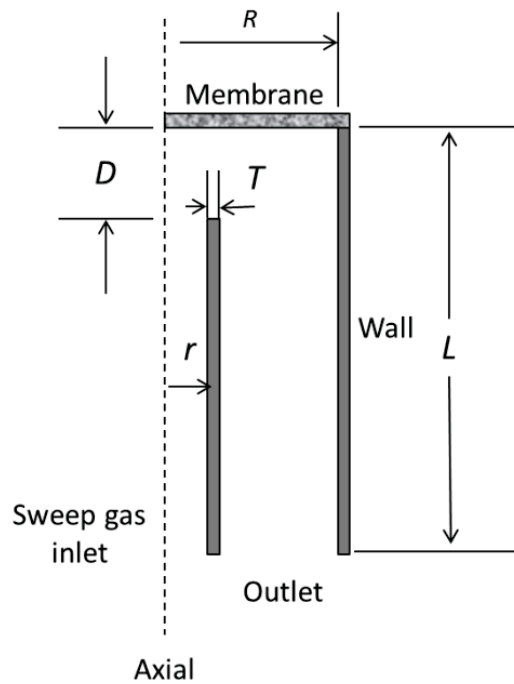
Figure 3.2. Schematic representation of the oxygen permeation set-up as used for the simulation.

The model used for the Computational Fluid Dynamics (CFD) simulation is schematically shown in Figure 3.2 and the dimensions of this model are given in Table 3.1. It should be noted that the incomplete gas mixing may occur at both the feed side and permeate side of the membrane. The change in P_{O_2} in the feed side, however, is expected to be rather small, because in most cases a large flow rate is used and only a small part of the oxygen is consumed [6]. Therefore, in this study P_{O_2} is assumed to be constant in the feed compartment of the set-up (0.21 bar), while in the permeate compartment of the reactor a gradient in P_{O_2} is expected.

The P_{O_2} distribution in the permeate compartment is obtained by simultaneously solving the Navier-Stokes and Maxwell-Stefan diffusion equations with the boundary conditions as given in Table 3.2. It should be noted that the laminar flow model is selected for the flow field calculation. This was allowed because Reynold's number is < 50 in the smallest diameter of the system (sweep gas inlet tube) for sweep gas

flow rates up to 90 ml/min.

Meshing is an important factor that can affect the accuracy of a CFD simulation. In general, finer meshing usually ensures a higher accuracy, but it also increases computation work. In this study, we gradually refined the mesh by reducing the element size until the simulation results remained the same. The total number of elements, used in this study, is ~ 20,000.

Table 3.1. Geometry of the permeation set-up

Variable	Value	Units
Membrane radius, R_m	6	mm
Membrane thickness	1	mm
Sweep gas inlet tube (inner radius), r	1.5	mm
Distance of sweep gas inlet to membrane, D	3.6	mm
Sweep gas tube thickness, T	1	mm
Pressure	1.0	atm
Simulated length, L	15	mm

Table 3.2. Boundary conditions for simulation

Boundary conditions (convection)	Type
Sweep gas inlet	Mass flow
Membrane inlet	Pointwise mass flow[**]
Sweep gas outlet	Pressure (1 bar)
Axis	Axial symmetry
Membrane	Non-slip
Wall	Non-slip

Boundary conditions (diffusion)	Type
Sweep gas inlet	Oxygen mole fraction (0.001)
Sweep gas outlet	Convective flow
Axis	Axial symmetry
Membrane	Inward flux[**]
Wall	No flux

** The inward flux is calculated by eq. (3.5).

3.2.4 Calculation of oxygen ionic conductivity from oxygen permeation data

As can be seen form eq. (3.5), the oxygen ionic conductivity of a MIEC membrane is dependent on P_{O_2}. The calculation of σ°_{ion} and n from oxygen permeation measurements was done in 2 steps. The first step is to estimate σ°_{ion} and n under the CISTR assumption, so by assuming that the P_{O_2} measured at the outlet of the set-up is identical to that on the membrane surface (P''_{O_2}). By using eq. (3.1) a data set of $\sigma_{ion} \sim P''_{O_2}$ is obtained in this way. This data set is used to fit the eq. (3.4) by applying a least-square algorithm. In this way the two parameters, σ°_{ion} and n, are obtained but still assuming a CISTR approach of the permeation set-up.

In the second step, the estimated σ°_{ion} and n from the first step are used as input parameters for the COMSOL model, where there is no CISTR assumption. The fitting program with COMSOL is illustrated in Figure 3.3. With a given set of σ°_{ion} and n the P_{O_2} on the membrane surface and at the outlet of the permeation set-up are calculated with COMSOL. During iteration, σ°_{ion} and n were adjusted until the calculated P_{O_2} at the outlet of the permeation set-up is in agreement with the P_{O_2} measured in experiments.
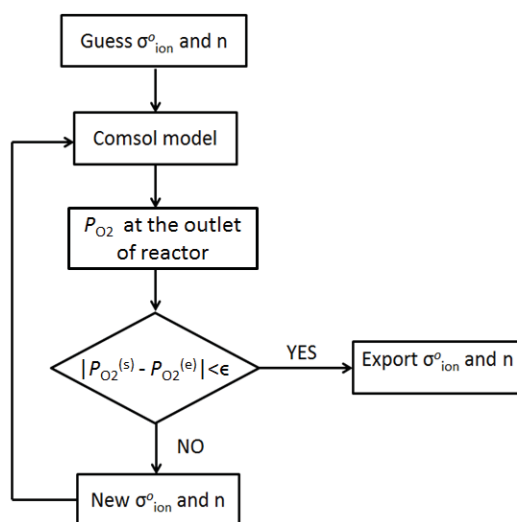
Figure 3.3. Fitting procedure for calculation of the oxygen ionic conductivity. $P_{O2}^{\,s}$ and $P_{O2}^{\,e}$ are the oxygen partial pressure at the outlet of the reactor, respectively calculated using the COMSOL Multiphysics® program model and the experimentally determined one.

3.3 Results and discussion

3.3.1 Oxygen permeation results

Table 3.3 gives the oxygen flux of SCF membranes at different temperature and at different sweep flow rates. As we can see, the oxygen permeation flux increases with sweep gas flow rate, which is because of the overall P_{O_2} at the permeate side of the membrane is decreased when a higher sweep gas flow rate is used, leading to an increase of the driving force. The oxygen flux decrease with decreasing sweep flow

rate as observed at 800 °C is explained by the phase transition of SCF from the cubic to the orthorhombic structure [8-9], which latter has a lower oxygen permeability. The phase transition of SCF occurs at around 790 °C, and is affected by the P_{O_2}. At lower P_{O_2} (meaning in this case a higher sweep-gas flow rate) the phase transition is more likely to occur.

Table 3.3. Oxygen flux of SCF membranes at different temperatures and different sweep gas flow rates

Helium flow rate (ml/min)	j_{O_2} (mol/cm^2/s, $\times 10^{-7}$)			
	800°C	850°C	900°C	950°C
31.19	3.13	5.99	7.88	9.86
47.69	3.03	6.19	8.40	10.74
73.49	3.07	6.65	9.22	12.03
95.89	3.00	6.71	9.56	12.58

3.3.2 Oxygen ionic conductivity of SCF

Fitting results of σ^o_{ion} and n without (= initial values, using eq. (3.1) and (3.4)) and with (= fitted values, using COMSOL) CISTR assumption are given in Table 3.4. As can be seen, both σ^o_{ion} and n tend to be smaller if a CISTR assumption is made and the difference is getting more pronounced at a higher temperature.

Table 3.4. Oxygen ionic conductivity σ^o_{ion} and power index n obtained from fitting experimental results.

		800°C	850°C	900°C	950°C
Initial values	σ^o_{ion} (S/cm)	0.83	1.26	1.47	1.79
	n	0.34	0.28	0.24	0.22

Fitted	σ^{o}_{ion} (S/cm)	0.82	1.30	1.53	1.87
values	n	0.57	0.43	0.36	0.32

From an Arrhenius plot of log (σ^{o}_{ion}) versus 1000/T (Figure 3.4, non-CISTR), suggesting a thermal activation process for σ^{o}_{ion}, an activation energy of 25 ± 4 kJ/mole is calculated, which is similar to the result as reported by Qiu et al. [9]. The n value increases with decreasing temperature, suggesting that the ionic conductivity is more sensitive to P_{O_2} at lower temperature.
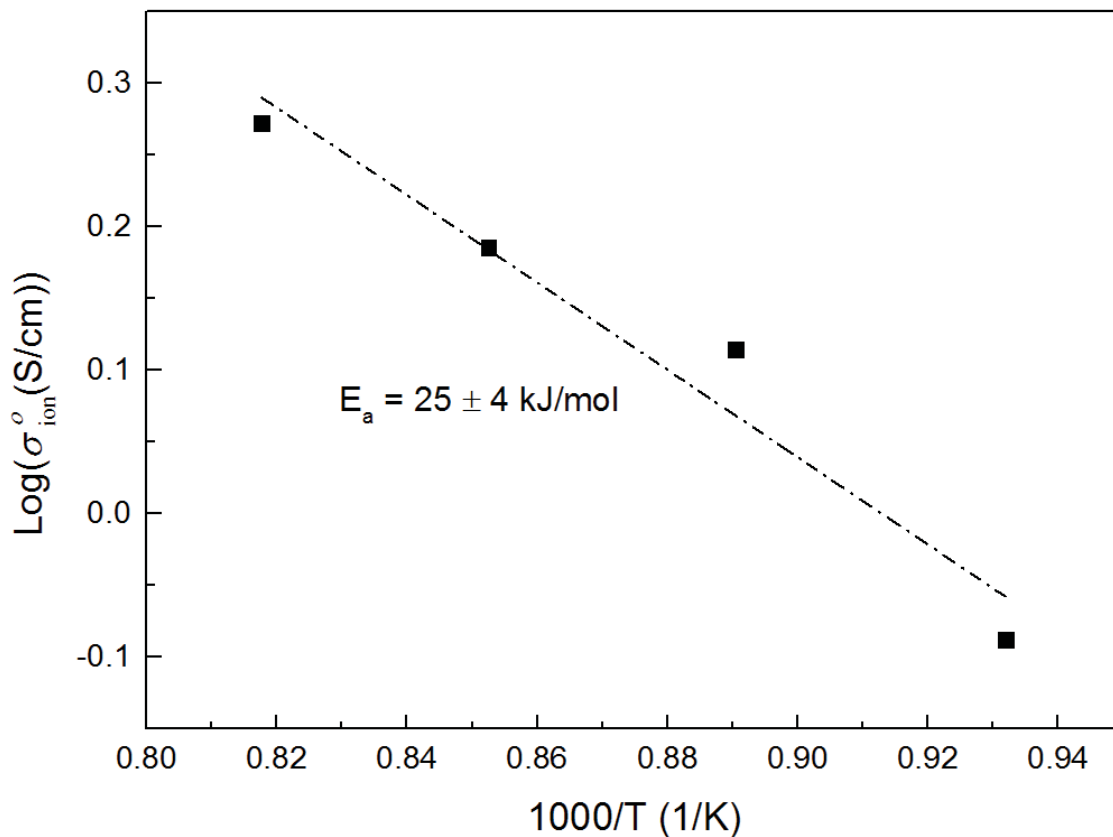
Figure 3.4. Temperature dependence of σ^{o}_{ion} for SCF membrane.

3.3.3 Parameters influencing the P_{O_2} distribution at the permeate side of the membrane

In order to compare the influence of different parameters on the P_{O_2} at the permeate side of the membrane, a reference case is required. In this reference case the following assumptions are made: (1) the distance between sweep gas inlet and membrane surface is 3 mm; (2) helium is chosen as sweep gas with a flow rate of 60 ml (STP)/min; (3) the operating temperature is 900 °C; (4) oxygen ionic conductivity data are taken from Table 3.4 ($\sigma^{\circ}{}_{ion}$ = 1.53 S/cm and n = 0.36). Other parameters are kept identical as given in Table 3.1. In the parametric study, the following cases had been investigated:

(1) The distance D between sweep gas inlet and the membrane (Figure 3.2) was varied from 1 to 5 mm with a step size of 2 mm.

(2) The sweep gas flow rate was varied from 30 to 90 ml/min (STP) with a step size of 30 ml/min (STP).

(3) When different sweep gases are used, the oxygen concentration profile in the reactor might be different because the diffusion coefficient between oxygen and the respective sweep gases is different (see table A3.1 in the appendix). In this parametric study, helium, argon, nitrogen and carbon dioxide were used as sweep gas.

Effect of reactor geometry

Due to direct flushing and the high velocity of the sweep gas in the inlet tube (~ 1 m/s at 900 °C when a flow rate of 60 ml/min is used), the P_{O_2} on the membrane surface is found to be higher at the edge (at the wall of the set-up) and lower at the center. Besides, the P_{O_2} on the membrane surface is higher than that far away from the surface. Both cases are strongly affected by the distance between the sweep gas inlet tube and the membrane surface *(D)*. As can be seen from Figure 3.5, a large D

seems to lead to a more homogenous oxygen partial pressure distribution.
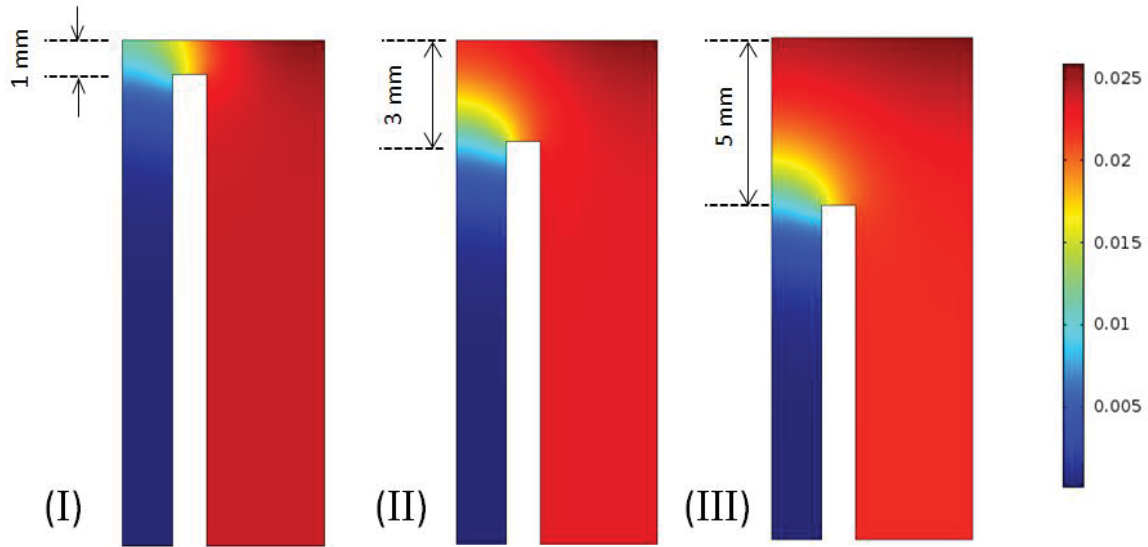
Figure 3.5. P_{O_2} (bar) in the permeation set-up as a function of D (distance from sweep gas inlet to membrane surface), I, II and III resp.: D=1, 3 and 5 mm. Helium is used as sweep gas with a flow rate of 60 ml/min.
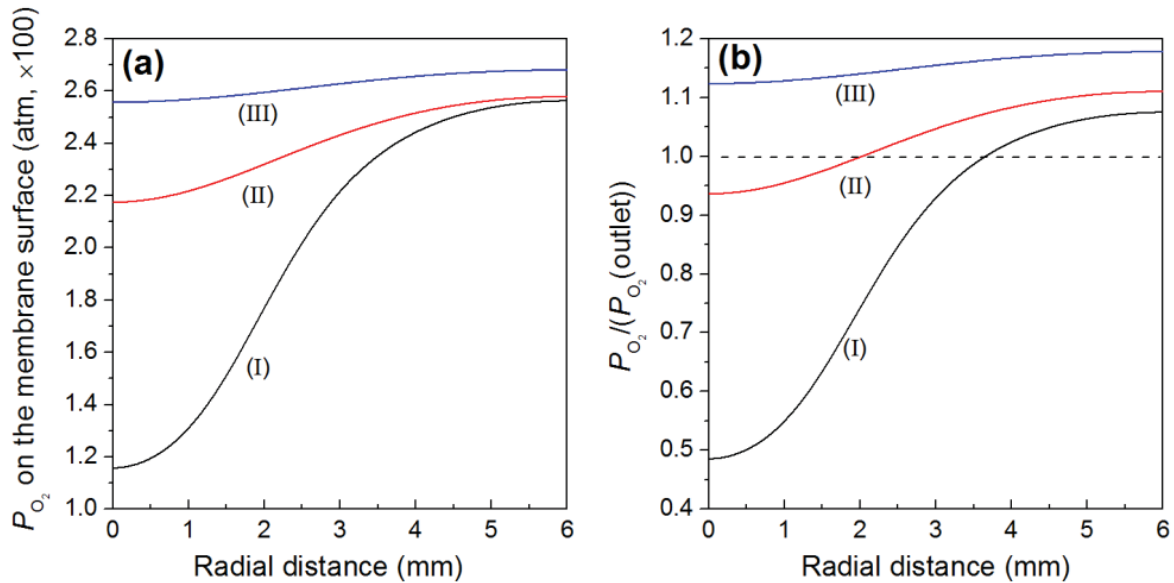
Figure 3.6. Influence of D (distance from sweep gas inlet to membrane surface) on: (a) P_{O_2} on the membrane surface; (b) ratio of P_{O_2} on the membrane surface to that at the outlet of the set-up. I, II and III resp.: $D = 1$, 3 and 5 mm. Helium is used as sweep gas with a flow rate of 60 ml/min. Radial distance: distance from membrane center to edge.

For a quantitative description of the P_{O_2} profile on the membrane surface, a plot

of P_{O_2} on the membrane surface against the radial distance (from membrane center to edge) is given in Figure 3.6a. It should be mentioned that the P_{O_2} on the membrane surface is defined as the P_{O_2} in the first mesh element layer from the membrane surface, which is around 3 μm. It can be seen from Figure 3.6a that the P_{O_2} on the membrane surface is more homogenous when a small D (1 mm) is used, for example, when D is 1 mm, the P_{O_2} at the edge of the membrane is ~ 2.2 times of that in the center, compared to a ratio of 1.04 when D is 5 mm.

Due to the lower gas velocities at the membrane surface in case of a large D, the O_2-concentration profile is more governed by the diffusive transport of the permeating oxygen than by the convective influence of the sweep gas and concentration polarization occurs In contrast, a small D causes higher sweep gas velocities at the membrane surface and therefore leads to a good transport of the permeating oxygen away from the surface. This affects also the permeation rate. When D is chosen to be 1, 3 and 5 mm, the oxygen flux is calculated to be 1.30, 1.26 and 1.23 ml/cm²/min, and it is obvious that a small D increases the oxygen flux due to more effective sweeping.

Compared to the measured oxygen partial pressure at the outlet of the setup, we can see from Figure 3.6b, that when a large D (5 mm) is used, the P_{O_2} on the membrane surface is higher than that at the outlet of the setup, regardless of the radial distance; while, for smaller D (1 and 3 mm), the P_{O_2} on the membrane surface is partly higher (at the membrane edge) and partly lower (membrane center) than that at the outlet of the setup. The average of this ratio is calculated to be 0.85, 1.03 and 1.15 for D = 1, 3 and 5 mm, respectively, which suggests both large and small D leads to a large deviation between P_{O_2} on the membrane surface and the value measured at the outlet of the set-up, while D = 3 mm seems to be a good selection in

this study and in that case the CISTR assumption is rather realistic.

Effect of sweep gas flow rate

The effect of sweep gas flow rate on the P_{O_2} profile in the reactor is shown in Figure 3.7.
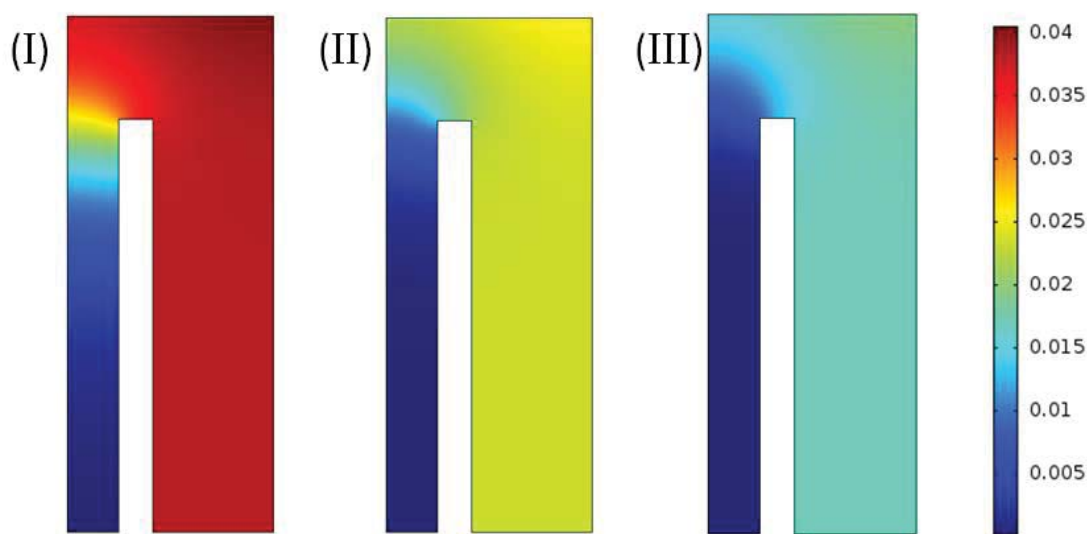
Figure 3.7. P_{O_2} (bar) in the permeation set-up as a function of helium flow rate, (I to III) helium flow rate: 30, 60 and 90 ml/min.

Figure 3.8. Influence of helium flow rate on: (a) P_{O_2} on the membrane surface; (b) ratio of P_{O_2} on the membrane surface to that at the outlet of the set-up. I, II and III resp.: 30, 60 and 90 ml/min. Radial distance: distance from membrane center to edge.

In the present study, helium is used as sweep gas. It can be seen that increasing the helium flow rate decreases the overall P_{O_2} within the reactor and therefore also on the membrane surface. It can be deduced from Figure 3.8a that P_{O_2} on the membrane surface is reduced from 3.7-4.0 bar to 1.5-1.9 bar when the helium flow rate increases from 30 to 90 ml/min. A decrease in P_{O_2} on the membrane surface leads to an increase in driving force for oxygen flux, meaning a higher oxygen flux. As can be seen from Figure 3.8b, the difference of P_{O_2} at the membrane surface and at the outlet of the reactor is getting bigger when a higher helium flow rate is applied.

Effect of sweep gas type

In most cases inert gases such as helium, argon, nitrogen or non-inert gases like CO_2 are used as sweep gas to study the oxygen permeation of dense membranes [2, 10-12]. One must be aware of the fact that diffusion of oxygen into the sweep gas is different for different gases. According to the Chapman–Enskog's theory (see appendix), the diffusion coefficient for binary gas system is mainly affected by the molecular weight differences between the gases (see eq. (3.7) in appendix). For example, the diffusion coefficients of oxygen in helium (7.20×10^{-4} m^2/s) at 900 °C is more than 3 times higher than that of oxygen in argon (2.12×10^{-4} m^2/s), indicating that diffusion of oxygen into helium is much faster than oxygen into argon. Therefore a faster mixing between the oxygen/helium is expected than that between the oxygen/argon. Figures 3.9 and 3.10 give the simulation results when different sweep gases are used. It is clear that the gas mixing, as well as the P_{O_2} homogeneousness on the membrane surface, is strongly affected by the sweep gas type. For example, when argon is used as sweep gas, the P_{O_2} at the edge of the membrane is 111 % higher than that in the center, compared to only 18 % when helium is used as sweep gas. When helium is used as sweep gas, the ratio of P_{O_2} on the membrane surface versus P_{O_2} at

the outlet of the permeation set-up is the smallest, indicating best mixing. Due to the faster diffusive oxygen transport away from the membrane surface with higher binary diffusion coefficients concentration polarization decreases. The permeation rate therefore reaches its highest value when using He as sweep gas (1.26 ml/cm^2/min), compared with 1.23, 1.23 and 1.22 ml/cm^2/min for N_2, Ar and CO_2 as sweep gas, respectively.
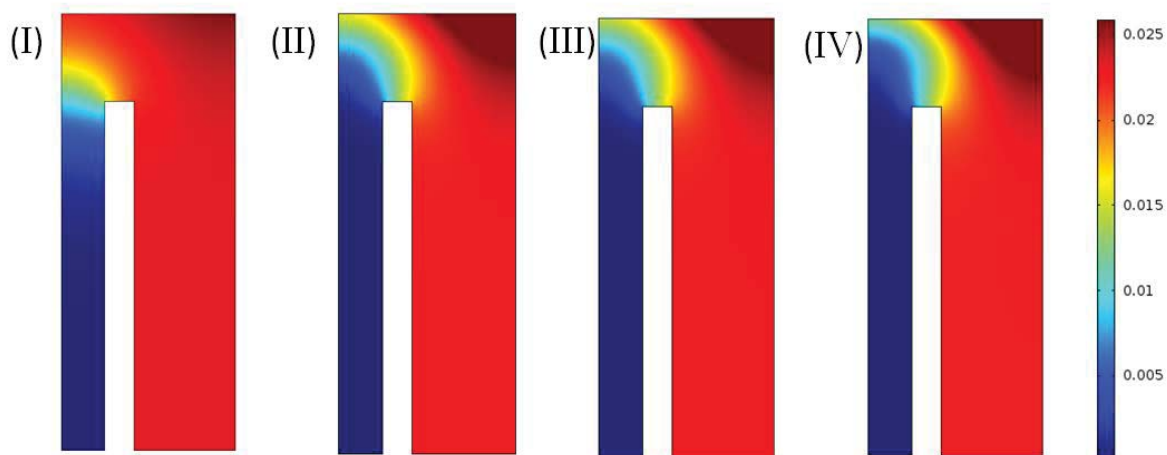
Figure 3.9. P_{O_2} (bar) in the permeation set-up when different sweep gas is used, I, II, III and IV resp.: He, N_2, Ar and CO_2. Sweep gas flow rate: 60 ml/min.
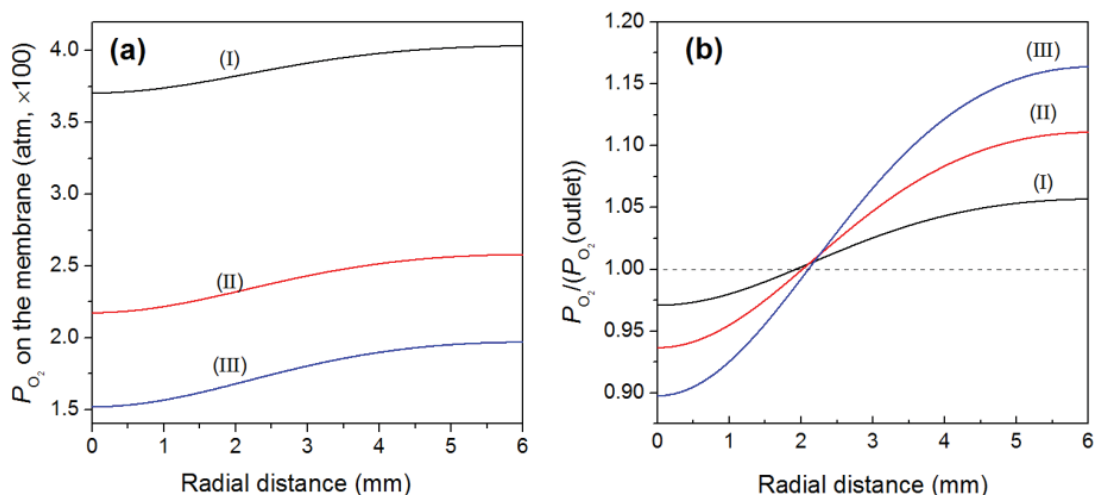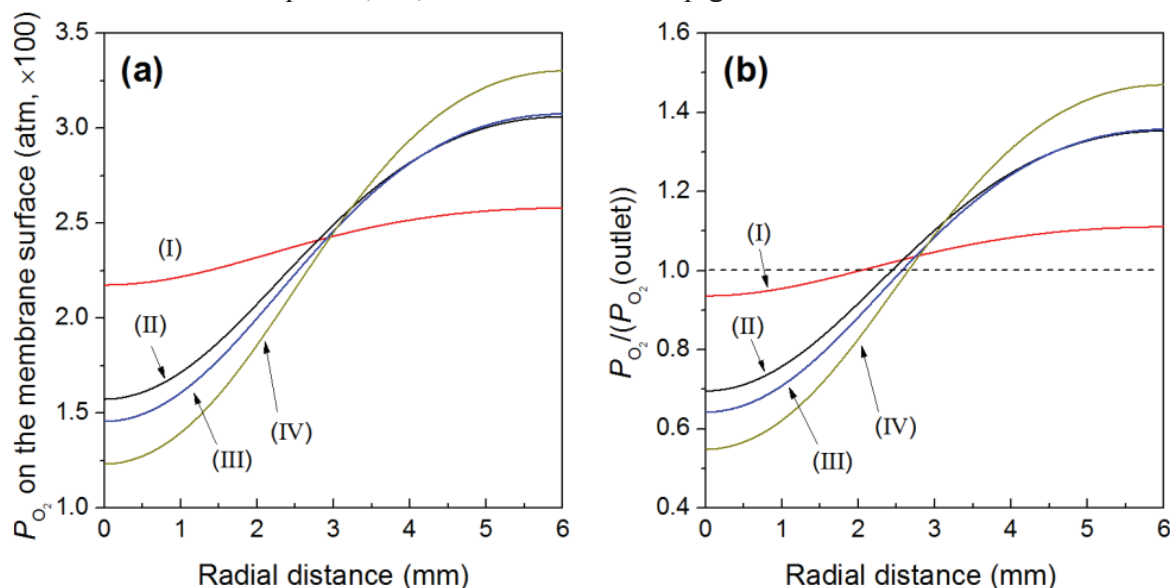

Figure 3.10. Influence of different sweep gases on: (a) P_{O_2} on the membrane surface; (b) ratio of P_{O_2} on the membrane surface to that at the outlet of the set-up. I, II and III resp.:

He, N_2, Ar and CO_2. Sweep gas flow rate: 60 ml/min. Radial distance: distance from membrane center to edge.

3.4 Conclusions

A CFD model is developed to describe the oxygen transport in a commonly used lab-scale oxygen permeation set-up. The oxygen ionic conductivity of the SCF membranes is obtained by fitting the oxygen permeation data with the aid of a CFD model, while no CISTR assumption is required. It is found from the CFD simulation that the P_{O_2} directly on the membrane surface differs from that obtained by measuring the P_{O_2} at the outlet. Furthermore, the fact that the P_{O_2} on the membrane surface is not homogeneous emphasizes the difficulty of using the CISTR assumption for determining the ionic conductivity from permeation measurements. Using the membrane's surface partial pressures determined by CFD simulations leads to a smaller oxygen ionic conductivity as when calculating the ionic conductivity under the CISTR assumption.

The influence of different parameters, such as the distance from sweep gas inlet to the membrane surface, the sweep gas flow rate and the sweep gas type, has been studied, and the following results were found:

(1) The distance from sweep gas inlet to the membrane surface affects the P_{O_2} in both radial direction and axial direction. At increasing distance the P_{O_2} on the membrane surface becomes more homogenous due to the lower sweep gas velocity at the surface, causing less convection. However, when the distance is too large, the overall P_{O_2} on the membrane surface will be much higher than that measured at the outlet of the set-up.

(2) The binary diffusion coefficient in the oxygen-sweep gas mixture has a strong influence on the concentration distribution in the setup. Higher diffusion coefficients lead to a better mixing and therefore a faster transport of the oxygen away from the

membrane surface. Faster mixing leads to a more homogeneous oxygen partial pressure distribution in the setup. Helium as sweep gas gives the highest diffusion coefficient and results in the most homogeneous oxygen partial pressure distribution in the setup, if compared with gases like N_2, Ar of CO_2.

(3) A higher sweep gas flow rate decreases the overall P_{O_2} at the permeate side of the membrane, thus increasing the oxygen flux, which makes the P_{O_2} on the membrane surface less homogenous. This influence is relatively small compared with the geometry change of the setup and sweep gas composition.

3.5 Appendix

3.5.1 Calculation of the diffusion coefficient of a gas mixture

For a binary gas system, the diffusion coefficient can be estimated by Chapman–Enskog's equation:

$$D = \frac{1.86 \times 10^{-3} T^{3/2} \sqrt{\frac{1}{M_1} + \frac{1}{M_2}}}{P \sigma_{12}^2 \Omega} \tag{3.6}$$

where D is the diffusion coefficient for the gas mixture; M_i the molar mass for gas i; $\sigma_{12} = \frac{\sigma_1 + \sigma_2}{2}$ the average collision diameter (Lennard-Jones characteristic length); T the temperature; P the pressure and Ω a dimensionless temperature-dependent collision integral. Results of several diffusion coefficients, using this equation, are given in table A3.1.

Table A3.1. Calculated gas diffusion coefficient at 1 bar. Values for σ_{12} and Ω can be found in Hirschfelder's book [13].

Temperature (K)	Diffusion coefficient (m²/s, ×10⁻⁴)			
	He-O_2	N_2-O_2	Ar-O_2	CO_2-O_2
1073	6.21	1.77	1.71	1.24
1123	6.70	1.91	1.84	1.34
1173	7.20	2.05	1.98	1.44
1223	7.71	2.19	2.12	1.55
1273	8.25	2.35	2.26	1.65

3.5.2 Calculation of the viscosity of single and mixed gases

Calculation of the viscosity of a single gas

The viscosity of a single gas at a certain temperature and pressure is usually easy

to find in handbooks. There is a small change in viscosity with pressure but a relative larger change in viscosity with temperature. The relationship between viscosity and temperature can be described by Sutherland's law[14]:

$$\mu = \mu_0 \frac{T_0 + C}{T + C} \left(\frac{T}{T_0} \right)^{3/2}$$

(3.7)

This in turn is equal to

$$\mu = \lambda \frac{T^{3/2}}{T + C}$$

(3.8)

where $\lambda = \dfrac{\mu_0 (T_0 + C)}{T_o^{3/2}}$ is a constant for the gas.

Table A3.2. Sutherland's constant, reference values and λ values for some gases [15]:

Gas	C [K]	T_0 [K]	μ_0 [μPa s]	λ [μPa s K$^{-1/2}$]
air	120	291.15	18.27	1.51
N_2	111	300.55	17.81	1.41
O_2	127	292.25	20.18	1.69
CO_2	240	293.15	14.8	1.57
CO	118	288.15	17.2	1.43
H_2	72	293.85	8.76	0.64
NH_3	370	293.15	9.82	1.30
SO_2	416	293.65	12.54	1.77
He	79.4	273	19	1.48

3.5.3 Calculation of the viscosity of mixed gases

The viscosity of a gas mixture can be calculated according to Sutherland-Thiesen equation [16]:

$$\mu_{\mathrm{m}} = \sum_{i=1}^{n} \frac{\mu_i}{1 + \dfrac{1.385\mu_1}{x_i \rho_i} \displaystyle\sum_{\substack{j=1 \\ j \neq i}}^{n} \dfrac{x_i}{D_{ij}}} \tag{3.9}$$

In case of a binary gas system, eq. (3.9) can be written:

$$\mu_{\mathrm{m}} = \frac{\mu_1}{1 + \dfrac{x_1}{x_2}\dfrac{1.385\mu_1}{D_{12}\rho_1}} + \frac{\mu_2}{1 + \dfrac{x_2}{x_1}\dfrac{1.385\mu_2}{D_{12}\rho_2}} \tag{3.10}$$

where μ_i is the viscosity of gas i; x_i is the mole fraction of gas i; D_{ij} is the diffusion coefficient between gas i and j; ρ_i is the density of gas i and μ_{m} is the viscosity of the gas mixture.

References

[1] J.J. Liu, S.Q. Zhang, W.D. Wang, J.F. Gao, W. Liu, C.S. Chen, Partial oxidation of methane in a $Zr_{0.84}Y_{0.16}O_{1.92}$-$La_{0.8}Sr_{0.2}Cr_{0.5}Fe_{0.5}O_{3-\delta}$ hollow fiber membrane reactor targeting solid oxide fuel cell applications, J Power Sources, 217 (2012) 287-290.

[2] W. Chen, C.-S. Chen, L. Winnubst, Ta-doped $SrCo_{0.8}Fe_{0.2}O_{3-\delta}$ membranes: Phase stability and oxygen permeation in CO_2 atmosphere, Solid State Ionics, 196 (2011) 30-33.

[3] B. Metz, O. Davidson, H.d. Coninck, M. Loos, L. Meyer, IPCC Special Report on Carbon Dioxide Capture and Storage, Intergovernmental Panel on Climate Change, (2005).

[4] Y. Teraoka, H.-M. Zhang, S. Furukawa, N. Yamazoe, Oxygen permeation through perovskite-type oxides, Chemistry Letter, 14 (1985) 1743-1746.

[5] C.H. Chen, H. Kruidhof, H.J.M. Bouwmeester, A.J. Burggraaf, Ionic conductivity of perovskite $LaCoO_3$ measured by oxygen permeation technique, Journal of Applied Electrochemistry, 27 (1997) 71-75.

[6] J.M. Gozálvez-Zafrilla, A. Santafé-Moros, S. Escolástico, J.M. Serra, Fluid dynamic modeling of oxygen permeation through mixed ionic-electronic conducting membranes, Journal of Membrane Science, 378 (2011) 290-300.

[7] H.J.M. Bouwmeester, A.J. Burggraaf, The CRC Handbook of Solid State Electrochemistry, 1 ed., CRC Press, 1996.

[8] W. Chen, Y.B. Zuo, C.S. Chen, A.J.A. Winnubst, Effect of Zr^{4+} doping on the oxygen stoichiometry and phase stability of $SrCo_{0.8}Fe_{0.2}O_{3-\delta}$ oxygen separation membrane, Solid State Ionics, 181 (2010) 971-975.

[9] L. Qiu, T.H. Lee, L.M. Liu, Y.L. Yang, A.J. Jacobson, Oxygen Permeation Studies of

$SrCo_{0.8}Fe_{0.2}O_{3-\delta}$, Solid State Ionics, 76 (1995) 321-329.

[10] G. Etchegoyen, T. Chartier, P. Del-Gallo, An architectural approach to the oxygen permeability of a $La_{0.6}Sr_{0.4}Fe_{0.9}Ga_{0.1}O_{3-\delta}$ perovskite membrane, J Eur Ceram Soc, 26 (2006) 2807-2815.

[11] V. Esposito, M. Søgaard, P.V. Hendriksen, Chemical stability of $La_{0.6}Sr_{0.4}CoO_{3-\delta}$ in oxygen permeation applications under exposure to N_2 and CO_2, Solid State Ionics, 227 (2012) 46-56.

[12] M.P. Lobera, J.M. Serra, S.P. Foghmoes, M. Søgaard, A. Kaiser, On the use of supported ceria membranes for oxyfuel process/syngas production, Journal of Membrane Science, 385–386 (2011) 154-161.

[13] J.O.Hirschfelder, C.F.Curtiss, R.B.Bird, Molecular Theory of Gases and Liquids, Molecular Theory of Gases and Liquids, (1954).

[14] W. Sutherland, LII. The viscosity of gases and molecular force, Philosophical Magazine Series 5, 36 (1893) 507-531.

[15] M. White, Viscous fluid flow, McGraw-Hill, Inc., 1991.

[16] J.W. Buddenberg, C.R. Wilke, Calculation of Gas Mixture Viscosities, Industrial & Engineering Chemistry, 41 (1949) 1345-1347.

Chapter 4 Ta-doped SrCo$_{0.8}$Fe$_{0.2}$O$_{3-\delta}$ membranes: Phase stability and oxygen permeation in CO$_2$ atmosphere

Abstract:

The chemical and structural stability of perovskite-derived SrCo$_{0.8}$Fe$_{0.2}$O$_{3-\delta}$ (SCF) and Sr(Co$_{0.8}$Fe$_{0.2}$)$_{0.9}$Ta$_{0.1}$O$_{3-\delta}$ (SCFTa) were investigated by both isothermal gravimetric analysis (TGA) and X-Ray diffraction (XRD). It was shown that the reaction between SCF and CO$_2$ at elevated temperature is almost negligible when Ta is doped to SCF. XPS analysis shows that the basicity of SCFTa is less than that of SCF, which may be contributed to the enhanced stability of SCFTa in CO$_2$ atmosphere. Ta^{5+} also increases the perovskite phase stability of SCF in low oxygen partial pressure (pO$_2$<10^{-2} atm), which was proven by the disappearance of a strong shrinkage signal during thermal expansion measurements. In the oxygen permeation measurement, the oxygen flux of SCFTa was slightly lower than that of SCF when an air–helium gradient was applied over the membrane, but it remained almost the same when pure CO$_2$ was introduced as sweep gas, while, the oxygen flux of SCF dropped drastically at first and decreased to zero after 60 hours in the CO$_2$ atmosphere.

4.1 Introduction

One of the reasons for global warming is the massive anthropogenic emission of CO_2, which arises mainly from use of fossil fuels. It has been proposed that burning fossil fuels with CO_2-diluted O_2 produces a concentrated CO_2 gas stream and thus enables efficient CO_2 capture [1, 2]. To improve the economic competiveness of this oxy-fuel combustion technique, there are substantial efforts in developing ceramic oxygen separation membranes that have a potential to reduce the oxygen production cost by one third over the present cryogenic air separation process [3]. It is reported that the O_2/CO_2 mixture, necessary for combustion, could be supplied by using CO_2 as sweep gas for the transport of oxygen through a Mixed Ionic and Electronic Conductor (MIEC) membrane [4-6]. The MIEC usually has the oxygen deficient perovskite structure ($ABO_{3-\delta}$), in which oxygen ions are transported via hopping of oxygen vacancies, while electrons are conducted along the B-O-B network. Several new materials have been explored from which $SrCo_{0.8}Fe_{0.2}O_{3-\delta}$ (SCF) is regarded as one of the most promising material. However, SCF has been reported to undergo a phase transition from cubic perovskite to orthorhombic brownmillerite below 790°C. Moreover, because of the presence of the alkaline-earth element Sr, SCF is very sensitive to acidic gasses like CO_2. Yi et al. showed that exposure of SCF to an atmosphere containing 5% CO_2 at 810°C resulted in the decomposition and partial failure of the membrane [7]. Zeng et al. also found that SCF completely decomposed after annealing in CO_2 at 950°C [8].

Recently, high valence ions such as Ti^{4+} and Ta^{5+} have been reported to have positive effect on the phase stability and CO_2 tolerance of some MIECs. Zeng et al. have found that Ti doping considerably decreased the reaction between CO_2 and SCF [8], while Wang's group has been reported that introduction of Ta into $SrCoO_{3-\delta}$ improves phase stability and reversibility in air [9], and Ta containing $BaCo_{0.7}Fe_{0.2}Ta_{0.1}O_{3-\delta}$ also exhibits high stability, high permeability and a low thermal expansion coefficient [10]. Bi et al. also found that partial substitution of Ce by Ta

strongly increased the chemical stability of $BaCe_{0.8}Y_{0.2}O_{3-\delta}$ against CO_2 [11], and they claimed that the relatively high electronegativity of Ta decreased the basicity of $BaCe_{0.8}Y_{0.2}O_{3-\delta}$, and consequently increased the chemical stability in a CO_2 environment. So it is reasonable to make the assumption that partial substitution of the B-site Co and Fe in SCF by Ta may increase its phase stability and CO_2 tolerance.

In this work, 10% of the Co and Fe cations in SCF were substituted by Ta, aiming to increase to the stability of SCF in CO_2 atmosphere. Both isothermal gravimetric and XRD were used to study the effect of Ta doping on phase stability, while oxygen permeation measurements were performed to examine permeation performance under operating conditions.

4.2 Experimental

$SrCo_{0.8}Fe_{0.2}O_{3-\delta}$ (SCF) and $Sr(Co_{0.8}Fe_{0.2})_{0.9}Ta_{0.1}O_{3-\delta}$ (SCFTa) powders were synthesized using an EDTA complexation/pyrolysis process [12]. Required quantity of $SrCO_3$ were dissolved in diluted nitric acid and appropriate amounts of $Co(NO_3)_2$, $Fe(NO_3)_3$ solutions and EDTA (metal-cation: EDTA=1:1) were added. The pH of the solution was adjusted to 2 with ammonia and finally Ta_2O_5 was added. The mixture was evaporated at 80^oC while stirring until a viscous resin was obtained and subsequently heated on a hot plate, resulting in a rapid and vigor auto-ignition. The resultant powder was calcined at 1000^oC for 5 h. The calcined powders were pressed uni-axially at 4 MPa into disk shapes, subsequently cold isostatically pressed at 300Mpa, and sintered in ambient air at 1200^oC (SCF) or 1237^oC (SCFTa) for 15h.

Densities of the sintered samples were determined using Archimedes method in mercury. The phase composition was analyzed using XRD (Philips X'Pert Pro Super, Cu Kα). The O1s XPS spectra of as-calcined powders were measured using an ESCALAB MK II, VG equipment, and analyzed with the Gaussian peaks software. Isothermal gravimetric analyses were carried out in a home-built apparatus equipped with an analytical balance. About 1 g of powder was placed in a quartz sample holder suspended from the bottom of the balance with a hooked quartz stick, and was heated

in flowing air to 900ºC. When the sample mass reached a constant value at 900ºC, a CO_2 stream was introduced instead of air and the mass change was recorded and sampled by a computer.

Thermal expansion measurements were conducted using a dilatometer (NETZSCH DIL 402C) at a heating/cooling rate 3 °C. First, sintered SCF and SCFTa samples were heated to 1000ºC in nitrogen (pO_2 ~10^{-4} atm) and then cooled to room temperature also in nitrogen. After that, the as-annealed samples were heated to 1000ºC again in nitrogen and the thermal expansion was recorded.

The experimental setup for oxygen permeation measurements is schematically shown in Figure 4.1. Disk-shaped samples with a diameter of 15 mm and a relative density > 90 % were polished to a thickness of 1 mm and ultrasonically cleaned in ethanol. The membranes were sealed to one end of an alumina tube at 1020ºC using a glass ring as sealant. After sealing, the temperature was lowered to 900ºC, and air was fed to one side of the sample (100ml/min), while He or CO_2 (50ml/min) was led over the other (permeate) side to carry away the permeated oxygen. The composition of the effluent stream at the permeate side was analyzed by an online gas chromatograph (Ke Xiao instrument China GC-1690T). The oxygen flux was corrected for any oxygen leakage through the glass sealant or imperfection in the pellet by measuring the concentration of nitrogen in the effluent stream. The amount of leakage oxygen is typically less than 5% of the total amount of the permeated oxygen.
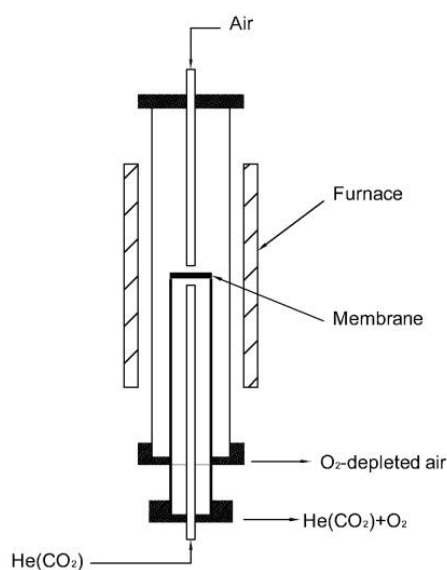
Figure 4.1. Schematic diagram of the high temperature permeation setup

4.3 Results and Discussion

4.3.1 Phase composition and thermal expansion

Figure 4.2 shows the room temperature XRD patterns of as-calcined SCF and SCFTa powders. The XRD patterns can be indexed as cubic perovskite, and there is no evidence of second phase, indicating that a phase pure perovskite structure can be obtained by the synthesis method described above.
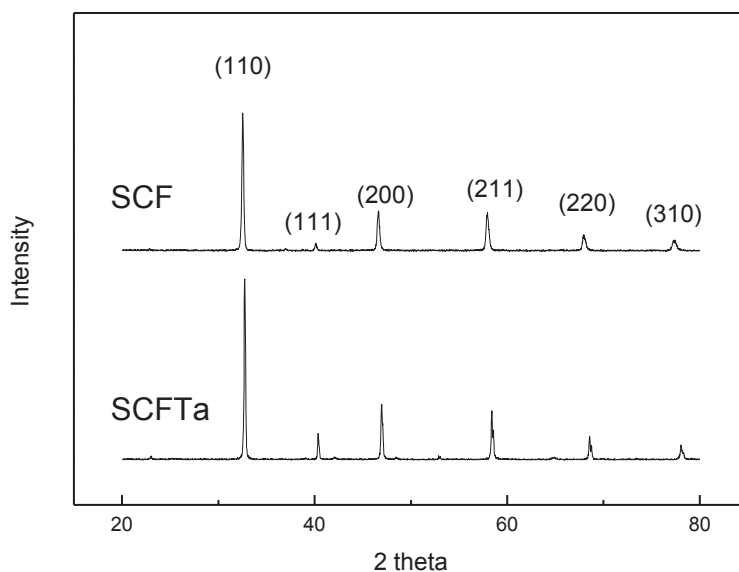
Figure 4.2. XRD patterns of as-calcined SCF and SCFTa. All peaks are indexed in cubic setting

For SCF, it is well known that, during heating, a phase transition from the brownmillerite to the perovskite crystal structure occurs around 790°C when pO_2 is less than 10^{-2} atm [13-16], accompanied by a sudden volume decrease of more than 1% which may result in cracking of the membrane. Because of the sudden expansion during the formation of the perovskite crystal structure, analyzing the thermal expansion as function of temperature is a simple tool for detecting whether a membrane experiences this phase transition. Such a sudden expansion is even better visible when the derivative of the expansion as function of temperature is depicted. Thermal expansion measurements for both SCF and SCFTa were conducted and the results are shown in Figure 4.3. A sudden large shrinkage for un-doped SCF at around 760°C is observed which can be identified as the phase transition from the orthorhombic brownmillerite to the cubic perovskite structure. In previous work [17], we have found that addition of Zr increases the phase stability of SCF in a nitrogen atmosphere and decreases the volume change. However, still a small change in thermal expansion occurs when 4% Zr (the solubility limit in SCF) was added. While, no such shrinkage is observed for SCFTa (see Figure 4.3), suggesting that Ta

doping can completely prevent the phase transition.
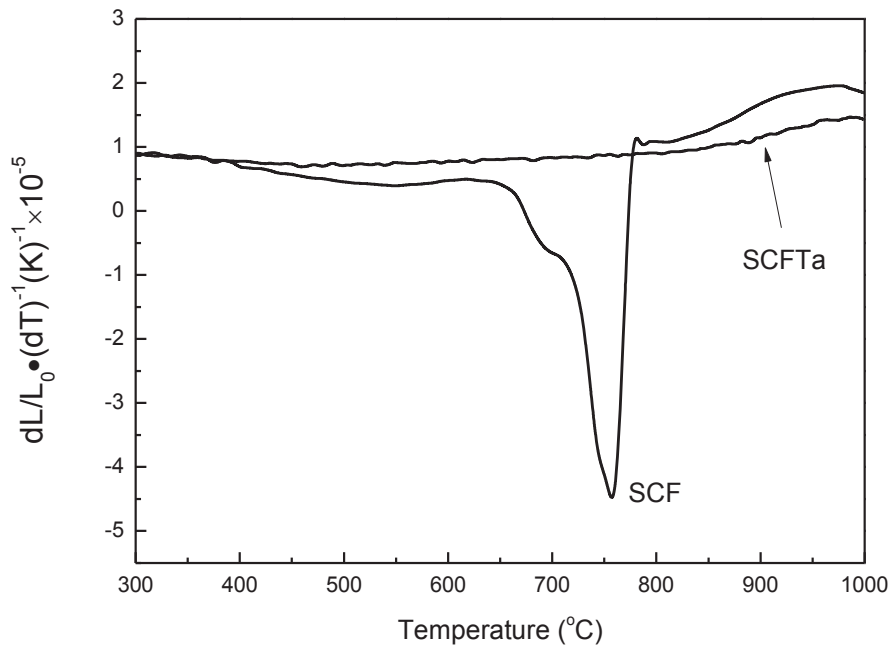
Figure 4.3. Derivative of the expansion as function of temperature of SCF and SCFTa (in nitrogen)

4.3.2 Effect of Ta-doping on the reaction between SCF powders and CO$_2$

Isothermal gravimetric analysis of SCF and SCFTa powders in CO$_2$ atmosphere at 900°C are given in Figure 4.4. The mass of the SCF powder immediately increased upon exposure to pure CO$_2$ at 900°C, resulting in a mass gain of 14.5% after 18 hours. While the Ta-doped SCF powder showed a slight increase in mass of only 1.7% after 17 hours of CO$_2$ exposure. Obviously, the reaction between SCF and CO$_2$ is largely restrained by the doping of Ta to SCF. After the isothermal gravimetric analysis, the samples were cooled to room temperature in CO$_2$ atmosphere and X-ray powder diffraction measurements were conducted to study the phase composition. The results given in Figure 4.5 show that the SCF sample completely decomposed into strontium carbonates and iron/cobalt oxides, which is in accordance with the work of Rui [18] and Yang [19]. For the Ta-doped SCF, only a small amount of SrCO$_3$ was present but this could be regarded as an extremely small amount, while

65

the perovskite structure of SCFTa was largely preserved.
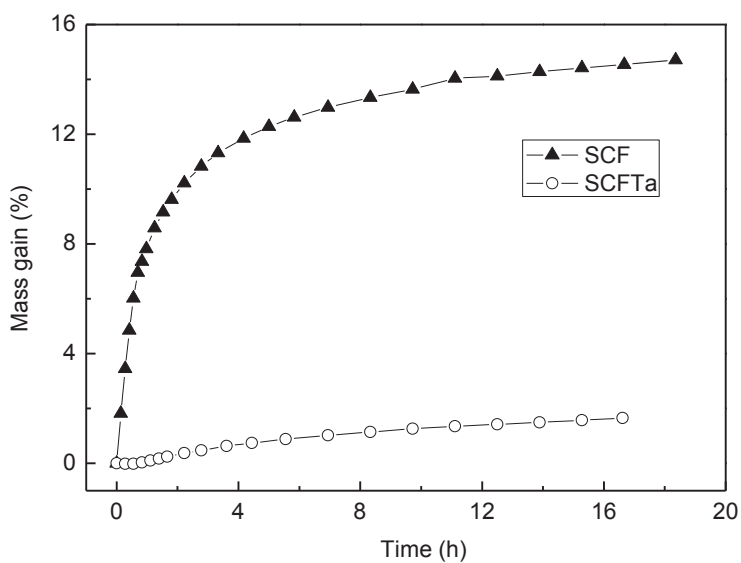
Figure 4.4. Mass change of SCF and SCFTa powder samples upon exposure to CO_2 at 900°C
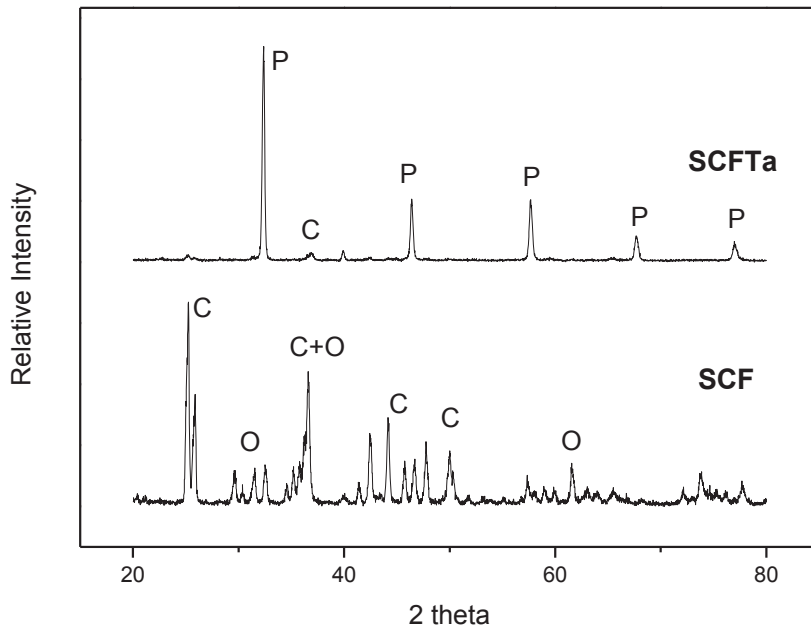
Figure 4.5. XRD patterns of SCF and SCFTa after isothermal gravimetric analysis in CO_2 atmosphere at 900°C for 19 and 17 hours respectively and subsequently cooled to room temperature in CO_2. P: perovskite; C: $SrCO_3$; O: metal-oxides

The general reaction between SCF or SCFTa and CO_2 can be written as follow [20]:

$$SrCo_{0.8}Fe_{0.2}O_{3-\delta}+CO_2 \leftrightarrow$$

$$SrCO_3+0.1Fe_2O_3+0.8CoO+\frac{0.9\text{-}\delta}{2}O_2 \qquad (4.1)$$

$$Sr(Co_{0.8}Fe_{0.2})_{0.9}Ta_{0.1}O_{3-\delta}+CO_2 \leftrightarrow$$

$$SrCO_3+0.09Fe_2O_3+0.72CoO+0.05Ta_2O_5+\frac{0.76\text{-}\delta}{2}O_2 \qquad (4.2)$$
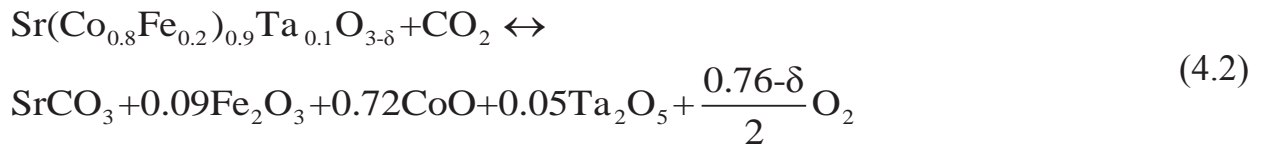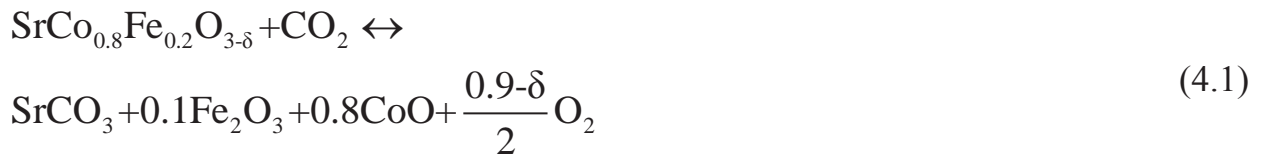
If δ is assumed to be 0.5 [21], as mentioned in , it can be calculated from these chemical reactions in combination with the mass loss as determined by isothermal gravimetric analysis (Figure 4.2) that over 85% (mole) of SCF has decomposed, while this decomposition less than 8% for SCFTa. Generally, the chemical reactions as given in eq. (4.1) and (4.2) can be regarded as a Lewis acid-base reaction, where CO_2 acts as the acid while the metal oxides represent the solid base [11]. The intensity of this reaction is determined by the basicity of the metal oxides, and it is well known that the basicity of a metal oxide is defined as the ability of these species to donate electrons to an adsorbed molecule (in this case CO_2). In general, the O1s binding energy (O1s BE), which is related to the charge density around the oxide ions, is usually used as a measure for the basicity of metal oxides [22, 23]. A higher O1s BE means a lower charge density and consequently it is harder for the oxides to donate electrons to the adsorbed molecule. In this work, the O1s BE of SCF and SCFTa were measured by X-ray Photoelectron Spectroscopy (XPS). The XPS spectra of the O1s BE signals are shown in Figure 4.6, and all specific data are summarized in table 4.1.
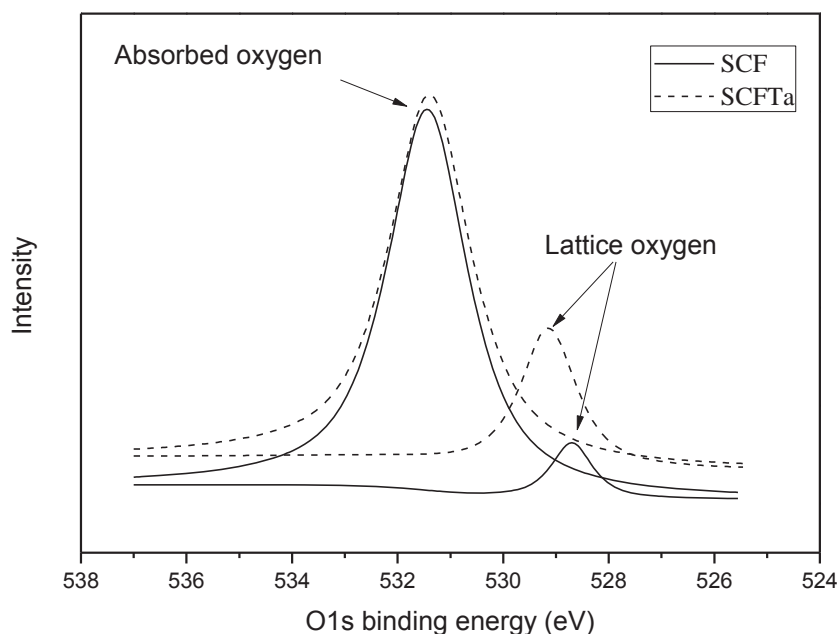
Figure 4.6. O1s binding energy of lattice oxide ions and absorbed oxygen of SCF and SCFTa powders as determined by XPS

Table 4.1. O1s binding energies of SCF and SCFTa

	Absorbed oxygen (eV)	Lattice oxygen (eV)
SCF	531.4	528.7
SCFTa	531.4	529.1

The peak at 531.4 eV is assigned to oxygen absorbed on the particle surface [8], which is identical for both SCF and SCFTa. However, the peak for lattice oxygen of SCFTa in XPS shifts to a higher value by 0.4 eV compared with pure SCF, indicating that the electron donating capacity of SCFTa is less and consequently its basic character is weaker than that of SCF. One possible reason for the lower basicity of SCFTa is that the Ta-O bond strength of 799.1 kJ/mol is much higher than that of Co-O (384.5 kJ/mol) and the Fe-O bond (390.4 kJ/mol) [24]. So, partial substitution of Co and Fe, as present on the B-sites of SCF, by Ta increases the average B-O bond strength and consequently decreases the surface charge density, leading to a decrease of the basicity of SCF.

4.3.3 Oxygen permeation
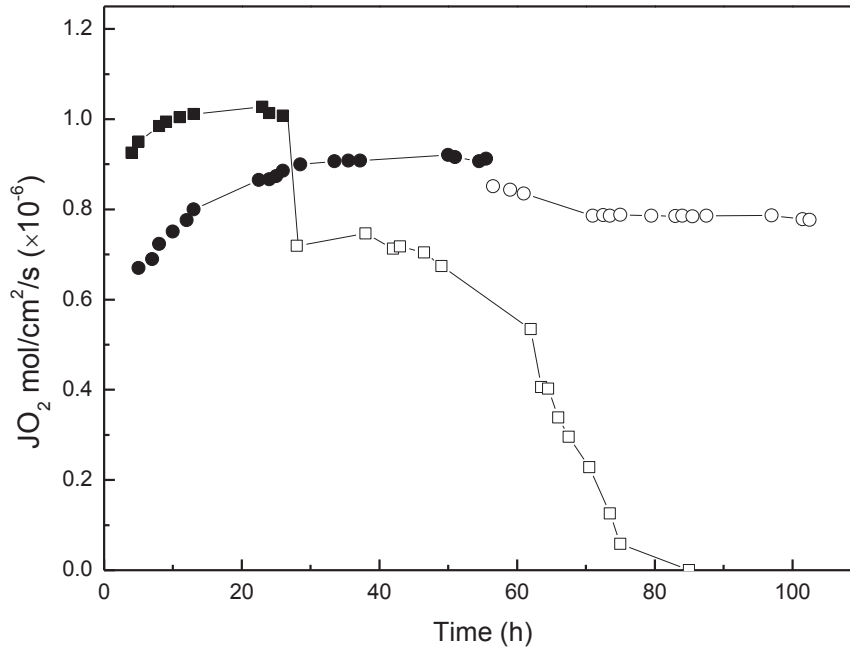
Figure 4.7. Time dependence of oxygen permeation flux through 1 mm membranes at 900oC; Sweep gas flow rate (He, CO2): 50ml/min
■: SCF in He; □: SCF in CO2; ●: SCFTa in He; ○: SCFTa in CO2

To examine the oxygen permeation performance of SCF and SCFTa membranes under operating conditions, i.e. in a CO_2 atmosphere, long term oxygen permeation measurements were performed at 900°C under air/CO_2 gradient (air flow rate 100 ml/min). The results, as given in Figure 4.7, showed a permeability of around 1×10^{-6} mol/cm^2/s for SCF when helium (50 ml/min) was used as sweep gas, which is in accordance with literature [15]. However, when CO_2 (50 ml/min) was introduced, the flux suddenly dropped to 7.2×10^{-7} mol/cm^2/s, followed by a decrease to almost zero after 57 hours of CO_2 exposure at the sweep side of the membrane. For SCFTa, it took almost 30 hours to achieve a steady oxygen permeation flux in helium, which has also been found by Zhu and Yi in their work [25, 26]. This could be due to readjusting of the lattice structure from the as-prepared state to a steady state under permeation conditions or to a reduction of the initial surface oxygen desorption rate.

When CO_2 was introduced as sweep gas instead of helium, the oxygen permeation flux dropped from 9×10^{-7} mol/cm^2/s to 8.5×10^{-7} mol/cm^2/s. This drop in permeation is much lower than that of SCF. Even more important is that the flux remained almost constant during the following 50 hours (7.8×10^{-7} mol/cm^2/s after 50 hours). Overall, it is worthwhile to get a stable membrane at the expense of sacrificing a little of permeability because stability is of top importance in industry. The good performance of SCFTa undoubtedly suggests that SCFTa should be a promising material for oxygen production in the oxy-fuel process.

4.4 Conclusion

The phase transition from perovskite to brownmillerite at low oxygen partial pressure ($pO_2 < 10^{-2}$ atm) can effectively be restrained by substitution of Co and Fe with 10 % Ta at the B site of $SrCo_{0.8}Fe_{0.2}O_{3-\delta}$ (SCF). Oxygen permeation measurements were conducted and the results showed that the Ta-doped SCF possessed much better long-term stability in a CO_2 atmosphere than pure SCF. A possible reason is that Ta doping decreases the basicity of SCF, which restrains the acid-base reaction of CO_2 with SCF. Actually, the decrease of basicity has been proven by XPS analysis. To sum up, the good performance of SCFTa in reducing atmosphere as well as in CO_2 atmosphere makes this material an interesting candidate as membrane in the oxy-fuel combustion process.

References

[1]   B.J.P. Buhre, L.K. Elliott, C.D. Sheng, R.P. Gupta, T.F. Wall, Oxy-fuel combustion technology for coal-fired power generation, Progress in Energy and Combustion Science, 31 (2005) 283-307.

[2]   H.M. Kvamsdal, K. Jordal, O. Bolland, A quantitative comparison of gas turbine cycles with CO_2 capture, Energy, 32 (2007) 10-24.

[3]   P.A. Armstrong, E.P. Foster, H.H. Gunardson, ITM oxygen for gasification, in, 2005, pp. B17-B22.

[4]   S.G. Sundkvist, T. Griffin, N.P. Thorshaug, AZEP-Development of an Integrated Air Separation Membrane-Gas Turbine, Second Nordic Minisymposium on Carbon Dioxide Capture and Storage, (2001).

[5]   T. Griffin, S.G. Sundkvist, K. Asen, T. Bruun, Advanced zero emissions gas turbine power plant, J Eng Gas Turb Power, 127 (2005) 81-85.

[6]   S.G. Sundkvist, H. Eklund, AZEP -an EC funded project for development of a CCGT power plant without CO$_2$emissions, 4th Nordic Minisymposium on CO$_2$ Capture and Storage, (2005).

[7]   J.X. Yi, S.J. Feng, Y.B. Zuo, W. Liu, C.S. Chen, Oxygen permeability and stability of Sr$_{0.95}$Co$_{0.8}$Fe$_{0.2}$O$_{3-\delta}$ in a CO$_2$- and H$_2$O-containing atmosphere, Chem Mater, 17 (2005) 5856-5861.

[8]   Q. Zeng, Y.B. Zu, C.G. Fan, C.S. Chen, CO$_2$-tolerant oxygen separation membranes targeting CO$_2$ capture application, Journal of Membrane Science, 335 (2009) 140-144.

[9]   X. Chen, L. Huang, Y. Wei, H. Wang, Tantalum stabilized SrCoO$_{3-\delta}$perovskite   membrane   for oxygen separation, Journal of Membrane Science, 368 (2011) 159-164.

[10] H.X. Luo, B.B. Tian, Y.Y. Wei, H.H. Wang, H.Q. Jiang, J. Caro, Oxygen Permeability and Structural Stability of a Novel Tantalum-Doped Perovskite BaCo$_{0.7}$Fe$_{0.2}$Ta$_{0.1}$O$_{3-\delta}$, Aiche J, 56 (2010) 604-610.

[11] L. Bi, S. Zhang, S. Fang, Z. Tao, R. Peng, W. Liu, A novel anode supported BaCe$_{0.7}$Ta$_{0.1}$Y$_{0.2}$O$_{3-\delta}$ electrolyte membrane for proton-conducting solid oxide fuel cell, Electrochem Commun, 10 (2008) 1598-1601.

[12] M. Liu, R. Wang, D.F. Li, D.T. Liang, A novel combustion route for the preparation of perovskite-type oxygen permeable materials, Materials Chemistry and Physics, 102 (2007) 132-139.

[13] W.T.A. Harrison, T.H. Lee, Y.L. Yang, D.P. Scarfe, L.M. Liu, A.J. Jacobson, A Neutron-Diffraction Study of 2 Strontium Cobalt Iron-Oxides, Mater Res Bull, 30 (1995) 621-630.

[14] L.M. Liu, T.H. Lee, L. Qiu, Y.L. Yang, A.J. Jacobson, A thermogravimetric study of the phase diagram of strontium cobalt iron oxide, SrCo$_{0.8}$Fe$_{0.2}$O$_{3-\delta}$, Mater Res Bull, 31 (1996) 29-35.

[15] L. Qiu, T.H. Lee, L.M. Liu, Y.L. Yang, A.J. Jacobson, Oxygen Permeation Studies of SrCo$_{0.8}$Fe$_{0.2}$O$_{3-\delta}$, Solid State Ionics, 76 (1995) 321-329.

[16] S. McIntosh, J.F. Vente, W.G. Haije, D.H.A. Blank, H.J.M. Bouwmeester, Structure and oxygen stoichiometry of SrCo$_{0.8}$Fe$_{0.2}$O$_{3-\delta}$ and Ba$_{0.5}$Sr$_{0.5}$Co$_{0.8}$Fe$_{0.2}$O$_{3-\delta}$, Solid State Ionics, 177 (2006) 1737-1742.

[17] W. Chen, Y.B. Zuo, C.S. Chen, A.J.A. Winnubst, Effect of Zr4+ doping on the oxygen stoichiometry and phase stability of SrCo$_{0.8}$Fe$_{0.2}$O$_{3-\delta}$ oxygen separation membrane, Solid State Ionics, 181 (2010) 971-975.

[18] Z.B. Rui, J.J. Ding, Y.D. Li, Y.S. Lin, SrCo$_{0.8}$Fe$_{0.2}$O$_{3-\delta}$ sorbent for high-temperature production of oxygen-enriched carbon dioxide stream, Fuel, 89 (2010) 1429-1434.

[19] Q. Yang, Y.S. Lin, M. Bülow, High temperature sorption separation of air for producing oxygen-enriched CO$_2$ stream, Aiche J, 52 (2006) 574-581.

[20] H.J. Freund, M.W. Roberts, Surface chemistry of carbon dioxide, Surf Sci Rep, 25 (1996) 225-

273.

[21] S. McIntosh, J.F. Vente, W.G. Haije, D.H.A. Blank, H.J.M. Bouwmeester, Structure and oxygen stoichiometry of $SrCo_{0.8}Fe_{0.2}O_{3-\delta}$ and $Ba_{0.5}Sr_{0.5}Co_{0.8}Fe_{0.2}O_{3-\delta}$, Solid State Ionics, 177 (2006) 1737-1742.

[22] V. Dimitrov, T. Komatsu, Correlation between O1s binding energy and metal binding energy in XPS spectra of oxide glasses, Phys Chem Glasses, 44 (2003) 401-408.

[23] H. Fan, G. Wang, L. Hu, Infrared, Raman and XPS spectroscopic studies of Bi_2O_3–B_2O_3–Ga_2O_3 glasses, Solid State Sci, 11 (2009) 2065-2070.

[24] I. CRC Press, Handbook of Chemistry and Physics, Handbook of Chemistry and Physics, (2000).

[25] J.X. Yi, Y.B. Zuo, W. Liu, L. Winnubst, C.S. Chen, Oxygen permeation through a $Ce_{0.8}Sm_{0.2}O_{2-\delta}$-$La_{0.8}Sr_{0.2}CrO_{3-\delta}$ dual-phase composite membrane, Journal of Membrane Science, 280 (2006) 849-855.

[26] X.F. Zhu, W.S. Yang, Composite membrane based on ionic conductor and mixed conductor for oxygen permeation, AIChE, 54 (2008) 665-672.

Chapter 5 Oxygen-selective membranes integrated with oxy-fuel combustion

Abstract:

The perovskite-type oxide $SrCo_{0.8}Fe_{0.2}O_{3-\delta}$ (SCF), a highly oxygen-permeable material, is restricted for application in the membrane-integrated oxy-fuel combustion process by its low tolerance to CO_2. In the present work, we found that the CO_2 tolerance of SCF is improved by increasing the oxygen partial pressure in the CO_2-containing gas. Long term oxygen permeation experiments, at 950 ºC, showed that mixing 5 % of oxygen into the CO_2 sweep gas effectively prevents degradation of the SCF membrane. X-ray photoelectron spectroscopy it was indicates that the increase in CO_2 tolerance of SCF is caused by a decrease in basicity of the material with increasing oxygen partial pressure. Based on these experimental results, a modified oxy-fuel combustion process is proposed. Calculation of the required membrane area for operating a 50 MW coal-fired power plant showed that the modified process comprises a viable option.

5.1 Introduction

Oxy-fuel combustion is a promising technique for CO_2 capture in a fossil fuel-fired power plant. In a typical oxy-fuel combustion process, pure oxygen instead of air is used for fuel combustion, resulting in a concentrated CO_2 gas stream, thus enabling efficient CO_2 capture. In most cases pure oxygen is separated from air via the cryogenic distillation or the pressure swing adsorption (PSA) process. Both processes are energy intensive, which limits further development of the oxy-fuel combustion technique [1, 2]. It is proposed that oxygen can be produced by using mixed ionic-electronic conducting (MIEC) ceramic membranes, through which (neutral) oxygen transport at elevated temperatures (usually higher than 700 ºC) [3, 4]. A general scheme of this process is given in Figure 5.1. The oxygen, as separated from air by the membrane, is carried by the sweep gas CO_2, while the CO_2/O_2 gas mixture is used to combust the fossil fuel. After combustion and purification, the exhaust gas mainly consists of CO_2 (> 95 %). Part of the CO_2 is recycled as sweep gas and the rest is compressed for delivery and storage.
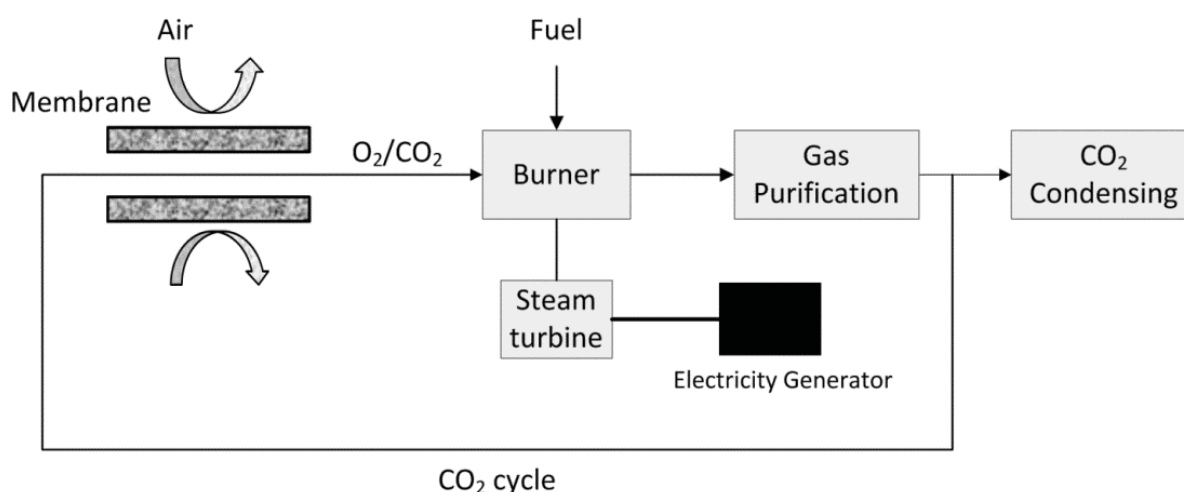
Figure 5.1. Scheme for membrane integrated oxy-fuel combustion process.

Most MIEC materials have the perovskite crystal structure and contain alkaline-earth elements like Ca, Sr or Ba. Due to the presence of these elements, a carbonation reaction tends to occur when these membranes are exposed to a CO_2-containing atmosphere. This reaction results in the formation of an alkaline-earth carbonate

layer on the membrane surface, which is impermeable for oxygen, resulting in a decline in oxygen flux or even to a non-permeating membrane. For example, $SrCo_{0.8}Fe_{0.2}O_{3-\delta}$ (SCF), a highly oxygen-permeable material, showed a decrease in oxygen flux to almost zero within 100 hours when using CO_2 as sweep gas [5]. In order to increase the CO_2 tolerance of SCF membranes, Sr^{2+} was partially substituted with La^{3+} [6], or Co/Fe with Ti^{4+}, Zr^{4+}, Ta^{5+} or Nb^{5+} [7, 8]. However, this improvement in CO_2 tolerance was at the expense of a decrease in oxygen flux [9].

Besides partial substitution, there are other parameters that affect the CO_2 tolerance of SCF, for example, temperature and CO_2 partial pressure (pCO_2). Yi et al. [10] found that SCF is more stable at higher temperature and lower pCO_2 (balanced with helium), and suggested SCF membranes should be operated above 900 ºC. In the present study we examined another possible parameter: the oxygen partial pressure (pO_2), which has not been reported before to the best of our knowledge, as a way to improve the CO_2 tolerance of alkaline-earth containing perovskite materials. In this study thermal-gravimetric analysis (TGA) was used to investigate the effect of pO_2 on the stability of the SCF perovskite system in a CO_2-containing atmosphere. X-ray photoelectron spectroscopy (XPS) was used to examine the oxygen bonding energy of SCF at different oxygen partial pressures. Oxygen permeation experiments were performed to test the CO_2 tolerance of SCF membranes under operating conditions by adding 0 % or 5 % of oxygen to the sweep gas (CO_2). Finally, we propose a modified oxy-fuel combustion process and estimated the SCF membrane area needed in a combustion process for a 50 MW coal-fired power plant.

5.2 Experimental procedure and methodology

5.2.1 Sample preparation

$SrCo_{0.8}Fe_{0.2}O_{3-\delta}$ (SCF) was synthesized using an EDTA complexation/pyrolysis process. Metal nitrates were dissolved at a stoichiometric ratio in demineralized water under stirring. EDTA, dissolved in ammonium hydroxide, was added for

chelating and after several minutes citric acid was added as well. The molar ratio of total metal ions : citric acid : EDTA was 1.0 : 1.5 : 1.0. The pH of the solution was adjusted to 6 by adding ammonium hydroxide. Subsequently NH_4NO_3 was added as an ignition aid at an amount of 100 g NH_4NO_3 per 0.1 mole of metal ions. The final solution was heated at 120-150 °C under stirring to evaporate water until the system changed into a viscous gel, which was transferred to a stainless steel vessel and heated on a hot plate at a temperature of around 500 ºC, while a vigorous combustion took place, resulting in a fluffy powder. The powder was collected and calcined at 950 ºC for 5 hours at a heating and cooling rate of 3 °C/min. The calcined powders were uniaxially pressed at 4 Mpa into disk-shaped membranes, subsequently cold isostatically pressed at 400 Mpa for 6 minutes, and sintered in ambient air at 1200 °C for 10 hours at a heating rate of 3 °C/min and a cooling rate of 2 °C/min.

5.2.2 Thermal-gravimetric analysis (TGA)

Isothermal gravimetric analyses were carried out on a Netzsch TG 449 F3 Jupiter®. About 20 mg of powder was weighed in an alumina crucible and placed in the TGA setup. The system was heated to 950 ºC in flowing 'synthetic' air (95 ml/min N_2 and 25 ml/min O_2; all gas flow rates are given under standard temperature and pressure without further notation) at a heating rate of 10 °C/min. The system was isothermally held for 1 hour in order to attain equilibrium, indicated by a constant weight of the sample. Subsequently the sweep gas was changed to a $CO_2/O_2/N_2$ mixture (total flow rate 120 ml/min with a CO_2 flow rate 80 ml/min; O_2 flow rate is variable and N_2 is used as balance). After 5 hours, the system was cooled down at 10 °C/min in the same flowing gases. All TGA data were processed with a correction file of a blank crucible using the same temperature program, to exclude background data of the equipment.

5.2.3 X-ray photoelectron spectroscopy analysis

For X-ray photoelectron spectroscopy (XPS: ESCALAB MK II, VG equipment)

analysis SCF bars (8 mm × 4 mm × 3 mm) were prepared using the same procedure as for the disk-shaped membranes. After sintering and polishing to the desired dimensions, the samples were annealed in nitrogen ($pO_2 = 10^{-4}$ bar) or oxygen ($pO_2 = 1.0$ bar) at 950 °C for 20 hours and quenched to room temperature within a few seconds. Afterwards, the bars were broken and only the center part of the cross section was analyzed by XPS using an X-ray beam size of 250 μm and a step size of 0.05 eV.

5.2.4 Oxygen permeation measurements
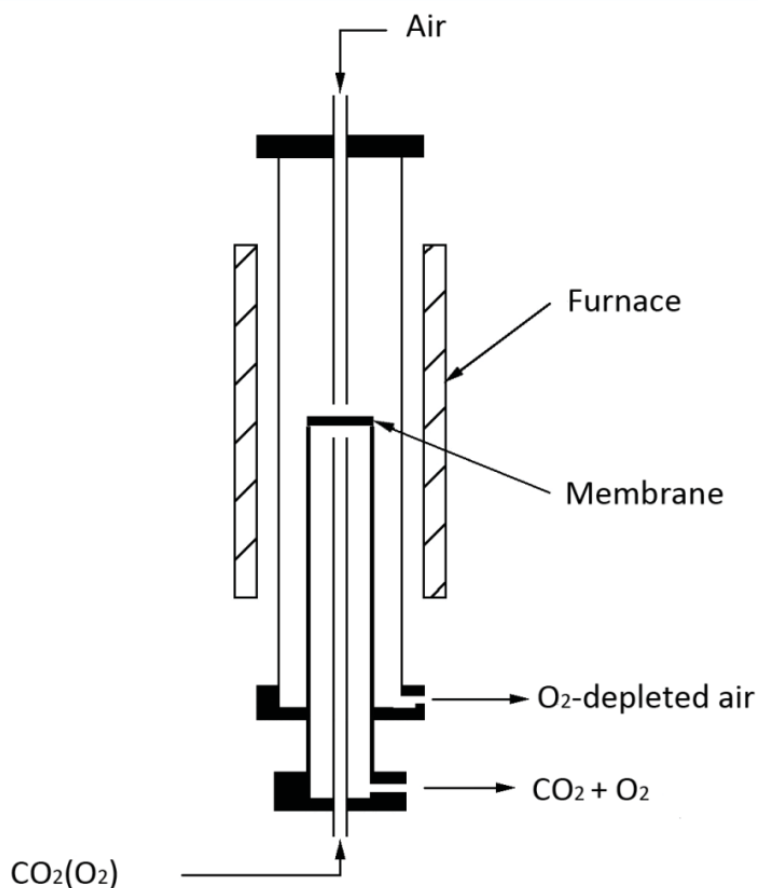
Figure 5.2. Schematic diagram of the high temperature permeation setup.

The experimental setup for oxygen permeation measurements is schematically shown in Figure 5.2. Disk-shaped membranes with a diameter of 15 mm and a relative density > 90 % were polished to a thickness of 1 mm and ultrasonically

cleaned in ethanol. The membranes were sealed to one end of a quartz tube (diameter 12 mm) using gold paste and a sealing temperature of 1000 °C. After sealing, the temperature was lowered to 950 °C, and air was applied as feed gas to one side of the membrane (100 ml/min), while CO_2 (50 ml/min) or a CO_2/O_2 gas mixture (50 ml/min) was applied to the other side to sweep away the permeated oxygen. The composition of the effluent gas at the permeate side was analyzed by an oxygen sensor (Systech ZR893). A gas chromatograph (Varian CP 4900 equipped with 5 Å molecular sieve column using He as carrier gas) was used to check for any leakage of the sealing. If there was no nitrogen peak in the spectrum for the permeate gas stream, it was assumed that the sealing was sufficient and oxygen permeation due to leakage was neglected.

5.2.5 Membrane area calculation

The aim of this calculation is to estimate the membrane area needed for a 50 MW coal-fired power plant. This was done in two steps: 1) calculation of the oxygen produced by a single membrane tube and 2) determination of the total required membrane area, necessary for the power plant, based on the calculation for a single tube.

Oxygen production by a single membrane tube
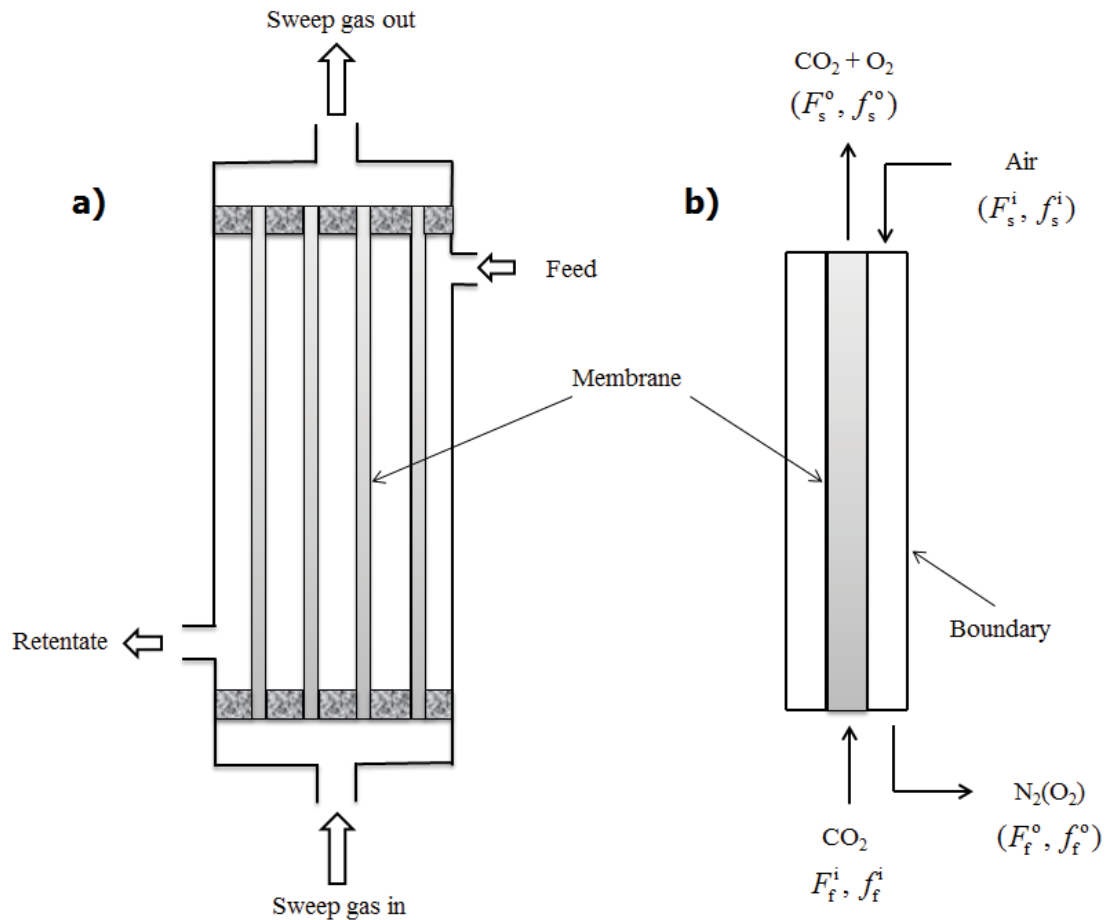
Figure 5.3. Schematic drawing of (a) a membrane module and (b) a membrane tube.

Tubular membranes were chosen in this study and a simple scheme of the membrane module and a membrane tube is shown in Figure 5.3. For the calculation the oxygen production by a single membrane tube, the following assumptions are made: (1) oxygen is transported from the shell side to the core side of the membrane tube; (2) the sweep and feed gas flows are in a counter-current mode; (3) there is no oxygen concentration polarization in the radial direction; (4) the absolute pressure drop in the membrane module is neglected; (5) the oxygen transport in both core and shell side of the membrane is described by a convection diffusion and a reaction model (eq. (5.1) - (5.2)) [11]; (6) the oxygen flux is governed by Wagner's equation (eq. (5.3)) [12], in which the electronic conductivity of the membranes is predominant and the ionic conductivity constant.

$$D_s \frac{d^2 f_s}{dz^2} - \frac{d}{dz}(\vec{v}_s f_s) + \frac{2V_m}{R_1}\vec{J}_{O_2} = 0 \qquad (5.1)$$

$$D_f \frac{d^2 f_f}{dz^2} - \frac{d}{dz}(\vec{v}_f f_f) + \frac{2R_1 V_m}{R_2^2 - R_1^2}\vec{J}_{O_2} = 0 \qquad (5.2)$$

where

$$\begin{cases} \vec{J}_{O_2} = \frac{RT}{(4F_a)^2 d}\sigma_{ion}\ln(\frac{P_f f_f}{P_s f_s}) \\ \\ \vec{v}_s = \frac{\vec{F}_s}{\pi R_1^2} \\ \\ \vec{v}_f = \frac{\vec{F}_f}{\pi(R_2^2 - R_1^2)} \end{cases} \qquad (5.3)$$

with Danckwerts boundary conditions [13],

$$\begin{cases} \vec{v}_s f_s^i = \vec{v}_s f_s - D_s \dfrac{df_s}{dz}, & z = 0 \\ \\ \dfrac{df_s}{dz} = 0, & z = L \\ \\ \dfrac{df_f}{dz} = 0, & z = 0 \\ \\ \vec{v}_f f_f^i = \vec{v}_f f_f - D_f \dfrac{df_f}{dz}, & z = L \end{cases} \qquad (5.4)$$

Where f, D, P, F and $\vec{v}$ are O_2 mole fractions, O_2 diffusion coefficients in the gas phase, absolute pressure, volume flow rate and velocity of the sweep (with subscript s) gas or feed (with subscript f) gas; R gas constant, z the coordinates along the membrane tube, T absolute temperature, V_m molar volume of oxygen in the gas phase oxygen at given temperature and pressure, F_a Faraday constant, d membrane thickness, σ_{ion} oxygen ionic conductivity, R_1 the radius of the tube membrane

(average of outer and inner diameter) and R_2 the distance from center of the tube membrane to the wall boundary (Figure 5.3). f_s^i, f_f^i f_s^i and f_f^i are the O_2 mole fractions at the inlet (with superscript i) and outlet (with superscript o) of sweep gas and feed gas and L the length of the membrane tube.

Eq. (5.1)-(5.2), in combination with the boundary conditions as given in eq. (5.4), can be numerically solved if sweep/feed gas flow rates *(F)* and their O_2 mole fractions *(f)* at the inlet of the membrane tube are known ($F_s^i, F_f^i, f_s^i, f_f^i$). From these results gas flow rates and O_2 mole fractions at the outlet of the membrane tube can be calculated ($F_s^o, F_f^o, f_s^o, f_f^o$). In most cases, f_s^i and f_f^i are fixed, while F_s^i and F_f^i can be adjusted if necessary. For example, if a certain O_2 mole fractions (f_s^o, f_f^o) in the sweep/feed gas at the outlet of the membrane tube is required, appropriate F_s^i and F_f^i values have to be chosen. In this study. In this work f_s^o is fixed at a value of 0.35 because it has been reported that a composition of approximately 35 % O_2 and 65 % of CO_2 (v/v) is needed in an oxy-fuel combustion process to ensure the flame temperature and heat capacity of gases to match fuel combustion in air [14]. Besides, f_f^o is kept at a value of 0.02 which means that around 92 % of oxygen in the air is recovered.

As the increase of sweep gas flow rate is caused by the permeated oxygen, the amount of moles of oxygen produced by a single membrane tube, F_{O_2}, can be calculated with eq. (5.5):

$$F_{O_2} = F_s^o - F_s^i \qquad (5.5)$$

Total membrane area calculation

The total membrane area is based on a 50 MW coal-fired power plant. In this power plant, the combustion of coal is described by reaction (6) assuming coal

contains 100 % of carbon.

$$C + O_2 \rightarrow CO_2 \tag{5.6}$$

If it is further assumed that the heat density of coal is 30 MJ/kg (HHV) and the overall efficiency of the power plant is 30 % [15], the total amount of coal needed for one hour operation of this power plant is

$$N_{coal} = \frac{50\ \text{MW} \times 3600\ \text{s}}{30\ \text{MJ/kg} \times 0.3 \times 12\ \text{kg/kmole}} \approx 1667\ \text{kmole} \tag{5.7}$$

The oxygen needed for the combustion of coal has the same mole number. Since the oxygen produced by a single tube membrane is known (eq. (5.5)), the number of tubular membranes, N_m, and also the total membrane area, A, can be calculated:

$$N_m = \frac{F_{O_2}^{T}}{F_{O_2}} \tag{5.8}$$

$$A = 2\pi R_1 L \times N_m \tag{5.9}$$

where $F_{O_2}^{T}$ is the amount of total oxygen needed and F_{O_2} is the amount of oxygen produced by a single membrane tube.

5.3 Results and discussion

5.3.1 Thermal-gravimetric analysis

The calcined SCF powder was checked to have a phase pure perovskite crystal structure by means of XRD. The reaction between SCF and CO_2 was studied by isothermal gravimetric experiments TGA. In Figure 5.4a, the results of TGA experiments at 950 °C are described under varying pO_2 by adjusting the N_2/O_2 ratio and keeping the pCO_2 constant at 0.67 bar. The weight of the SCF powder samples immediately increases upon exposure to a CO_2-containing gas mixture, while the rate of weight gain is different when the experiments were performed at different pO_2 (10^{-4}, 0.05, 0.10 and 0.20 bar); a higher pO_2 leads to a lower reaction rate of CO_2 with the SCF powder sample. After 5 hours, the weight of the samples increased by 15.4 %,

10.4 %, 8.6 % and 6.2 % respectively. Clearly, the reaction between SCF and CO_2 at 950 °C is strongly affected by pO_2.
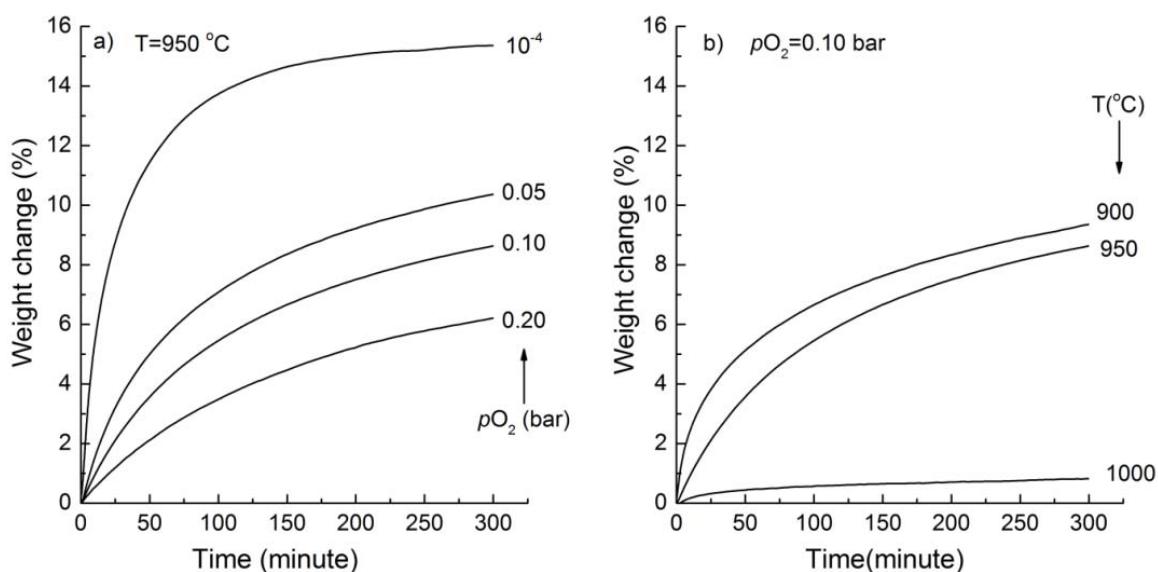
Figure 5.4. Weight change of SCF powder samples under different conditions; a) variation in pO_2; b) variation in temperature. ($pCO_2 = 0.67$ bar in all cases; balance: N_2).

Another parameter that can influence the reaction between SCF and CO_2 is the temperature. At 1000 °C, the reaction was very slow, and after 5 hours, the weight only increased by 0.8 %, compared to 9. 4 % and 8.6 % for 900 °C and 950 °C, respectively, when using a pO_2 of 0.1 bar. A higher temperature leads to a lower reaction rate (Figure 5.4b), which indicates that SCF is more stable at higher temperatures. This result is in accordance with previous data of Yi et al. [10]. A similar trend has been found for other perovskite structures like $BaCe_{0.9}Y_{0.1}O_{3-\delta}$ [16]. A thermodynamic analysis has been performed by Brandão et al. [17] for the explanation of this temperature effect.

5.3.2 XPS analysis
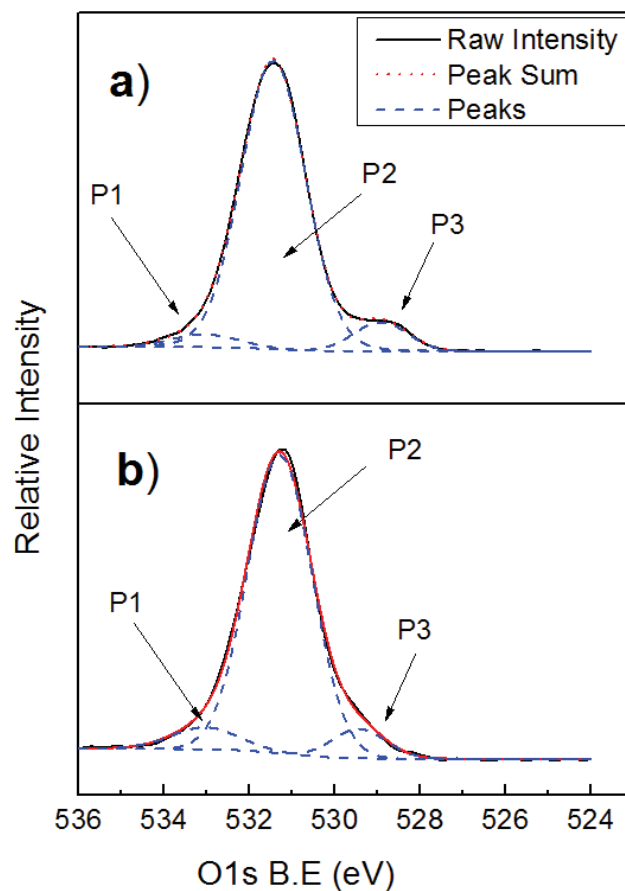
Figure 5.5. O1s binding energy of SCF samples quenched from 950 °C at different pO_2; a) $pO_2 = 10^{-4}$ bar; b) $pO_2 = 1.0$ bar; P1: Absorbed water; P2: Absorbed oxygen; P3: Lattice oxygen. (Details about peak position can be found in the Table 5.1)

Table 5.1. Peak positions of the XPS spectrum as given in Fig. 5.5.

pO_2 (bar)	P1 (eV)	P2 (eV)	P3 (eV)
1×10^{-4} (Fig. 5a)	533.0	531.4	528.9
1.0 (Fig. 5b)	533.0	531.4	529.5

The inhibition of the reaction between SCF and CO_2 can be explained by the Lewis acid–base theory, where CO_2 is regarded as the gas acid and SCF as the solid base [5]. The intensity of this reaction is determined by the basicity of SCF, which

may be different under different conditions, for example, different temperature or pO_2. In general, the basicity of a metal oxide is defined as its ability to donate electrons to an adsorbed molecule (in this case CO_2). The O1s binding energy (O1s BE), which is related to the charge density around the oxide ions, is usually taken as a measure of the basicity of a metal oxide [18, 19]. A higher O1s BE means a lower charge density, consequently, it is more difficult for the oxides to donate electrons to the adsorbed molecules [20], indicating a lower basicity of the metal oxide. To check whether the O1s BE for SCF is pO_2 dependent, we annealed SCF bulk samples in oxygen (pO_2=1 bar) and nitrogen (pO_2=10^{-4} bar) at 950 °C for 20 hours and quenched them to room temperature. XPS analysis was used to determine the O1s BE. The raw XPS data were de-convoluted into three Gaussian peaks (Figure 5.5). The peak at 533.0 eV is assigned to absorbed water, 531.4 eV to oxygen in absorbed oxygen, and 528-530 eV to lattice oxygen [21, 22]. For absorbed water and oxygen, the O1s BE has the same value in both pO_2 cases. For the lattice oxygen an increase in O1s BE from 528.9 eV to 529.5 eV was observed when pO_2 was increased from 10^{-4} to 1 bar. This suggests that the basicity of SCF tends to be lower at higher pO_2, thus lowers the affinity of reaction between SCF and CO_2. This result is in agreement with the TGA analysis (Figure 5a).

5.3.3 Oxygen permeation measurements
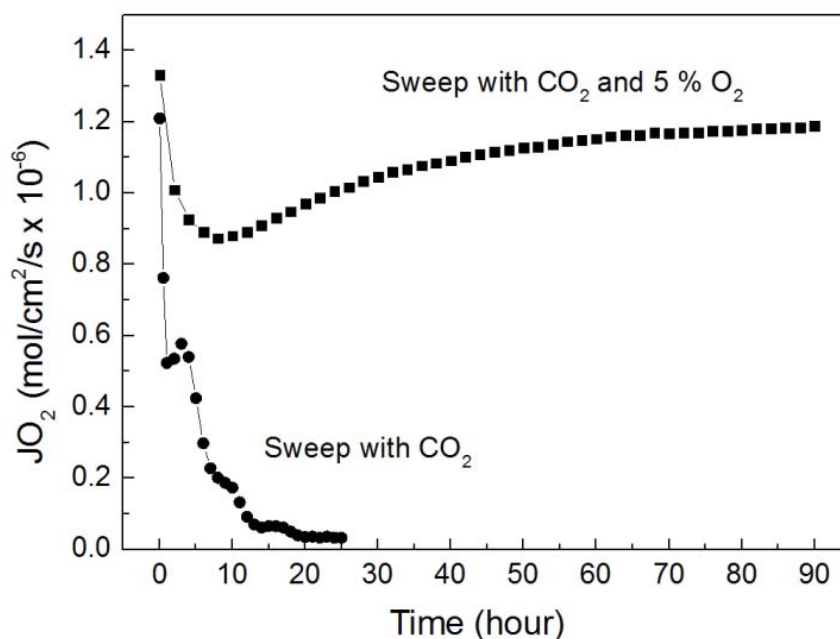
Figure 5.6. Long-term oxygen permeation tests of SCF membranes at 950 °C by using pure CO_2 (circles) or an O_2/CO_2 mixture (squares, O_2 mole fraction 5 %) as sweep gas (50 ml/min for both cases). Feed gas: air. Membrane thickness: 1 mm.

To check the stability of SCF membranes in CO_2 under operating conditions, two long term (90 hours) oxygen permeation measurements were performed, at 950 °C, in CO_2 atmosphere. In the first experiment synthetic air (O_2 20 ml/min and N_2 80 ml/min) was used as feed gas, and pure CO_2 (50 ml/min, $pO_2 \approx 10^{-4}$ bar) was used as sweep gas. In the second experiment, a mixture of O_2/CO_2 (O_2 2.5 ml/min and CO_2 47.5 ml/min) was used as sweep gas, and the feed gas was partly changed (O_2 50 ml/min and N_2 50 ml/min) to ensure a comparable pO_2 gradient across the membrane for both experiments. The results of oxygen permeation measurements, as given in Figure 5.6, show that the SCF membranes behaved quite differently in pure CO_2 than in the CO_2/O_2 mixture. If pure CO_2 is used as sweep gas, the oxygen flux decreased quickly to zero within 25 hours. A similar result has also been reported by Zeng et al. [5]. By using an O_2/CO_2 mixture ($pO_2 = 0.05$ bar) as sweep gas, the oxygen flux decreased by 34 % in the first 10 hours, and slowly recovered to 90 % of its original value in the following 50 hours, and then became constant. Although it is

still not clear what caused the oxygen flux decrease in the first 10 hours, it is obvious that the addition of some oxygen to the sweep gas indeed enhances the CO_2 tolerance of SCF membranes in a CO_2 atmosphere under operating conditions, and thus prevented the oxygen flux from decreasing in the long run. However, as shown in Figure 5.5, the reaction between SCF powder and CO_2 could not be prevented at a temperature of 950 °C by increasing pO_2 up to 0.20 bar, which seems to be in conflict with the oxygen permeation results. This "conflict" is attributed to the dynamic process occurring at the permeate side of the membrane. During an oxygen permeation experiment, oxygen is released from the membrane surface at the permeate side in the form of oxygen molecules, creating a higher oxygen activity at the membrane interface than in the gas bulk phase [23, 24]. This dynamic process, which is different from the stationary environment in the TGA experiments, is beneficial for the membrane stability.

5.3.4 Process design and membrane area calculation
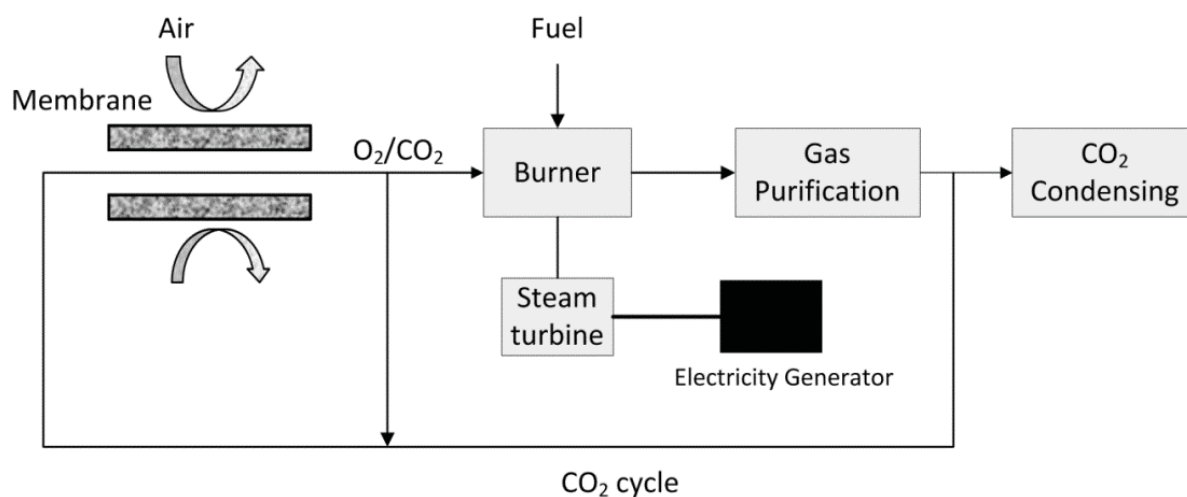
Figure 5.7. A modified process scheme for the membrane integrated oxy-fuel combustion.

Based on these experimental results we propose a new design for a membrane integrated oxy-fuel combustion process (Figure 5.7). In this concept an extra CO_2/O_2 recycle is introduced to increase the pO_2 in the CO_2 sweep gas. This modification

ensures that the pO_2 in the CO_2 sweep gas at the inlet of the membrane module is high enough to protect SCF from degradation by carbonation. However, this modification also leads to an increase of needed membrane area because part of CO_2/O_2 gas stream is used for recycling and the driving force for oxygen permeation is also slightly decreased. In order to quantitatively study this effect, a calculation was performed of the total membrane area needed for a 50 MW coal-fired power plant using O_2 mole fractions in the CO_2 sweep varying from 0.005 to 0.1 (details about this calculation can be found in the experimental procedure and methodology section). The membrane geometry and operating conditions are listed in Table 5.2.

Table 5.2. Membrane geometry and operating conditions of oxygen permeation in a single membrane tube.

Variable	Value	Units
Membrane length (L)	100	cm
Membrane outer diameter	1.0	cm
Membrane inner diameter	0.8	cm
Ionic conductivity	1.0	S/cm
Feed side pressure	10	bar
Sweep side pressure	1.7[*]	bar
Temperature	1223	K
Diffusion coefficient of O_2/N_2	2.19[**]	cm^2/s
Diffusion coefficient of O_2/CO_2	1.55[**]	cm^2/s
O_2 mole fraction of feed gas at inlet (f_f^i)	0.209	-
O_2 mole fraction of sweep gas at inlet (f_s^i)	0.005-0.1	-
O_2 mole fraction of feed gas at outlet (f_f^o)	0.02	-
O_2 mole fraction of sweep gas at outlet (f_s^o)	0.35	-

[*]: Typical pressure for oxy-fuel application [1].

[**]: The binary diffusion coefficients of O_2/N_2 and O_2/CO_2 at 950 °C were calculated with Chapman-Enskog's theory [25].

The results of calculation are given in Figure 5.8. When f_s^i (O_2 mole fraction in CO_2 sweep gas) is increased to 0.05, which has been proven to be sufficient to protect SCF membranes against CO_2 degradation, the total needed membrane area increases from 4.97×10^4 to 5.81×10^4 m^2, so only by ~17 % compared with the (theoretical) case of using pure CO_2 as sweep gas.
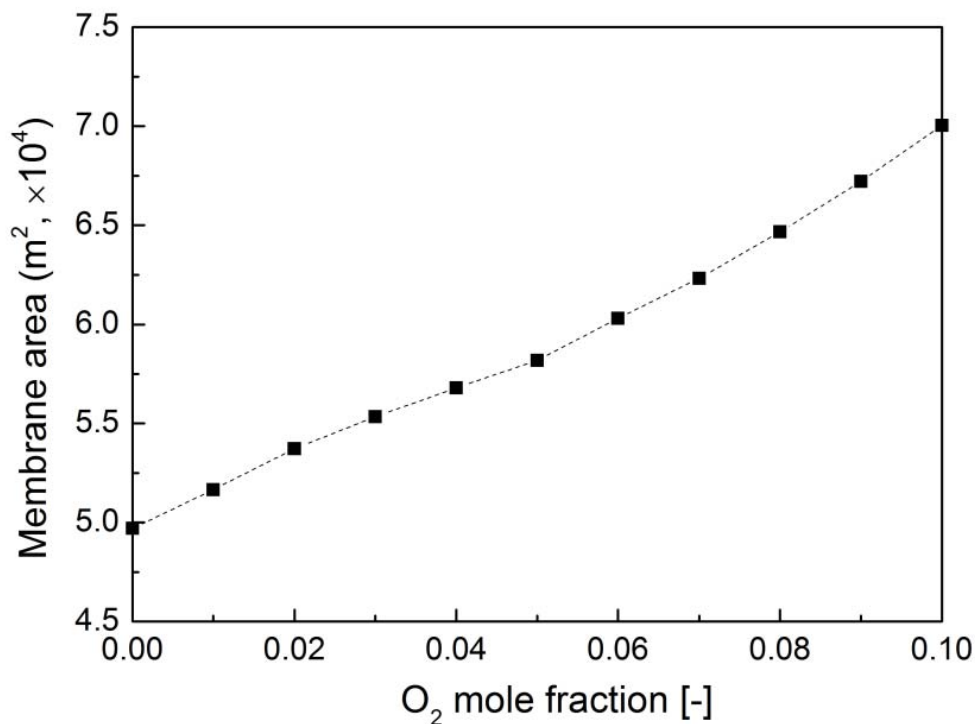
Figure 5.8. Calculated SCF membrane area for a 50 MW coal-fired power plant with different O_2 mole fractions of CO_2 in the sweep gas.

5.4 Conclusion

This study demonstrates that degradation of $SrCo_{0.8}Fe_{0.2}O_{3-\delta}$ (SCF) perovskite, oxygen-selective, membranes in a CO_2 atmosphere is affected by the oxygen partial pressure in the CO_2 sweep gas. Increasing the oxygen partial pressure enhances the CO_2 tolerance of these membranes. Long term oxygen permeation tests at 950 °C showed that mixing 5 % of oxygen to the CO_2 sweep gas can prevent the SCF membrane from degradation without sacrificing its high oxygen permeability. Based on these experimental results a modified membrane integrated oxy-fuel combustion

process is proposed. A simple membrane area calculation shows that 17 % of additional membrane area is necessary for achieving the same oxygen yield compared with pure CO_2 as sweep gas.

References

[1]   B. Metz, O. Davidson, H.d. Coninck, M. Loos, L. Meyer, IPCC Special Report on Carbon Dioxide Capture and Storage, Intergovernmental Panel on Climate Change, (2005).

[2]   M.A. Habib, H.M. Badr, S.F. Ahmed, R. Ben-Mansour, K. Mezghani, S. Imashuku, G.J. la O, Y. Shao-Horn, N.D. Mancini, A. Mitsos, P. Kirchen, A.F. Ghoneim, A review of recent developments in carbon capture utilizing oxy-fuel combustion in conventional and ion transport membrane systems, International Journal of Energy Research, 35 (2011) 741-764.

[3]   S. Engels, F. Beggel, M. Modigell, H. Stadler, Simulation of a membrane unit for oxyfuel power plants under consideration of realistic BSCF membrane properties, Journal of Membrane Science, 359 (2010) 93-101.

[4]   Y. Teraoka, H.-M. Zhang, S. Furukawa, N. Yamazoe, Oxygen permeation through perovskite-type oxides, Chemistry Letter, 14 (1985) 1743-1746.

[5]   Q. Zeng, Y.B. Zu, C.G. Fan, C.S. Chen, CO_2-tolerant oxygen separation membranes targeting CO_2 capture application, Journal of Membrane Science, 335 (2009) 140-144.

[6]   T. Klande, O. Ravkina, A. Feldhoff, Effect of A-site lanthanum doping on the CO_2 tolerance of $SrCo_{0.8}Fe_{0.2}O_{3-\delta}$ oxygen-transporting membranes, Journal of Membrane Science, 437 (2013) 122-130.

[7]   W. Chen, C.-s. Chen, L. Winnubst, Ta-doped $SrCo_{0.8}Fe_{0.2}O_{3-\delta}$ membranes: Phase stability and oxygen permeation in CO_2 atmosphere, Solid State Ionics, 196 (2011) 30-33.

[8]   G. Zhang, Z. Liu, N. Zhu, W. Jiang, X. Dong, W. Jin, A novel Nb_2O_5-doped $SrCo_{0.8}Fe_{0.2}O_{3-\delta}$ oxide with high permeability and stability for oxygen separation, Journal of Membrane Science, 405-406 (2012) 300-309.

[9]   J.W. Stevenson, T.R. Armstrong, R.D. Carneim, L.R. Pederson, W.J. Weber, Electrochemical properties of mixed conducting perovskites $La_{1-x}M_xCo_{1-y}Fe_yO_{3-\delta}$ (M = Sr, Ba, Ca), J Electrochem Soc, 143 (1996) 2722-2729.

[10]   J.X. Yi, S.J. Feng, Y.B. Zuo, W. Liu, C.S. Chen, Oxygen permeability and stability of $Sr_{0.95}Co_{0.8}Fe_{0.2}O_{3-\delta}$ in a CO_2- and H_2O-containing atmosphere, Chem Mater, 17 (2005) 5856-5861.

[11]   B. Bird, W. E.Stewart, E. N.Lightfoot, Transport Phenomena, 2ed., John Wiley&Sons, 2001.

[12]   Y.S. Lin, W.J. Wang, J.H. Han, Oxygen Permeation through thin mixed-conducting solid oxide membranes, Aiche J, 40 (1994) 786-798.

[13] P.V. Danckwerts, Continuous flow systems: Distribution of residence times, Chem Eng Sci, 2 (1953) 1-13.

[14] E. Croiset, K. Thambimuthu, A. Palmer, Coal combustion in O_2/CO_2 mixtures compared with air, The Canadian Journal of Chemical Engineering, 78 (2000) 402-407.

[15] J. Black, Cost and performance baseline for fossil energy plants. Volume 1: Bituminous coal and natural gas to electricity final report, in: National Energy Technology Laboratory, 2007, pp. 626.

[16] N. Zakowsky, S. Williamson, J.T.S. Irvine, Elaboration of CO_2 tolerance limits of $BaCe_{0.9}Y_{0.1}O_{3-\delta}$ electrolytes for fuel cells and other applications, Solid State Ionics, 176 (2005) 3019-3026.

[17] A. Brandão, J.F. Monteiro, A.V. Kovalevsky, D.P. Fagg, V.V. Kharton, J.R. Frade, Guidelines for improving resistance to CO_2 of materials for solid state electrochemical systems, Solid State Ionics, 192 (2011) 16-20.

[18] H. Vinek, H. Noller, M. Ebel, K. Schwarz, X-ray photoelectron spectroscopy and heterogeneous catalysis, with elimination reactions as an example, Journal of the Chemical Society, Faraday Transactions 1: Physical Chemistry in Condensed Phases, 73 (1977) 734-746.

[19] H. Noller, J.A. Lercher, H. Vinek, Acidic and basic sites of maim group mixed metal oxides, Materials Chemistry and Physics, 18 (1988) 577-593.

[20] H.J.M. Bosman, A.P. Pijpers, A.W.M.A. Jaspers, An X-ray photoelectron spectroscopy study of the acidity of SiO_2-ZrO_2 mixed oxides, J Catal, 161 (1996) 551-559.

[21] C.M. Pradier, C. Hinnen, K. Jansson, L. Dahl, M. Nygren, A. Flodstrom, Structural and surface characterization of perovskite-type oxides; influence of A and B substitutions upon oxygen binding energy, Journal of Materials Science, 33 (1998) 3187-3191.

[22] N.A. Merino, B.P. Barbero, P. Eloy, L.E. Cadús, $La_{1-x}Ca_xCoO_3$ perovskite-type oxides: Identification of the surface oxygen species by XPS, Applied Surface Science, 253 (2006) 1489-1493.

[23] J. Sunarso, S. Baumann, J.M. Serra, W.A. Meulenberg, S. Liu, Y.S. Lin, J.C.D. da Costa, Mixed ionic-electronic conducting (MIEC) ceramic-based membranes for oxygen separation, Journal of Membrane Science, 320 (2008) 13-41.

[24] H.J.M. Bouwmeester, H. Kruidhof, A.J. Burggraaf, Importance of the surface exchange kinetics as rate limiting step in oxygen permeation through mixed-conducting oxides, Solid State Ionics, 72 (1994) 185-194.

[25] E.L.Cussler, Diffusion: mass transfer in fluid system, 1ed., Cambridge University Press, Cambridge,1984.

Chapter 6 Membrane-integrated oxy-fuel combustion: process design and simulation

Abstract:

In this chapter a membrane-integrated oxy-fuel combustion process is designed and simulated in UniSim®. The results show that a net efficiency of 32.1 % is obtained for a coal-fired power plant where 20 tonne/h of coal is burned for electric power generation, which is higher than that of an oxy-fuel combustion process using oxygen from cryogenic distillation of air (29.6 %). The specific electrical energy demand for CO_2 capture in this oxy-fuel process, including oxygen production and CO_2 compression (to 100 bar), is calculated to be ~159 kWh_e / t_{CO_2}. The required membrane area for the power plant is approximately 71,000 m^2 based on Ta-doped $SrCo_{0.8}Fe_{0.2}O_{3-\delta}$ (SCF) membranes. Inspired by the research as described in chapter 4, a modified process is proposed, in which un-doped SCF membranes are used for air separation and an extra O_2/CO_2 loop is introduced to protect the SCF membranes. The modified process shows a similar net efficiency of 31.9 %, but a considerably lower amount of membrane area (49,000 m^2) is necessary.

This chapter has been submitted for a journal publication.

List of symbols

A	Surface area of an heat exchanger (m^2)
A_m	Total needed membrane area (m^2)
d	Membrane thickness (cm)
D_i	Membrane inner diameter (cm)
D_o	Membrane outer diameter (cm)
E_{out}	electric power output (MW)
E_t	thermal power released from the coal combustion (MW)
E_{O_2}	Power for oxygen production (MW)
$E_{CO_2}^{COM}$	Power for CO_2 compression to 100 bar (MW)
f_f^i	Oxygen mole fraction of the feed gas at inlet
f_f^o	Oxygen mole fraction of the feed gas at outlet
f_s^i	Oxygen mole fraction of the sweep gas at inlet
f_s^o	Oxygen mole fraction of the sweep gas at outlet
F_f^i	Feed gas flow rate in a single membrane tube at inlet (mole/h)
F_f^o	Feed gas flow rate in a single membrane tube at outlet (mole/h)
F_s^i	Sweep gas flow rate in a single membrane tube at inlet (mole/h)
F_s^o	Sweep gas flow rate in a single membrane tube at outlet (mole/h)
$F_f^i(T)$	Total feed gas flow rate of the membrane module at inlet (mole/h)
$F_f^o(T)$	Total feed gas flow rate of the membrane module at outlet (mole/h)
$F_s^i(T)$	Total sweep gas flow rate of the membrane module at inlet (mole/h)
$F_s^o(T)$	Total sweep gas flow rate of the membrane module at outlet (mole/h)
F_{O_2}	Oxygen produced by a single membrane tube (mole/h)
$F_{O_2}^T$	Oxygen produced by the whole membrane module (mole/h)
j_{O_2}	Oxygen flux (mole/cm^2/s)
L	Length of the membrane tube (cm)
$\dot{m}_{O_2}$	Oxygen mass flow rate (tonne/h)

$\dot{m}_{CO_2}$	CO_2 capturing mass flow rate (tonne/h)
F_{CO_2}	CO_2 molar flow rate (mole/h)
N_m	Total needed membrane tube number
P_f	Operating pressure of the feed gas (bar)
P_s	Operating pressure of the sweep gas (bar)
P_{O_2}	Oxygen partial pressure (bar)
P''_{O_2}	Oxygen partial pressure at feed side (bar)
P'_{O_2}	Oxygen partial pressure at sweep side (bar)
Q	Heat transferred per unit time in a heat exchanger (MW)
R	Gas constant (J/mole/K)
SE_{CO_2}	Specific energy for CO_2 capture (kWh_e / t_{CO_2})
SE_{O_2}	Specific energy for O_2 production (kWh_e / t_{O_2})
T	Temperature (K)
ΔT_{lm}	Logarithm mean temperature difference between the two fluids (K
U	Overall heat transfer coefficient of the heat exchanger (W/m^2/C)
$\eta_{t \to e}$	Overall steam turbine efficiency
η	Power plant net efficiency
η_r	Power plant net efficiency of the reference case
η_o	Power plant net efficiency of the oxy-fuel combustion process
θ	Oxygen recovery

6.1 Introduction

Coal-fired power plants contribute to around 30 % of the total anthropogenic CO_2 emission to the atmosphere, which is considered to be one of the main reasons of the global climate change. In the past 20 years several techniques are developed to reduce the CO_2 emission and several overviews of these techniques were published [1-3]. Among these techniques post-combustion, combined with amine absorption, is the most mature one. In this technique CO_2 in the flue gas from the power plant is chemically absorbed at ambient temperature by an amine and the CO_2-enriched amine then flows through a stripper where temperature is increased to 110 ºC - 130 ºC to remove the absorbed CO_2 [4]. After CO_2 removal, the amine solvent is pumped back to the absorber via an amine lean-rich heat exchanger and a cooler to bring it down to the absorber temperature level. In this technique, large amounts of energy has to be applied for the desorption of CO_2 in the stripper because part of the water in the amine solvent (around 70 wt %) is also evaporated. The overall energy consumption for CO_2 capture in this amine absorption process is approximately 340-450 kWh_e/t_{CO_2}, which results in a net efficiency drop of 30-35 % for the whole post-combustion process [5-7].

Another promising technique for CO_2 capture is oxy-fuel combustion where pure oxygen, instead of air, is used for the combustion of coal, resulting in a concentrated CO_2 gas stream thus enabling efficient CO_2 capture, because no amine absorption/desorption process is required [8]. Pure oxygen, required for the oxy-fuel combustion process, can be produced via cryogenic distillation of air, which is a mature technique for oxygen separation from air, as established around 100 years ago. However, the energy consumption for oxygen production, using this technique, is relatively high. For a standalone cryogenic air separation unit the specific energy for oxygen production is about 200-240 kWh_e/t_{O_2} [9] (oxygen under standard conditions), which leads to a net efficiency drop in the power plant of ~10 %. This

efficiency drop is much smaller than that in the amine based post-combustion process. In addition, the energy, necessary for oxygen production by cryogenic distillation, can be further decreased by optimizing this process, but $160 \ \text{kWh}_e/\text{t}_{O_2}$ seems to be a realistic limit [9]. To overcome this limit, it is proposed to produce the oxygen, required needed for the oxy-fuel combustion process, by using oxygen transport membranes (OTM), which are conductive only to oxygen at elevated temperatures (>700 °C) [5, 10-12]. A general scheme of this process is shown in Figure 6.1. The oxygen, as separated from air by the membrane, is swept by the CO_2, while the O_2/CO_2 gas mixture is used for the combustion of the fossil fuels. After purification, the exhaust gas mainly consists of CO_2, part of the CO_2 is recycled as sweep gas, and the other part is compressed for delivery and storage.
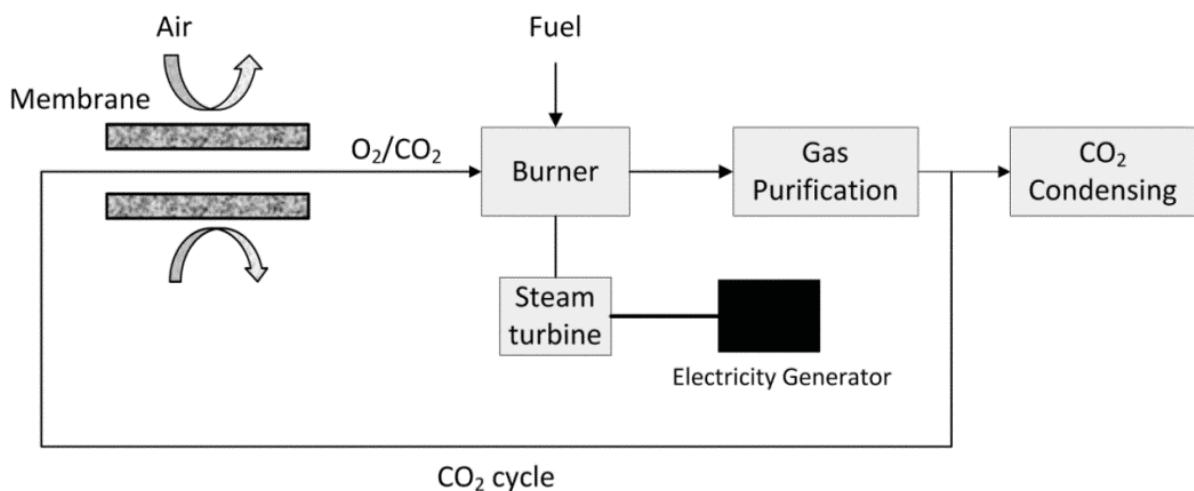
Figure 6.1. A simple illustration of the membrane-integrated oxy-fuel combustion process.

A lot of research is performed in the field of exploring suitable membranes for air separation for this application [11, 13-18]. However, little work has been done on the overall evaluation of a membrane-integrated oxy-fuel combustion process, such as membrane area and energy balance estimation or to show whether the currently developed membranes are sufficient for, or far from, industrial application [19].

In this study, a membrane-integrated oxy-fuel combustion process is designed for a coal-fired power plant, where 20 tonne/h of coal is burned for electric power.

This process is simulated in UniSim®, and the membrane area, necessary for air separation for the power plant, the net efficiency of the power plant and the energy demand for CO_2 capture are calculated. For comparison, two other combustion processes are presented: a conventional coal-fired power plant, using air, without CO_2 capture and an oxy-fuel combustion process using oxygen from cryogenic distillation of air. The differences among these processes are discussed.

6.2 Coal-fired power plant without CO₂ capture

In a conventional coal-fired power plant, air is used to combust the coal and the CO_2-containing exhaust gas is emitted to the atmosphere. A simple scheme of this process is shown in Figure 6.2. Here air is compressed to 1.7 bar (A1) to carry the pulverized coal to the burner, where combustion occurs. It is assumed that there is only carbon in the coal and the reaction between carbon and oxygen is stoichiometric,

$$C + O_2 \rightarrow CO_2 \quad \Delta H_r^\circ = -393.5 \, \text{kJ/mol} \tag{6.1}$$

The thermal energy, released from the burner, is used by a steam turbine for electricity generation. It should be noted that the steam turbine system was not drawn in this process because its efficiency varies a lot in different power plants. In this work, we use a parameter called overall steam turbine efficiency ($\eta_{t \rightarrow e}$) to represent the conversion ratio from thermal power to electric power.
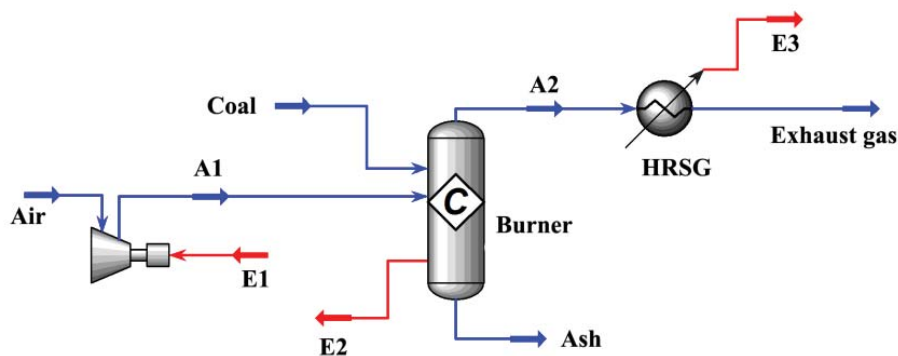
Figure 6.2. Scheme for a conventional coal-fired power plant without CO_2 capture (details about the material and power streams are given in table A6.1. in the appendix).

The temperature of the flue gas (A2) from the burner at $\sim$ 400 ºC is further decreased to 50 ºC by a Heat-Recovery-Steam-Generator (HRSG), which energy (E3) is also used for the steam turbine system. After the HRSG the exhaust gas consists of some impurity (acid) gases like SO_2 and NO_x, which have to be removed in a purification step before emission to the atmosphere is allowed. However, as is mentioned above, it is assumed that there is only carbon in the coal and thus a purification step is omitted. The same strategy holds for all studies in this work.

The electric power output (E_{out}) and net efficiency (η_r) of the process were calculated by means of the following equations:

$$E_{out} = (E_2 + E_3) \times \eta_{t \to e} - E_1 \tag{6.2}$$

$$\eta_r = \frac{E_{out}}{E_t} \times 100 \,\% \tag{6.3}$$

where E_1, E_2 and E_3 are indicated in Figure 6.2 and E_t, the total thermal energy released from the combustion, is calculated by the following equation:

$$E_t = \Delta H_r^o \times F_{CO_2} \tag{6.4}$$

where ΔH_r^o is the standard enthalpy change in the reaction shown in eq. (6.1), and F_{CO_2} the CO_2 molar flow rate.

As can be seen from eq. (6.2) and (6.3), $\eta_{t \to e}$ plays an important role in determining the electric power output and the power plant net efficiency. In principle, $\eta_{t \to e}$ has a theoretical maximum Carnot efficiency of $\sim$64 % assuming the water/steam cycle works between room temperature (25 ºC) and 565 ºC (creep temperature of stainless steel), but an actual efficiency of up to 42 % for a modern coal-fired power plant is usually expected. In this study $\eta_{t \to e}$ is assumed to be 40 % for all cases [3].

Table 6.1. Operating conditions and simulation results for a conventional coal-fired power plant without CO_2 capture.

Variable	Value	Units
Coal consumption	20.0	tonne/h
Air mass flow	230	tonne/h
Air pressure after compression[2]	1.70	bar
Compressor adiabatic efficiency	90.0**	%
Overall steam turbine efficiency ($\eta_{t \to e}$)	40.0	%
Electric power output (E_{out})	70.2	MW
Net efficiency (η_r)	38.5	%

**: Compressor adiabatic efficiency is kept at 90 % for all studies in this work

The process, shown in Figure 6.2, was simulated in UniSim® design, which inherently ensures mass and energy balances across all components, includes thermodynamic data for all chemical species, calculates chemical equilibrium states for the combustion reaction. The simulation results are summarized in table 6.1 (details about the material and power streams are given in table A6.1 in the appendix). The net efficiency of the power plant (η_r) is calculated to be 38.5 % according to eq. (6.2), which is in agreement with the case as treated by J. Black of the National Energy Technology Laboratory [3].

The process shown in Figure 6.2 is used as a reference case for comparison with processes where CO_2 capture is applied. The net efficiency of the power plant is expected to be lower when CO_2 capture is applied because some power has to be spent on CO_2 processing. If one assumes that the net efficiency in this new process is η and that the CO_2 mass flow rate is $\dot{m}_{CO_2}$ (assume 100 % CO_2 capture), then the energy, necessary to capture one unit of CO_2, can be calculated by the following equation,

$$SE_{CO_2} = \frac{E_t(\eta_r - \eta)}{\dot{m}_{CO_2}} \qquad (6.5)$$

SE_{CO_2} is the specific energy demand for CO_2 capture whose unit can be given as kWh_e/t_{CO_2} .

6.3 Oxy-fuel combustion process

In an oxy-fuel combustion process, as depicted in Figure 6.3, oxygen is used instead of air to combust the fuel. A CO_2 recycle (A6, A7) is introduced to avoid extreme high temperatures in the burner [20]. The O_2/CO_2 ratio is adjusted to be 0.35/0.65 (v/v) as it is reported that the combustion of coal with this O_2/CO_2 ratio has a similar flame temperature and heat capacity as the combustion of coal in air [21]. This O_2/CO_2 mixture (A1) is compressed to 1.7 bar to carry the pulverized coal to the burner for combustion, and the energy, released from combustion, is used for the steam turbine system for electricity generation. The flue gas from the burner (A3) flows through a HRSG for further steam generation and after that it is divided into two parts, one part (A6, identical to A7) is recycled and the other part (A5) is compressed for delivery and storage. The CO_2 compression (to 100 bar) is carried out in 5 stages and after each stage the gas is cooled to 30 °C before the next compression step.
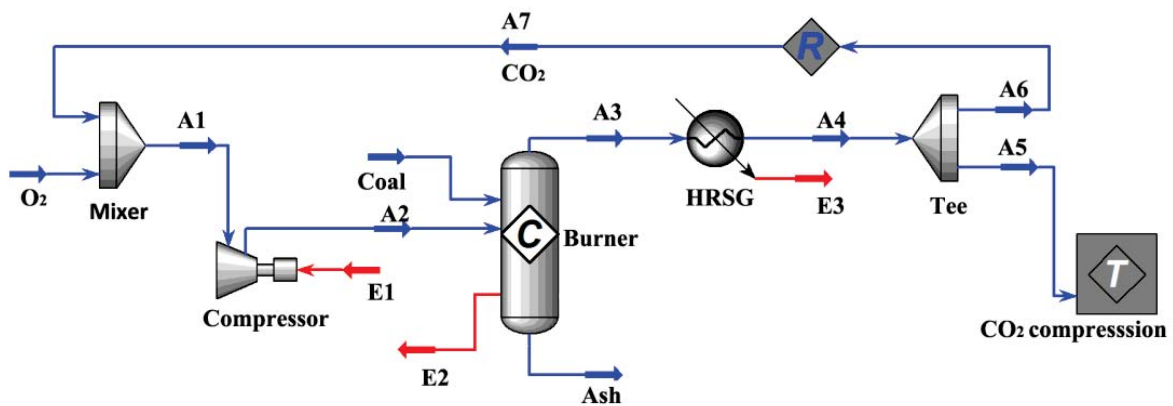
Figure 6.3. Oxy-fuel combustion process with CO_2 capture in a coal-fired power plant (details about the material and power streams are given in table A6.2. in the appendix).

The oxygen, necessary for this process, is produced via cryogenic distillation of air and the energy demand (electric power) for this oxygen production is assumed to be $200 \text{ kWh}_e / t_{O_2}$ [9]. Taking that into consideration, the electric power output and net efficiency of this process can be calculated with the following equations,

$$E_{out} = (E_2 + E_3) \times \eta_{t \rightarrow e} - (E_1 + E_{O_2} + E_{CO_2}^{COM}) \qquad (6.6)$$

$$\eta_o = \frac{E_{out}}{E_t} \times 100\% \qquad (6.7)$$

where E_{O_2} and $E_{CO_2}^{COM}$ represent the power needed for the oxygen production and the CO_2 compression (to 100 bar).

The process shown in Figure 6.3 was simulated in UniSim® design and the results are given in table 6.2 (details about the material and power streams are given in table A6.2 in the appendix). The net efficiency is calculated to be 29.6 %, which is lower than that of the reference process without CO_2 capture (38.5 %). This is due to the large amount of power, necessary for oxygen production (10.7 MW) and CO_2 compression (6.11 MW). According to eq. (6.5), the specific energy demand for CO_2 capture is calculated to be $221 \text{ kWh}_e/t_{CO_2}$.

Table 6.2. Simulation results of the conventional oxy-fuel combustion process with CO_2 capture

Variable	Value	Units
Coal consumption	20.0	tonne/h
O_2 mass flow	53.3	tonne/h
Power for oxygen production (E_{O_2})	10.7	MW
CO_2 mass flow (captured part, A5)	73.4	tonne/h
Power for CO_2 compression ($E_{CO_2}^{COM}$)	6.11	MW
CO_2 mass flow (recycled part, A6)	138	tonne/h
Power for O_2/CO_2 compression (E1)	2.17	MW
Electric power output (E_{out})	54.0	MW
Net efficiency (η_o)	29.6	%

6.4 Membrane-integrated oxy-fuel combustion process

6.4.1 Membrane module

Membrane material selection

The membrane, to be used in the membrane-integrated oxy-fuel combustion (see Figure 6.1) process, should be stable in a CO_2 atmosphere, combined with sufficient oxygen permeability. However, for most highly permeable membranes such as $Ba_{0.5}Sr_{0.5}Co_{0.8}Fe_{0.2}O_{3-\delta}$ (BSCF) and $SrCo_{0.8}Fe_{0.2}O_{3-\delta}$ (SCF) membranes [22, 23], the stability of these membranes in CO_2 atmosphere is a big issue. For example, the oxygen flux of SCF membranes decreases to almost zero after exposing the permeate

side to a pure CO_2 sweep gas stream for 70 hours at 950 ºC [10]. Alternatively, there are some membranes which are very stable in CO_2 atmosphere, such as dual phase membranes or K_2NiF_4-type membranes [15, 17, 24, 25]. The oxygen fluxes of these membranes, however, are much lower, as compared with BSCF and SCF. In [11] it is found that SCF remains stable in a CO_2 atmosphere when Co/Fe (i.e. B) is partly (10 %) substituted by tantalum (called as Ta-doped SCF), while the oxygen flux is not decreased a lot. For reasons of CO_2 stability and sufficient oxygen flux, Ta-doped SCF is selected as membrane material for this study.

The oxygen flux of a dense membrane is calculated by using the Wagner equation:

$$j_{O_2} = -\frac{RT}{(4F)^2 d} \sigma_{ion} \ln \frac{P''_{O_2}}{P'_{O_2}} \tag{6.8}$$

where j_{O_2} is the oxygen flux, R gas constant, T absolute temperature, F Faraday constant, d membrane thickness, σ_{ion} oxygen ionic conductivity and P_{O_2} oxygen partial pressure (P''_{O_2} at feed side and P'_{O_2} at sweep side). The oxygen ionic conductivity not only depends on the temperature but also on the P_{O_2}. In this study, the membrane module works at a fixed temperature (950 ºC) but in a changing P_{O_2} environment. In general, the oxygen ionic conductivity increases with increasing P_{O_2}, but the change in conductivity as function of P_{O_2} is quite small unless P_{O_2} is less than 0.01 bar [26]. In this study the P_{O_2} in the membrane module is higher than 0.01 bar except at the very beginning of the sweep site of the (tubular) membrane module and therefore it is assumed that the oxygen ionic conductivity is constant in our case. Based on previous oxygen permeation studies at 950 ºC under and 0.21/0.04 bar P_{O_2} gradient [10], the oxygen ionic conductivity of SCF is calculated to be ~1 S/cm. For Ta-doped SCF, the oxygen flux is around 30 % lower at the same

temperature and P_{O_2} gradient. Therefore it is assumed that the oxygen ionic conductivity is 0.7 S/cm for this system.

Membrane area calculation

Different types of membrane designs are available, like flat, tubular, hollow fiber or monolithic configurations. All designs have advantages and disadvantages in terms of area, sealing and fabrication. A review paper by Vente et al. compared these configurations and it was concluded that a tubular design is the optimal one [27]. In this work a tubular membrane module is chosen for oxygen separation from air. A schematic drawing of the membrane module is shown in chapter 4 (Figure 4.3). In this study the membrane tubes are installed in parallel. Geometrical and operating parameters for one membrane tube are given in table 6.3.

Table 6.3. Geometry of one tubular membrane and operating conditions.

Variable	Value	Units
Membrane length (L)	100	cm
Membrane outer diameter (D_o)	1.0	cm
Membrane inner diameter (D_i)	0.8	cm
Membrane thickness (d)	0.1	cm
Pressure of feed gas (P_f)	10	bar
Pressure of sweep gas (P_s)	1.7	bar
Operating temperature	950	°C
O_2 mole fraction of feed gas at inlet (f_f^i)	0.21	-
O_2 mole fraction of feed gas at outlet (f_f^o)	0.02	-
O_2 mole fraction of sweep gas at inlet (f_s^i)	0.005	-
O_2 mole fraction of sweep gas at outlet (f_s^o)	0.35	-

In order to calculate the required amount of membrane area, it is necessary to know how much oxygen is produced by one single membrane tube and then the total needed membrane area can be extrapolated. As is schematically shown in Figure 6.4, it is assumed that the membrane operates in a countercurrent mode, where F_s^i, F_f^i are the sweep and feed gas flow rates at the inlet of the membrane tube, and F_s^o, F_f^o at the outlet, while f_s^i, f_f^i, f_s^o and f_f^o the corresponding oxygen mole fractions in these gas streams.
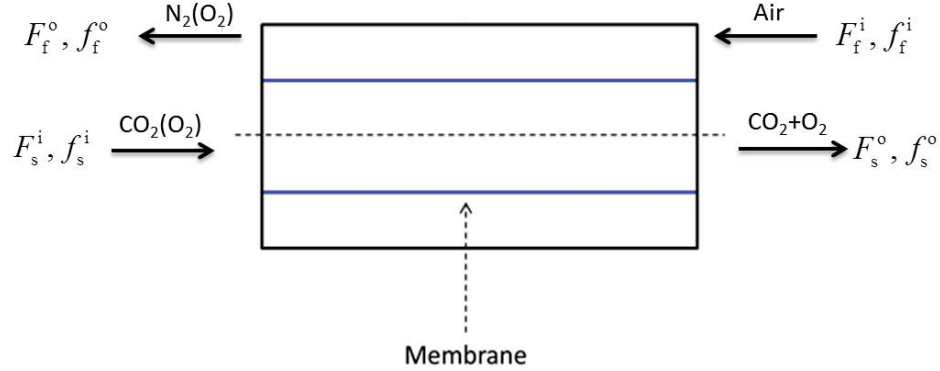
Figure 6.4. Scheme of oxygen flux through a membrane tube, F represents gas flow rate and f is the corresponding oxygen mole fraction in the gas stream.

In this study, f_f^i and f_s^o are fixed at 0.21 (oxygen mole fraction of air) and 0.35 (as explained in section 6.3), and the default values of f_s^i and f_f^o are 0.005 (residual oxygen in CO_2) and 0.02 (see table 6.3). With these values, a linear relationship between F_s^i and F_f^i is derived according to the conservation of mass for oxygen.

$$F_s^i = \frac{(f_f^i - f_f^o) \times (1 - f_s^o)}{(f_s^o - f_s^i) \times (1 - f_f^o)} F_f^i \qquad (6.9)$$

Note that eq. (6.9) is necessary rather than sufficient to meet the requirements of oxygen mole fractions. When F_s^i and F_f^i increase simultaneously, by solving the above mentioned problem according to the procedure as described in chapter 4 (section 4.2.5), it is found that both f_s^o and f_f^o decreases, and there is only one combination of (F_s^i, F_f^i) that meet the constrains of oxygen mole fractions (f_s^i, f_f^i, f_s^o and f_f^o) with given membrane property and operating conditions, i.e., temperature and pressure. With this (F_s^i, F_f^i) combination, F_s^o and F_f^o can be calculated. In other words, if f_s^i, f_f^i, f_s^o and f_f^o are specified, F_s^i, F_f^i, F_s^o and F_f^o are also fixed, and the oxygen produced by a single membrane tube can be

calculated by:

$$F_{O_2} = F_s^o - F_s^i \qquad (6.10)$$

Since the total amount of oxygen, necessary for the process, is known, the number of membrane tubes, N_m, can be calculated, as well as the total membrane area (A_m),

$$N_m = \frac{F_{O_2}^T}{F_{O_2}} \qquad (6.11)$$

$$A_m = \frac{\pi}{2}(D_i + D_o)LN_m \qquad (6.12)$$

where $F_{O_2}^T$ is the amount of total required oxygen, F_{O_2} the amount of oxygen produced by a single membrane tube, D_i and D_o the membrane inner and outer diameter, and L the membrane length.

6.4.2 Process design

The design for a membrane-integrated oxy-fuel combustion process is shown in Figure 6.5. In this design air is compressed to 10 bar, preheated by a heat exchanger (HEX-1) and further heated (by Heater-1) to the desired temperature (950 ºC) before flowing to the membrane module. In the membrane module oxygen is depleted and the © gas (A4) is used to preheat the feed gas. After the heat exchanger the © gas (A5) is used to operate a gas turbine, where the energy released from gas expansion (E2) is transferred to the air compressors. At the sweep side of the membrane the permeated oxygen is swept by CO_2 (A14), and this O_2/CO_2 mixture (A7), after passing a heat exchanger (HEX-2) to preheat the recycled CO_2 sweep gas (A12), is used for the combustion of coal in the burner. The energy (E4) released from the burner is partly used to heat the air stream (E3) and the recycled CO_2 stream (E6), and the remaining part is transferred to a water-steam recycle system for electricity generation. The flue gas (A9) from the burner flows through a HRSG where the energy (E7) is further used for steam generation. After the HRSG the flue gas (A10)

goes to a gas splitter (TEE), in which one part of it (A11) is recycled as sweep gas for the membrane module and the other part (A15) is compressed (to 100 bar) for delivery and storage.
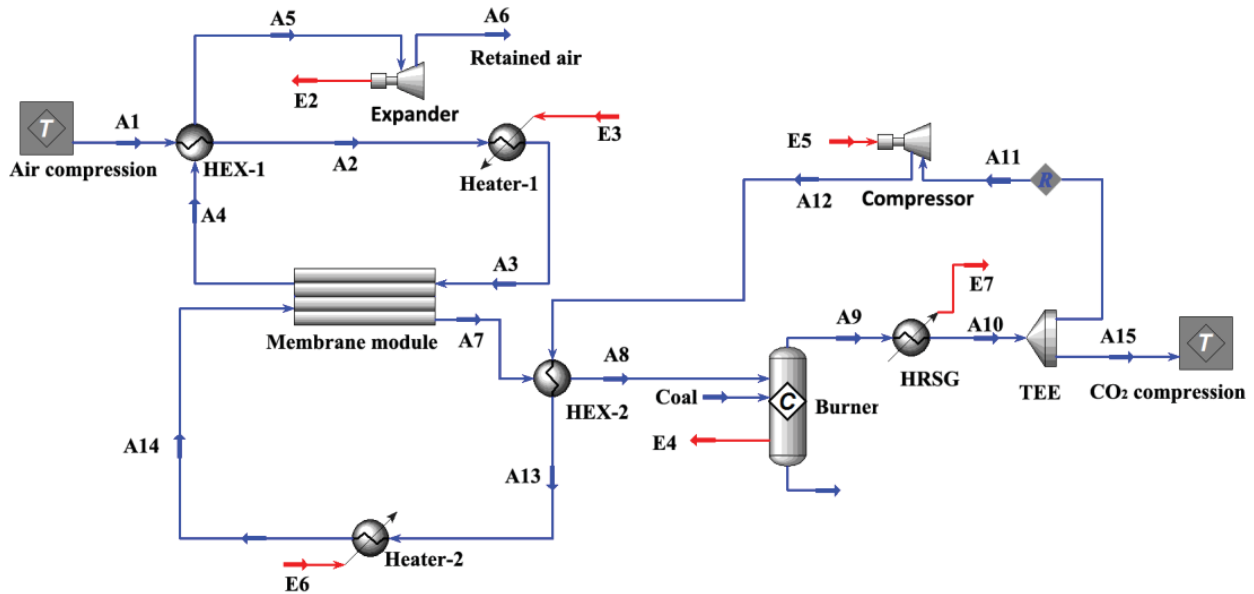
Figure 6.5. Flow sheet of membrane-integrated oxy-fuel combustion process (details about the material and power streams are given in table A6.3. in the appendix).

In this design the gas compressors (all compressors) play an important role in the efficiency of the power plant. A key parameter for gas compressors is the maximum discharge temperature, which strongly depends on the materials and sealants used for the compressor. As a general rule the discharge temperature should be lower than 200 ºC for most gas compressors [28]. Multistage compression with intermediate cooling is therefore usually applied in order to reach the desired pressure. In this study a three-stage air and a five-stage CO_2 compressor is used and the discharge temperature is kept below 150 ºC, while the compressed gas is cooled down to 30 ºC between the compressing stages.

The design includes two heat exchangers, a heat exchanger between compressed air and © air from the membrane module (HEX-1) and a heat exchanger between the recycled CO_2 and the O_2/CO_2 mixture from the membrane module (HEX-2). The general equation for heat transfer across a surface A in a heat exchanger is [29]:

$$Q = UA\Delta T_{lm} \tag{6.13}$$

where Q is the heat transfer per unit time, U the overall heat transfer coefficient and ΔT_{lm} the logarithm mean temperature difference between the two fluids. In general, a heat exchanger shows a higher efficiency at smaller values of ΔT_{lm}. However, a smaller ΔT_{lm} leads to a smaller driving force for heat transfer and therefore a larger area of the heat exchanger is necessary. As a general rule, ΔT_{lm} should be more than 20 ºC, and the temperature approach (the temperature difference between outlet temperature of hot fluid and inlet temperature of cold fluid) should be more than 10 ºC to avoid an extremely large heat exchanger [29]. In this study, ΔT_{lm} in both heat exchangers is kept at ~ 150 ºC and the temperature approach is kept at ~ 100 ºC. These high values in ΔT_{lm} and temperature approach are designed due to the low gas-gas heat transfer coefficient.

6.4.3 Process simulation

The process simulation was performed in UniSim®. The main assumptions such as coal consumption rate, compressor/expander efficiency and steam turbine efficiency are kept the same with the previous studies in this chapter (see table 6.1). Since there is no membrane unit in UniSim®, the flow rates and compositions of A3, A4, A7 and A14 (see Figure 6.5) were calculated with a dedicated membrane module solved by Matlab. The values were then transferred to UniSim® simulation. The power output and the net efficiency of the power plant were calculated as below:

$$E_{out} = (E_4 - E_6 - E_3 + E_7) \times \eta_{t \to e} - (E_{com} - E_2) \tag{6.14}$$

$$\eta_m = \frac{E_{out}}{E_t} \times 100\% \tag{6.15}$$

where E_{com} is the electric power necessary for all gas compressors (power for air compression + power for CO_2 compression to 100 bar for stream A15 + $E5$).

The simulation results are given in table 6.4. Details on material and power

streams are given in table A6.3 of the appendix. A net efficiency of 32.1 % is obtained, which is lower than the reference process, without CO_2 capture (38.5 %), but higher than the conventional oxy-fuel combustion process (29.6 %).

Table 6.4. Simulation results for the membrane based oxy-fuel combustion process.

Variable	Value	Units
Air mass flow	250	tonne/h
Power for air compression	17.2	MW
Power from retentive air expansion (E2)	12.0	MW
CO_2 mass flow (captured part)	73.4	tonne/h
Power for CO_2 compression (to 100 bar)	6.11	MW
CO_2 mass flow (recycled part)	138	tonne/h
Power for recycled CO_2 compression (E5)	1.75	MW
Total membrane area (A_m)	71,000	m^2
Electric power output (E_{out})	58.5	MW
Net efficiency (η_m)	32.1%	-

6.4.4 Specific energy demand for CO_2 capture and oxygen production

According to eq. (6.5), the specific energy demand for CO_2 capture (so for CO_2 compression and oxygen production) is calculated to be ~159 kWh_e/t_{CO_2}, which is lower than that in the oxy-fuel combustion process where oxygen is supplied by cryogenic distillation of air (221 kWh_e/t_{CO_2} see section 6.3). In the oxy-fuel combustion process, described in section 6.3, the specific energy demand for oxygen production can easily be determined, as it is a stand-alone process. For the membrane-integrated oxy-fuel combustion process, the oxygen production (by

membrane separation) is coupled with other processes in the power plant. It is therefore difficult to distinguish the power, necessary for oxygen production from other power demanding processes in this design. In order to calculate this and make a comparison with the cryogenic distillation of air process, the following assumption is made:

The total reduction of power plant capacity due to CO_2 capture consists of the powers, necessary for CO_2 compression and oxygen production.

$$SE_{O_2} = \frac{E_t(\eta_r - \eta) - E_{CO_2}^{COM}}{\dot{m}_{O_2}}$$

(6.16)

Since the power for CO_2 compression is known (table 6.4), the power needed for oxygen production is subsequently obtained. The specific energy for oxygen production (104 kWh_e/t_{O_2}), calculated according to eq. (6.16), is significantly lower than that of cryogenic distillation process (200 kWh_e/t_{O_2}) [9].

6.4.5 Parametric study

In this section, the effect of oxygen recovery, operating pressure at membrane feed side and membrane thickness on the performance of the power plant are discussed. When one process parameter is varied, the other parameters are kept constant, having the values as used for the 'standard case' (see table 6.1 and 6.3).

Effect of oxygen recovery

In this design oxygen recovery (θ) is defined as the ratio of oxygen, permeated through the membrane, and total oxygen in the feed gas. This recovery is a function of the oxygen mole fractions of the feed gas at the in- and outlet of the membrane module.

$$\theta = \frac{F_f^i f_f^i - F_f^o f_f^o}{F_f^i f_f^i} = \frac{f_f^i - f_f^o}{f_f^i(1 - f_f^o)}$$

(6.17)

As air is used as the feed gas, f_f^i is 0.21, then eq. (6.17) can be rewritten,

$$\theta = \frac{0.21 - f_f^o}{0.21 \times (1 - f_f^o)} \qquad (6.18)$$

For the standard case of the membrane-integrated oxy-fuel combustion process, as described in section 6.4.3, the oxygen recovery has a value of 0.92. It is obvious that θ decreases with f_f^o in the range of 0 to 0.21, meaning that a lower f_f^o results in a higher θ. Since the total amount of oxygen, necessary for the power plant is a constant, a lower feed flow rate is needed at lower f_f^o. Consequently, in that case the energy for compression and heating the feed gas will decrease, which possibly affects the net efficiency of the power plant. In Figure 6.6 the effect of oxygen recovery on several process parameters and power plant efficiency are given. Figure 6.6a shows the effect of oxygen recovery (or oxygen mole fraction at the feed gas outlet: f_f^o) on the amount of oxygen produced by a single membrane tube. It is clear that when f_f^o decreases, the mean P_{O_2} at the air side also decreases, implying that the driving force for oxygen permeation is smaller, thus the oxygen produced by one single membrane tube decreases. Figure 6.6b indicates that by decreasing f_f^o from 0.10 to 0.01, the required feed gas flow rate (F_f^i) decreases from 13.8 to 8.3 ($\times 10^6$ mole/h). This also means that the total membrane area, required for the production of a fixed amount of oxygen, increases from 61,000 m² to 73,000 m² (Figure 6c), meaning an increase of 20 % in required membrane area. However the net efficiency of the power plant increases from 30.4 % to 32.2 % with decreasing f_f^o.
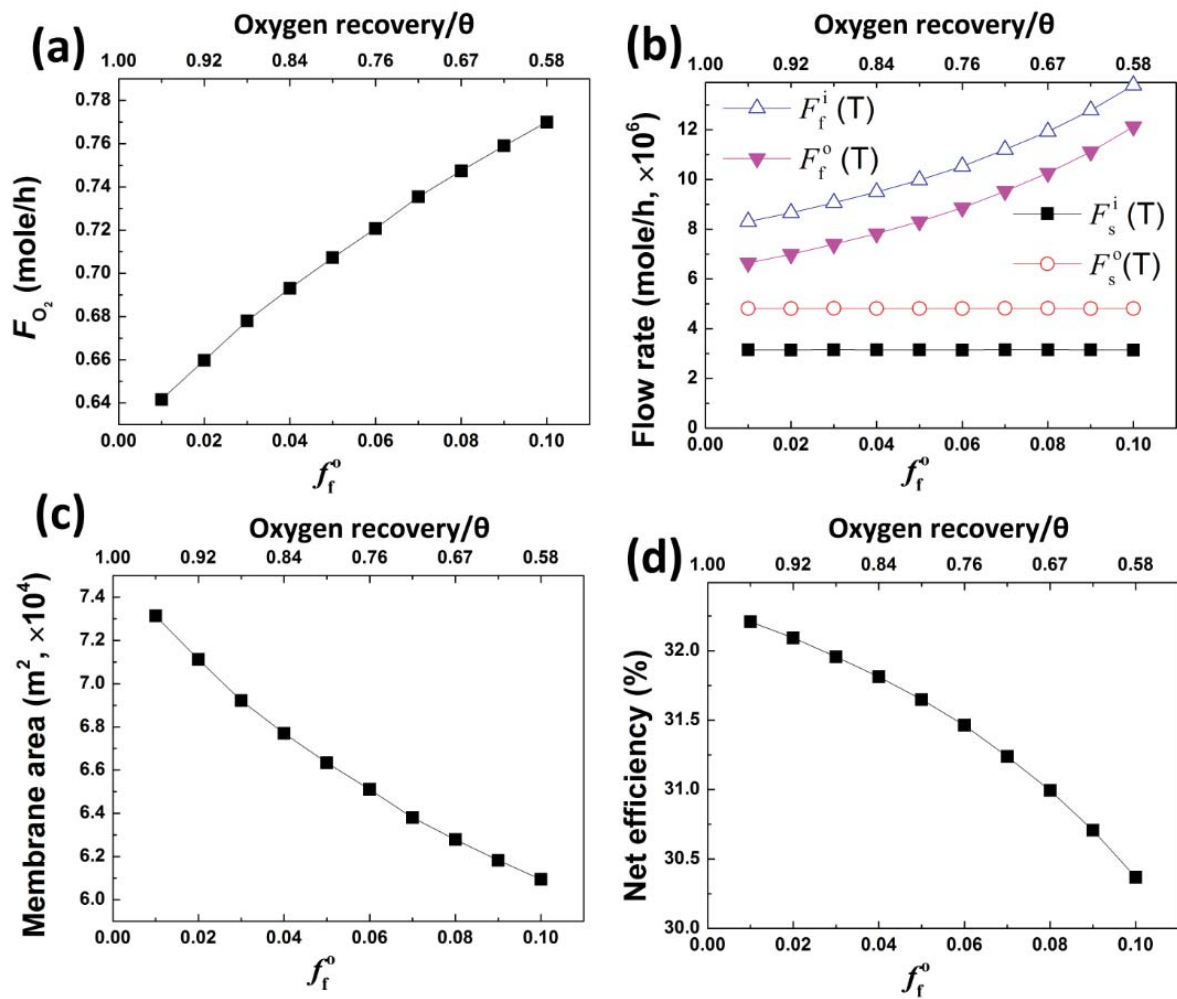
Figure 6.6. Effect of oxygen recovery on several process parameters (a) Oxygen produced by one membrane tube; (b) Gas flow rate in the whole membrane module; (c) Total membrane area needed and (d) Net efficiency of the power plant. (f_f^i remains constant in this parametric study).

Effect of membrane feed side operating pressure

Varying the operating pressure at the feed side of the membrane (P_f) has two major impacts on the characteristics of the power plant: (1) the total required membrane area and (2) the net efficiency of the power plant (see Figure 6.7). Figure 6.7a shows that a decrease in P_f from 13 bar to 4 bar results in a reduction in oxygen production by one single membrane tube from 0.79 to 0.24 mole/h. This can be explained by the fact that by decreasing in P_f the driving force for oxygen transport

through the membrane decreases and thus the amount of oxygen produced by one single membrane tube is reduced. This reduced oxygen production per membrane tube leads to an increase of the required amount of membranes from 59,000 m² to 195,000 m² (Figure 6.7b), meaning an increase by more than a factor of 3. Finally, a decrease in P_f leads to a decrease in power, necessary for air compression, which causes an increase of the net efficiency of the power plant. It can be seen from Figure 6.7c, when P_f decreases from 13 bar to 4 bar, the power plant net efficiency increases from 31.6 % to 33.6 %.

The change in the amount of required membrane area as function of oxygen mole fraction at the outlet of the feed gas (f_f^o) and as function of operating pressure at the feed side of the membrane (P_f) will now be discussed. It is found that the influence of P_f is more pronounced than that of f_f^o (compare resp. Figure 6.7b and 6.6c). This can be explained by the fact that changing P_f has an overall effect of P_{O_2} at the feed side of the membrane, i.e. an increase/decrease in P_f leads to an entire shift of P_{O_2} over the feed side, while a change in f_f^o only affects P_{O_2} near the outlet of the feed side, leaving P_{O_2} at the inlet of the feed side constant.
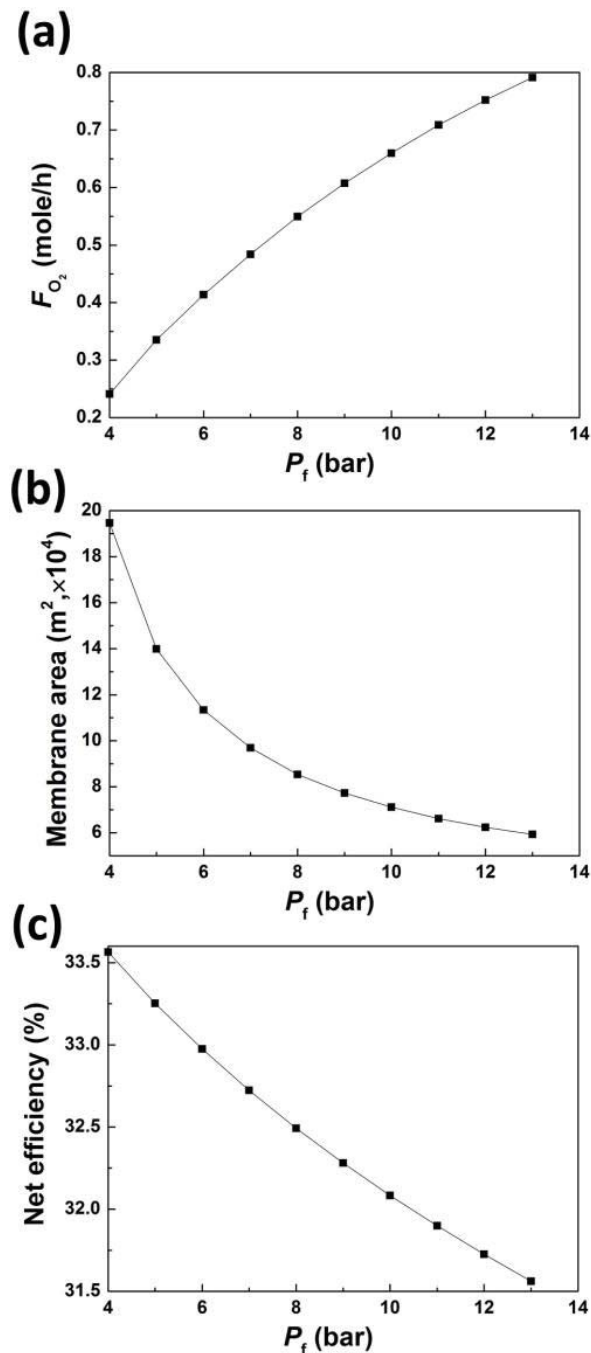
Figure 6.7. Effect of membrane feed side pressure (P_f) on: (a) Oxygen produced by one membrane tube, (b) Total membrane area need and (c) The net efficiency of the power plant.

Effect of membrane thickness

According to eq. (6.8), the oxygen flux increases when the membrane thickness decreases (assuming membrane bulk diffusion as the rate determining step for oxygen permeation), which means that more oxygen is produced by one single

membrane tube. Since the total oxygen, necessary in this study is constant, less membrane area is needed. The influence of membrane thickness on the required amount of membrane area (under 'standard' operating conditions) is shown in Figure 6.8. If the membrane thickness is reduced from 1.0 to 0.6 mm, the amount of membrane area decreases from 71,000 m^2 to 42,600 m^2. However, it should be noted that the membrane thickness cannot be reduced without limitations. This is not only because of manufacturing problems, but also because of the fragility of the membranes, which is very common for ceramics. A possible solution to this problem is to use supported thin films where a porous support is used to maintain the mechanical strength of the membrane, while a dense oxygen permeable layer/film is coated on top of it. In this way the membrane thickness can be reduced to as low as 20 μm, and the oxygen flux will be significantly increased [30, 31]. Another issue which should be mentioned in this parametric study on membrane thicknesses is that all process parameters, as given in tables 6.1 and 6.3 (i.e.: the oxygen mole fractions, f_s^i, f_f^i, f_s^o and f_f^o, and the operating pressures, P_f and P_s), are constant, which implies that F_s^i, F_f^i, F_s^o and F_f^o are also constant. Therefore, the variation in membrane thickness only affects the total amount of membrane area and not the net efficiency of the power plant.
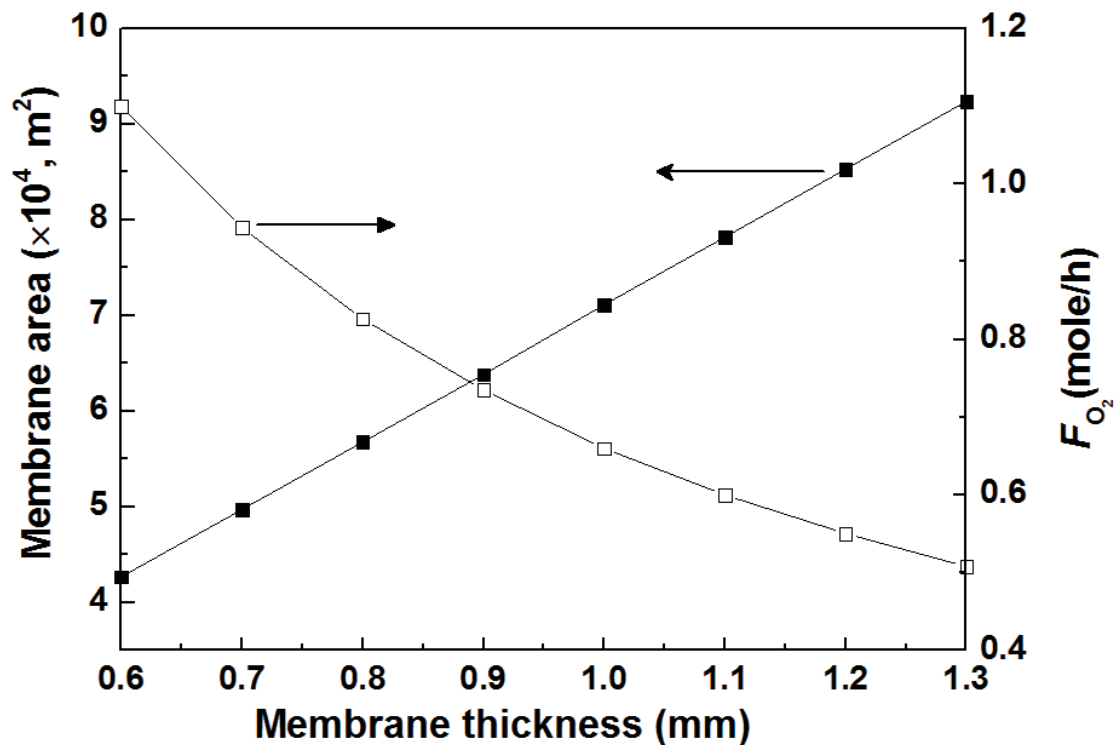
Figure 6.8. Effect of membrane thickness on the amount of oxygen produced by one single membrane tube and total needed membrane area.

6.4.6 Process modification

As discussed in chapter 4, the CO_2 resistance of high oxygen-permeable SCF membranes is largely improved by increasing P_{O_2} in the CO_2 sweep gas. Adding 5 % of oxygen in the sweep gas can protect SCF membranes from CO_2 poisoning. This observation inspired us to propose a modified process, which is shown in Figure 6.9. In this modified process undoped SCF membranes are used for air separation and an extra O_2/CO_2 loop (A18) is introduced to increase P_{O_2} in the CO_2 sweep gas (f_s^i) in order to protect the SCF membranes against CO_2 poisoning. Due to the pressure drop in the membrane module, the extra O_2/CO_2 loop has to be recompressed (COM-2) before being mixed with recycled CO_2. Since the temperature of the O_2/CO_2 mixture from the heat exchanger (HEX-2) is too high (473 ºC), the O_2/CO_2 loop has to be cooled (to 150 ºC in this study) before compression, and after the compression it is heated again to 950 ºC.
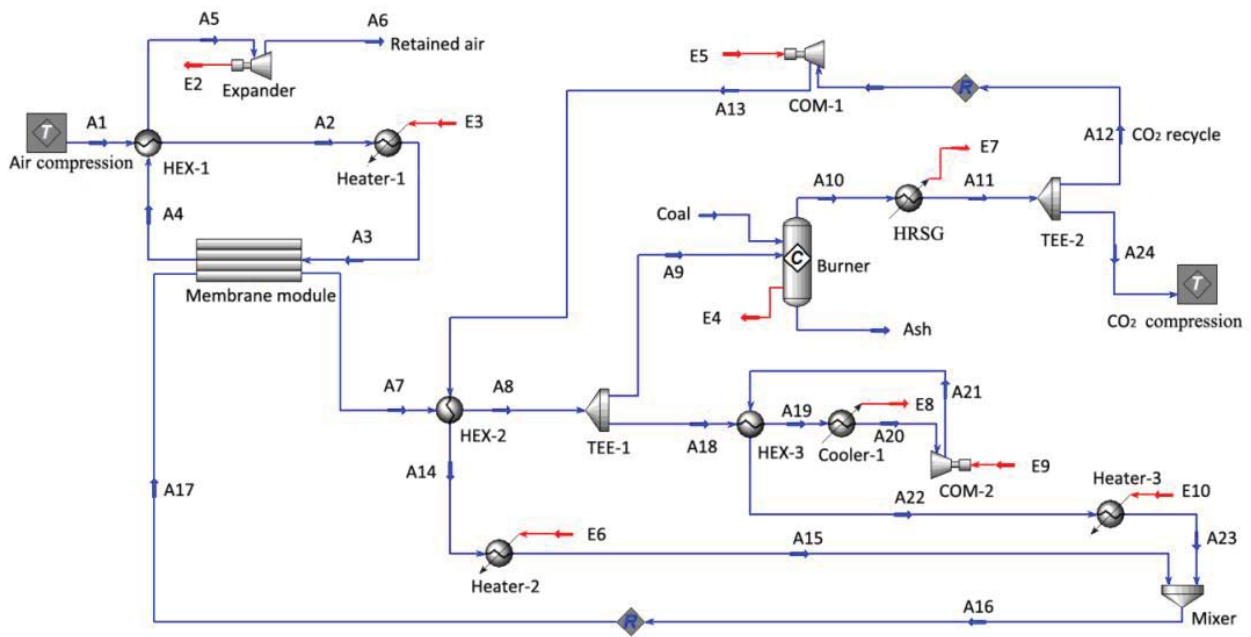
Figure 6.9. A modified membrane-integrated oxy-fuel combustion process (details about the material and power streams are given in table A6.4. in the appendix).

In this modified process the membrane geometry and operating conditions are kept constant (see table 6.1 and 6.3 except f_s^i, which latter now has a value from 0.05). The simulation results are given in table 6.5. Details about the material and power streams are given in table A6.4 of the appendix. This modified process almost has the same net efficiency (31.9 %) as the unmodified one (32.1 %). However, the required amount of membrane area in this modified process (49,000 m²) is much less than that in the unmodified one (71,000 m²), namely a reduction of more than 30 %. This is due to the fact that the SCF membrane used in the modified process has a higher oxygen permeability if compared with the Ta doped-SCF (see 6.4.1).

Table 6.5. Simulation results for the modified membrane-integrated oxy-fuel combustion process.

Variable	Value	Units
Total needed membrane area	49,000	m^2
Electric power output	58.1	MW
Net efficiency (η_m)	31.9	%
Specific energy for CO_2 capture	164	kWh_e/t_{CO_2}
Specific energy for O_2 production	111	kWh_e/t_{O_2}

6.5 Conclusion

The integration of oxygen transport membranes into the oxy-fuel combustion process can decrease the energy demand for CO_2 capture, as compared to a typical oxy-fuel combustion process where cryogenic distillation is used for oxygen production. In the present study, based on a power plant where 20 tonne/h of coal is burned for electric power generation, a net efficiency of 32.1 % is obtained for the membrane-integrated oxy-fuel combustion process (including CO_2 compression to 100 bar), which is higher than that of typical oxy-fuel combustion process (29.6 % including CO_2 compression). The required membrane area is approximately 71,000 m^2. The specific energy demand for CO_2 capture in this study is 185 kWh_e/t_{CO_2}, and the specific energy demand for O_2 production is 104 kWh_e/t_{O_2}. A modified process design is also proposed, in which higher oxygen permeable membranes (SCF) are used and an extra CO_2/O_2 loop is introduced to protect SCF from CO_2 poisoning. The modified process shows a similar net efficiency of 31.9 %, but a significantly lower amount of required membrane area (49,000 m^2).

References

[1] J.D. Figueroa, T. Fout, S. Plasynski, H. McIlvried, R.D. Srivastava, Advances in CO_2 capture technology-The U.S. Department of Energy's Carbon Sequestration Program, Int J Greenh Gas Con, 2 (2008) 9-20.

[2] B. Metz, O. Davidson, H.d. Coninck, M. Loos, L. Meyer, IPCC Special Report on Carbon Dioxide Capture and Storage, Intergovernmental Panel on Climate Change, (2005).

[3] J. Black, Cost and performance baseline for fossil energy plants. Volume 1: Bituminous coal and natural gas to electricity final report, in, National Energy Technology Laboratory, 2007, pp. 626.

[4] L. Dumée, C. Scholes, G. Stevens, S. Kentish, Purification of aqueous amine solvents used in post combustion CO_2 capture: A review, Int J Greenh Gas Con, 10 (2012) 443-455.

[5] H. Stadler, F. Beggel, M. Habermehl, B. Persigehl, R. Kneer, M. Modigell, P. Jeschke, Oxyfuel coal combustion by efficient integration of oxygen transport membranes, Int J Greenh Gas Con, 5 (2011) 7-15.

[6] J. Oexmann, C. Hensel, A. Kather, Post-combustion CO_2-capture from coal-fired power plants: Preliminary evaluation of an integrated chemical absorption process with piperazine-promoted potassium carbonate, Int J Greenh Gas Con, 2 (2008) 539-552.

[7] M.R.M. Abu-Zahra, J.P.M. Niederer, P.H.M. Feron, G.F. Versteeg, CO_2 capture from power plants: Part II. A parametric study of the economical performance based on mono-ethanolamine, Int J Greenh Gas Con, 1 (2007) 135-142.

[8] T. Wall, Y. Liu, C. Spero, L. Elliott, S. Khare, R. Rathnam, F. Zeenathal, B. Moghtaderi, B. Buhre, C. Sheng, R. Gupta, T. Yamada, K. Makino, J. Yu, An overview on oxyfuel coal combustion—State of the art research and technology development, Chemical Engineering Research and Design, 87 (2009) 1003-1016.

[9] A. Darde, R. Prabhakar, J.-P. Tranier, N. Perrin, Air separation and flue gas compression and purification units for oxy-coal combustion systems, Energy Procedia, 1 (2009) 527-534.

[10] Q. Zeng, Y.B. Zu, C.G. Fan, C.S. Chen, CO_2-tolerant oxygen separation membranes targeting CO_2 capture application, Journal of Membrane Science, 335 (2009) 140-144.

[11] W. Chen, C.-s. Chen, L. Winnubst, Ta-doped $SrCo_{0.8}Fe_{0.2}O_{3-\delta}$ membranes: Phase stability and oxygen permeation in CO_2 atmosphere, Solid State Ionics, 196 (2011) 30-33.

[12] S. Engels, F. Beggel, M. Modigell, H. Stadler, Simulation of a membrane unit for oxyfuel power plants under consideration of realistic BSCF membrane properties, Journal of Membrane Science, 359 (2010) 93-101.

[13] X. Zhu, H. Liu, Y. Cong, W. Yang, Novel dual-phase membranes for CO_2 capture via an oxyfuel route, Chem Commun, 48 (2012) 251-253.

[14] Y.Y. Wei, J. Tang, L.Y. Zhou, J. Xue, Z. Li, H.H. Wang, Oxygen separation through U-shaped hollow fiber membrane using pure CO_2 as sweep gas, Aiche J, 58 (2012) 2856-2864.

[15] Y. Wei, O. Ravkina, T. Klande, H. Wang, A. Feldhoff, Effect of CO_2 and SO_2 on oxygen permeation and microstructure of $(Pr_{0.9}La_{0.1})_2(Ni_{0.74}Cu_{0.21}Ga_{0.05})O_{4+\delta}$ membranes, Journal of Membrane Science, 429 (2013) 147-154.

[16] H. Luo, H. Jiang, T. Klande, F. Liang, Z. Cao, H. Wang, J. Caro, Rapid glycine-nitrate combustion synthesis of the CO_2-stable dual phase membrane $40Mn_{1.5}Co_{1.5}O_{4-\delta}–60Ce_{0.9}Pr_{0.1}O_{2-\delta}$ for CO_2 capture via an oxy-fuel process, Journal of Membrane Science, 423–424 (2012) 450-458.

[17] W. Li, J.J. Liu, C.S. Chen, Hollow fiber membrane of yttrium-stabilized zirconia and strontium-doped lanthanum manganite dual-phase composite for oxygen separation, Journal of Membrane Science, 340 (2009) 266-271.

[18] M. Arnold, H.H. Wang, A. Feldhoff, Influence of CO_2 on the oxygen permeation performance and the microstructure of perovskite-type $(Ba_{0.5}Sr_{0.5})(Co_{0.8}Fe_{0.2})O_{3-\delta}$ membranes, Journal of Membrane Science, 293 (2007) 44-52.

[19] R. Castillo, Thermodynamic analysis of a hard coal oxyfuel power plant with high temperature three-end membrane for air separation, Appl Energ, 88 (2011) 1480-1493.

[20] L. Chen, S.Z. Yong, A.F. Ghoniem, Oxy-fuel combustion of pulverized coal: Characterization, fundamentals, stabilization and CFD modeling, Progress in Energy and Combustion Science, 38 (2012) 156-214.

[21] E. Croiset, K. Thambimuthu, A. Palmer, Coal combustion in O_2/CO_2 mixtures compared with air, The Canadian Journal of Chemical Engineering, 78 (2000) 402-407.

[22] Z.P. Shao, W.S. Yang, Y. Cong, H. Dong, J.H. Tong, G.X. Xiong, Investigation of the permeation behavior and stability of a $Ba_{0.5}Sr_{0.5}Co_{0.8}Fe_{0.2}O_{3-\delta}$ oxygen membrane, Journal of Membrane Science, 172 (2000) 177-188.

[23] L. Qiu, T.H. Lee, L.M. Liu, Y.L. Yang, A.J. Jacobson, Oxygen Permeation Studies of $SrCo_{0.8}Fe_{0.2}O_{3-\delta}$, Solid State Ionics, 76 (1995) 321-329.

[24] H. Luo, H. Jiang, T. Klande, Z. Cao, F. Liang, H. Wang, J. Caro, Novel cobalt-free, noble metal-free oxygen-permeable $40Pr_{0.6}Sr_{0.4}FeO_{3-\delta}-60Ce_{0.9}Pr_{0.1}O_{2-\delta}$ dual-phase membrane, Chem Mater, 24 (2012) 2148-2154.

[25] W. Li, T.-F. Tian, F.-Y. Shi, Y.-S. Wang, C.-S. Chen, $Ce_{0.8}Sm_{0.2}O_{2-\delta}−La_{0.8}Sr_{0.2}MnO_{3-\delta}$ Dual-Phase Composite Hollow Fiber Membrane for Oxygen Separation, Ind Eng Chem Res, 48 (2009) 5789-5793.

[26] H.J.M. Bouwmeester, M.W. Otter, B.A. Boukamp, Oxygen transport in $La_{0.6}Sr_{0.4}Co_{1-y}Fe_yO_{3-d}$, J Solid State Electr, 8 (2004).

[27] J.F. Vente, W.G. Haije, R. Ijpelaan, F.T. Rusting, On the full-scale module design of an air

separation unit using mixed ionic electronic conducting membranes, Journal of Membrane Science, 278 (2006) 66-71.

[28] Seider, Seader, Lewin, Widagdo, Product and process design principles, Third ed., John Wiley&Sons, Inc., 2010.

[29] R.K.Sinnott, Chemical engineering design, 4 ed., Elsevier, 2005.

[30] S. Baumann, J.M. Serra, M.P. Lobera, S. Escolástico, F. Schulze-Küppers, W.A. Meulenberg, Ultrahigh oxygen permeation flux through supported $Ba_{0.5}Sr_{0.5}Co_{0.8}Fe_{0.2}O_{3-\delta}$ membranes, Journal of Membrane Science, 377 (2011) 198-205.

[31] J.M. Serra, J. Garcia-Fayos, S. Baumann, F. Schulze-Küppers, W.A. Meulenberg, Oxygen permeation through tape-cast asymmetric all-$La0.6Sr_{0.4}Co_{0.2}Fe_{0.8}O_{3-\delta}$ membranes, Journal of Membrane Science, 447 (2013) 297-305.

6.6 Appendix:

Table A6.1. Material and power streams for the coal-fired power plant without CO_2 capture (see Figure 6.2)

Material streams	Air	A1	A2	Coal	Exhaust gas
Temperature (^{o}C)	25	79	400	25	50
Pressure (bar)	1	1.7	1	1	1
Mole flow (kmole/h)	7976	7976	7976	1667	7976
Mass flow (tonne/h)	230	230	250	20	250
Power streams	**E1**	**E2**	**E3**		
(MW)	3.49	158.5	25.6		

Table A6.2. Material and power streams for the oxy-fuel combustion process with CO_2 capture (see Figure 6.3)

Material streams	A1	A2	A3	A4	A5	A6	A7	O2	Coal
Temperature (^{o}C)	40	85	373	50	50	50	50	15	25
Pressure (bar)	1	1.7	1.7	1	1	1	1	1	1.7
Mole flow (kmole/h)	4763	4763	4763	4763	1667	3096	3096	1667	1667
Mass flow (tonne/h)	190	190	210	210	73	136	136	53	20
Power streams	**E1**	**E2**	**E3**	**CO_2 compression**					
(MW)	2.2	165.4	18.6	6.11					

Table A6.3. Material and power streams for the membrane-integrated oxy-fuel combustion process (see Figure 6.5)

Material streams	A1	A2	A3	A4	A5	A6	A7	A8	A9	A10
Temperature (°C)	112	716	950	950	212	4	950	435	435	50
Pressure (bar)	10	10	10	9.99	9.99	1	1.7	1.7	1.2	1
Mole flow (kmole/h)	8659	8659	8659	6992	6992	6992	4815	4815	4815	4815
Mass flow (tonne/h)	250	250	250	196	196	196	192	192	212	212
Material streams	**A11**	**A12**	**A13**	**A14**	**A15**	**Coal**				
Temperature (°C)	50	101	850	950	50	25				
Pressure (bar)	1	1.7	1.7	1.7	1	1.2				
Mole flow (kmole/h)	3148	3148	3148	3148	1666	1659				
Mass flow (tonne/h)	138	138	138	138	73	20				
Power streams	**E2**	**E3**	**E4**	**E5**	**E6**	**E7**	**CO$_2$ compression**		**Air compression**	
(MW)	11.97	18.85	179.9	1.75	4.89	22.81	6.11		17.2	

Table A6.4. Material and power streams for the modified membrane-integrated oxy-fuel combustion process (see Figure 6.9)

Material streams	A1	A2	A3	A4	A5	A6	A7	A8	A9	A10
Temperature (°C)	112	716	950	950	212	4	950	486	486	486
Pressure (bar)	10	10	10	9.99	9.99	1	1.7	1.7	1.7	1.7
Mole flow (kmole/h)	8659	8659	8659	6992	6992	6992	5280	5280	4763	4763
Mass flow (tonne/h)	249.8	249.8	249.8	196.4	196.4	196.4	210.2	210.2	189.6	209.6
Material streams	**A11**	**A12**	**A13**	**A14**	**A15**	**A16**	**A17**	**A18**	**A19**	**A20**
Temperature (°C)	50	50	92	850	950	950	950	486	260	150
Pressure (bar)	1	1	1.7	1.7	1.7	1.7	1.7	1.7	1.695	1.695
Mole flow (kmole/h)	4763	3096	3096	3096	3096	3613	3613	517	517	517
Mass flow (tonne/h)	209.6	136.2	136.3	136.3	136.3	156.9	156.9	20.6	20.6	20.6
Material streams	**A21**	**A22**	**A23**	**A24**	**Coal**					
Temperature (°C)	150	387	950	50	25					
Pressure (bar)	1.7	1.695	1.7	1	1.7					
Mole flow (kmole/h)	517	517	517	1667	1667					
Mass flow (tonne/h)	20.6	20.6	20.6	73.4	20.0					
Power streams	**E2**	**E3**	**E4**	**E5**	**E6**	**E7**	**E8**	**E9**	**E10**	
(MW)	11.97	18.85	179.3	1.44	4.82	25.93	0.62	0.002	3.76	
Power streams	**CO₂ compression**		**Air compression**							
(MW)	6.11		17.2							

Chapter 7 Conclusions and recommendations

This thesis describes several fundamental aspects on the membrane-integrated oxy-fuel combustion process and can be divided in two parts: 1) The development and characterization of membrane materials; 2) The design, simulation and evaluation of a coal-fired power plant, coupled with a membrane module.

A simple and easy method to measure the oxygen nonstoichiometry of a perovskite material is described in chapter 2. A Computing Fluid Dynamic (CFD) model is developed in chapter 3 to describe the oxygen gradient in a commonly used oxygen permeation set-up, as used to determine the oxygen ionic conductivity of a membrane. Chapter 4 provides the development of a CO_2-stable membrane (Ta doped $SrCo_{0.8}Fe_{0.2}O_{3-\delta}$ (SCF)) as can be used for the membrane-integrated oxy-fuel combustion process. In chapter 5 it is found that the CO_2 tolerance of the SCF membrane is affected by the ambient oxygen partial pressure: mixing 5% oxygen to CO_2 can prevent the membrane from degradation. In chapter 6 of this thesis a membrane-integrated oxy-fuel combustion process is designed, and this process is simulated in Unisim for evaluation.

In this final chapter, some general conclusions are drawn from the previous chapters, and some recommendations are given for future work.

7.1 Incomplete gas mixing in a lab-scale permeation set-up

Oxygen permeation measurements are performed to determine membrane properties like the oxygen flux through a membrane at a given oxygen partial pressure gradient and the (ionic) conductivity. These measurements are usually performed in lab-scale equipment as schematically given in Figure 3.1 (Chapter 3). By varying the oxygen partial pressure (P_{O_2}) at the feed/sweep side of the membrane, it is possible to calculate the oxygen ionic conductivity using Wagner's equation (see eq.1.6 in chapter 1) [1]. However, an ideal gas mixing has to be assumed in such a permeation set-up, i.e.: the oxygen partial pressure (P_{O_2}) is homogeneous on the membrane surface and is identical with the value measured at the outlet of the set-up.

It is then assumed that the set-up functions as a Continuous Ideally Stirred Tank Reactor (CISTR). However, with the aid of a CFD model, it is found in chapter 3 that this assumption is not completely valid. The P_{O_2} on the membrane surface at the permeate is not homogeneous over the surface, while there might be also a difference between P_{O_2} as measured at the outlet of the set-up and the (average) P_{O_2} at the membrane surface. This incomplete gas mixing is affected by the set-up geometry as well as operating conditions like flow rate and type of sweep gas. It is shown that especially the type of sweep gas has great influence on the gas mixing, e.g. using helium as sweep gas results in better mixing with oxygen than argon. If using helium as sweep gas in the set-up as used in our Inorganic Membranes laboratory, there is only a slight deviation in the CISTR assumption.

Due to incomplete gas mixing, calculation of the oxygen ionic conductivity based on the P_{O_2} measured at the outlet is not accurate. A way to overcome this problem is to use a CFD model, as described in chapter 3. With this CFD model, no ideal gas mixing assumption is required, and the oxygen ionic conductivity can be obtained by fitting the experimental results.

7.2 Chemical stability of MIEC membranes in a CO_2-containing atmosphere

The chemical stability of mixed ion-electron conducting (MIEC) membranes in a CO_2-containing atmosphere is of relevance in a number of processes where CO_2 is in contact with the membrane, e.g. when these membranes are applied in a 4-end mode operation, where CO_2 is used as sweep gas. This chemical stability is affected by factors like membrane material, operation temperature and oxygen partial pressure in the CO_2-rich sweep gas.

The type of membrane material has a major effect on the chemical stability. For example, $Ba_{0.5}Sr_{0.5}Co_{0.8}Fe_{0.2}O_{3-\delta}$ (BSCF) has a very low tolerance to CO_2. The introduction of CO_2 in the sweep/feed gas causes an immediate decline in oxygen

flux [2, 3]. $La_{0.6}Sr_{0.4}Co_{0.8}Fe_{0.2}O_{3-\delta}$ (LSCF) has a relatively high CO_2 tolerance, and it is found that a stable oxygen flux is obtained when CO_2 is used as sweep gas [4, 5]. $SrCo_{0.8}Fe_{0.2}O_{3-\delta}$ (SCF) is somewhere in the middle, and using CO_2 as sweep gas leads to a slow decrease in oxygen flux [6]. So a general order of CO_2 tolerance for BSCF, SCF and LSCF is: LSCF>SCF>BSCF. However, it has also been found that the oxygen permeability of BSCF, SCF and LSCF is in reversed order of LSCF<SCF<BSCF, and it seems there is a trade-off between CO_2 tolerance and oxygen permeability. In chapter 4 it is proven that 10% Ta doping at the Co/Fe (B-) site of SCF leads to an increase in CO_2 tolerance, and a stable oxygen flux is obtained at 900 °C using CO_2 as sweep gas, although the oxygen permeability is ~30% smaller than that of the SCF membrane. It is found that the increase in the CO_2 tolerance is caused by a decrease in the Lewis basicity of the membrane, as revealed by XPS studies.

Beside the type of membrane material, the operation temperature also plays an important role on the stability of the membrane in a CO_2 atmosphere. Yi et al. reported [10] that the oxygen flux of SCF membranes decreases at 810 °C but remains almost unchanged at 900 °C when 5 % of CO_2 is introduced to the feed gas (air). In chapter 5 isothermal gravimetric analyses were performed at 900 °C, 950 °C and 1000 °C using a sweep gas containing 67 % CO_2, 10 % O_2 and 23 % nitrogen. It is found that the reaction of SCF with CO_2 is completely restrained when the temperature is raised to 1000 °C, compared to fast reactions with CO_2 at 900 °C and 950 °C. In principle, it is possible to use a MIEC membrane at a high temperature to avoid CO_2 poisoning. However, some practical problems may arise if the temperature is too high. For example, the melting temperature of BSCF is ~ 1150 °C to 1200 °C. It is better not to operate MIEC membranes at a temperature that is very close to the melting temperature of the material.

The effect of P_{O_2} on the stability of SCF membranes in a CO_2-containing atmosphere has been intensively discussed in chapter 5. It is found that the chemical

stability of the membrane in a CO_2-containing sweep gas is improved by increasing the oxygen partial pressure in the sweep gas. Long term oxygen permeation experiments, at 950 ºC, showed that mixing 5 % of oxygen into the CO_2 sweep gas effectively prevents degradation of the SCF membrane. Here it is also observed that the increase in CO_2 tolerance is due to a decrease in the Lewis basicity of the membrane, similar to the results of Ta-doped SCF as described in chapter 4. It should be noted that although the work was only focused on SCF, it is expected that similar Lewis acid/base effects on CO_2-stability are valid for other perovskite systems.

7.3 Evaluation of the membrane-integrated oxy-fuel combustion process

The integration of MIEC membranes in the oxy-fuel combustion process is evaluated in chapter 6. It is found that the integration of oxygen transport membranes decreases the energy demand for CO_2 capture, as compared to a conventional oxy-fuel combustion process where cryogenic distillation is used for oxygen production. In a case study, based on a power plant where 20 tonne/h of coal is burned for electric power generation, a net efficiency of 32.1 % is obtained for the membrane-integrated oxy-fuel combustion process (including CO_2 compression to 100 bar), which is higher than that of a conventional oxy-fuel combustion process (29.6 % including CO_2 compression). The required membrane area for the power plant is approximately 71,000 m^2 based on Ta-doped $SrCo_{0.8}Fe_{0.2}O_{3-\delta}$ membranes. The specific energy demand for CO_2 capture in this study is 185 kWh_e/t_{CO_2}, and the specific energy demand for oxygen production is 104 kWh_e/t_{O_2}. A modified process design is also proposed, in which higher oxygen permeable membranes (SCF) are used and an extra CO_2/O_2 loop is introduced to protect SCF from CO_2 poisoning. The modified process shows a similar net efficiency of 31.9 %, but a significantly lower amount of required membrane area (49,000 m^2). However, it should be noted that in the modified process, extra cost has to be spent on the heat exchangers and gas compressors (see figure 6.9).

7.4 Some recommendations for future work

Membrane stability in a SO_2-containing atmosphere

In the 4-end mode operation of membranes as used in e.g. the oxy-fuel combustion process, the permeate side of the membrane is exposed to the recycled flue gas, which mainly contains CO_2. However, depending on the fuel used and the gas purification technique applied, there might be some traces of other gases present in the flue gas which is partly recycled as a sweep gas. These species may affect the membrane performance, even at a very low concentration. An example of a strong membrane-poisoning gas is SO_2. Wei et al. [11] have reported that $(Pr_{0.9}La_{0.1})_2(Ni_{0.74}Cu_{0.21}Ga_{0.05})O_{4+\delta}$ (PLNCG) shows very high CO_2 tolerance but rather low SO_2 tolerance. The oxygen flux of a PLNCG membrane remains almost the same when the sweep gas was switched from helium to pure CO_2, however, when the sweep gas was switched to helium containing 84 ppm SO_2, the oxygen flux drops to half of its original value within 2 hours and keeps decreasing. Engels et al. [3] have also found similar results with $Sr_{0.5}Ca_{0.5}Mn_{0.8}Fe_{0.2}O_{3-\delta}$ (SCMF). SCMF shows excellent CO_2 tolerance, but when 360 ppm SO_2 is introduced in the CO_2 sweep gas, the oxygen flux is immediately stopped. In both cases, it is found that metal sulfates were formed, resulting in a membrane which is impermeable for oxygen. Since the decomposition temperature of metal sulfates is usually much higher than carbonates due to their high formation energy [12-14], SO_2 might be a more severe problem compared with CO_2. Thus, it might be of interesting to consider the 3-end mode operation for the oxy-fuel combustion process, because no sweep gas is required in such a case.

Membrane stability in a water vapor containing atmosphere

Water vapor may also exist in the recycled flue gas. Bucher et al. [15] have reported that adding ~1% water vapor to an Ar-O_2 mixture in the feed gas decreases the oxygen surface reaction rate of $La_{0.6}Sr_{0.4}Co_{0.2}Fe_{0.8}O_{3-\delta}$ by a factor of 10 at 600 °C. Similar effects has also been found for $La_{0.6}Sr_{0.4}Co_{0.8}O_{3-\delta}$ [16]. It is interpreted

that the decrease in surface reaction rate is caused by the coverage of the whole sample surface with silicon. The quartz reactor acted as a silicon source, and volatile $Si(OH)_4(g)$, which forms in humid atmospheres, was transported via the gas phase to the reactive sample surface. In practice, there are various Si-sources such as glass seals and thermal insulation in the membrane module system. For operating these membranes in water vapor containing atmospheres it is important to avoid the use SiO_2-containing materials for sealing etc.

<u>Process development for the 3-end mode</u>

The work described in this thesis is focused on the 4-end mode operation with regard to the application of the membrane in the membrane-integrated oxy-fuel process. For the 3-end mode (see Figure 1.6a) there is a less strong demand on chemical stability as compared with the 4-end mode, because the membrane is not exposed to any "poisoning" gas like CO_2 or SO_2. Although the 3-end mode might be more promising in oxy-fuel combustion process, not a lot of research has been done on the development of a process where a membrane is applied in the 3-end mode. In future, simulation experiments on the 3-end mode must be regarded as well in making an estimation of the energy requirement for oxygen production, i.e. how much energy is needed to produce 1 tonne of oxygen in such a case.

References

[1] C.H. Chen, H. Kruidhof, H.J.M. Bouwmeester, A.J. Burggraaf, Ionic conductivity of perovskite $LaCoO_3$ measured by oxygen permeation technique, Journal of Applied Electrochemistry, 27 (1997) 71-75.

[2] M. Arnold, H.H. Wang, A. Feldhoff, Influence of CO_2 on the oxygen permeation performance and the microstructure of perovskite-type $(Ba_{0.5}Sr_{0.5})(Co_{0.8}Fe_{0.2})O_{3-\delta}$ membranes, Journal of Membrane Science, 293 (2007) 44-52.

[3] S. Engels, T. Markus, M. Modigell, L. Singheiser, Oxygen permeation and stability investigations on MIEC membrane materials under operating conditions for power plant processes, Journal of Membrane Science, 370 (2011) 58-69.

[4] X. Tan, N. Liu, B. Meng, J. Sunarso, K. Zhang, S. Liu, Oxygen permeation behavior of

$La_{0.6}Sr_{0.4}Co_{0.8}Fe_{0.2}O_3$ hollow fibre membranes with highly concentrated CO_2 exposure, Journal of Membrane Science, 389 (2012) 216-222.

[5] T. Klande, O. Ravkina, A. Feldhoff, Effect of A-site lanthanum doping on the CO_2 tolerance of $SrCo_{0.8}Fe_{0.2}O_{3-\delta}$ oxygen-transporting membranes, Journal of Membrane Science, 437 (2013) 122-130.

[6] Q. Zeng, Y.B. Zu, C.G. Fan, C.S. Chen, CO_2-tolerant oxygen separation membranes targeting CO_2 capture application, Journal of Membrane Science, 335 (2009) 140-144.

[7] J.W. Stevenson, T.R. Armstrong, R.D. Carneim, L.R. Pederson, W.J. Weber, Electrochemical properties of mixed conducting perovskites $La_{1-x}M_xCo_{1-y}Fe_yO_{3-\delta}$ (M = Sr, Ba, Ca), J Electrochem Soc, 143 (1996) 2722-2729.

[8] J. Sunarso, S. Baumann, J.M. Serra, W.A. Meulenberg, S. Liu, Y.S. Lin, J.C.D. da Costa, Mixed ionic-electronic conducting (MIEC) ceramic-based membranes for oxygen separation, Journal of Membrane Science, 320 (2008) 13-41.

[9] J.A. Lane, S.J. Benson, D. Waller, J.A. Kilner, Oxygen transport in $La0.6Sr_{0.4}Co_{0.2}Fe_{0.8}O_{3-\delta}$, Solid State Ionics, 121 (1999) 201-208.

[10] J.X. Yi, S.J. Feng, Y.B. Zuo, W. Liu, C.S. Chen, Oxygen permeability and stability of $Sr_{0.95}Co_{0.8}Fe_{0.2}O_{3-\delta}$ in a CO_2- and H_2O-containing atmosphere, Chem Mater, 17 (2005) 5856-5861.

[11] Y. Wei, O. Ravkina, T. Klande, H. Wang, A. Feldhoff, Effect of CO_2 and SO_2 on oxygen permeation and microstructure of $(Pr_{0.9}La_{0.1})_2(Ni_{0.74}Cu_{0.21}Ga_{0.05})O_{4+\delta}$ membranes, Journal of Membrane Science, 429 (2013) 147-154.

[12] M.W. Nathans, W.W. Wendlandt, The thermal decomposition of the rare-earth sulphates: Thermogravimetric and differential thermal analysis studies up to 1400°C, Journal of Inorganic and Nuclear Chemistry, 24 (1962) 869-879.

[13] A.G. Ostroff, R.T. Sanderson, Thermal stability of some metal sulphates, Journal of Inorganic and Nuclear Chemistry, 9 (1959) 45-50.

[14] J.A. Poston Jr, R.V. Siriwardane, E.P. Fisher, A.L. Miltz, Thermal decomposition of the rare earth sulfates of cerium(III), cerium(IV), lanthanum(III) and samarium(III), Applied Surface Science, 214 (2003) 83-102.

[15] E. Bucher, W. Sitte, F. Klauser, E. Bertel, Oxygen exchange kinetics of $La_{0.58}Sr_{0.4}Co_{0.2}Fe_{0.8}O_3$ at 600°C in dry and humid atmospheres, Solid State Ionics, 191 (2011) 61-67.

[16] E. Bucher, W. Sitte, F. Klauser, E. Bertel, Impact of humid atmospheres on oxygen exchange properties, surface-near elemental composition, and surface morphology of $La_{0.6}Sr_{0.4}CoO_{3-\delta}$, Solid State Ionics, 208 (2012) 43-51.

Summary

Dense ceramic oxygen transport membranes (OTMs) have an infinite selectivity for oxygen because oxygen is transported in the form of ions. This feature makes it of great potential in air separation and other oxygen related processes. This thesis describes original research on OTMs, including fundamental material studies as well as process engineering design and simulation.

A general introduction is given in **chapter 1**, which includes a brief review of CO_2 capturing techniques and the basic concept of using OTMs in the oxy-fuel process of a fossil fuel fired power plant.

Chapter 2 and 3 are focused on the development of experimental and mathematical approaches for membrane characterization. In **chapter 2** a new and easy method is described to determine the oxygen non-stoichiometry of perovskite materials, which are the most commonly used materials for OTMs. The method is based on the complete decomposition of the powder to stoichiometric metal oxides and/or metal carbonates by using CO_2 as reacting gas. The oxygen non-stoichiometry is calculated from the mass change caused by this reaction. Its applicability is demonstrated by using $SrCoO_{3-\delta}$, $BaCoO_{3-\delta}$, $BaFeO_{3-\delta}$ and $BaCeO_{3-\delta}$ as representative materials.

Oxygen permeability of the OTMs is another important membrane property for oxygen transport. Analysis of the oxygen permeability of dense ceramic membranes is usually performed with a lab-scale oxygen permeation set-up where feed and sweep gas are directly flushed over the membrane surface. Due to concentration gradients within the experimental setup, the oxygen partial pressure (P_{O_2}) measured at the outlet of the set-up does not always have to be the same as the P_{O_2} on the membrane surface. This leads to an inaccurate calculation of the oxygen ionic conductivity (an intrinsic material property) of the membrane. In order to overcome

this problem, a computational fluid dynamics (CFD) model is developed and described in **Chapter 3**. In the description of this model special attention is paid to the exact oxygen partial pressures on the membrane surface at the permeate side. With this CFD model, the oxygen ionic conductivity of a selected model membrane, $SrCo_{0.8}Fe_{0.2}O_{3-\delta}$ (SCF), is calculated. In addition, the influence is studied of several set-up parameters on the oxygen partial pressure distribution in the setup such as the distance from sweep gas inlet to the membrane surface, the type of sweep gas used and the sweep gas flow rate. The following results were found:

(1) The distance from sweep gas inlet to the membrane surface affects the P_{O_2} in both radial direction and axial direction. At increasing distance the P_{O_2} on the membrane surface becomes more homogenous due to the lower sweep gas velocity at the surface, causing less convection. However, when the distance is too large, the overall P_{O_2} on the membrane surface will be much higher than that measured at the outlet of the set-up.

(2) The binary diffusion coefficient in the oxygen-sweep gas mixture has a strong influence on the concentration distribution in the setup. Higher diffusion coefficients lead to a better mixing and therefore a faster transport of the oxygen away from the membrane surface. Faster mixing leads to a more homogeneous oxygen partial pressure distribution in the setup. Helium as sweep gas gives the highest diffusion coefficient and results in the most homogeneous oxygen partial pressure distribution in the setup, if compared with gases like N_2, Ar of CO_2.

(3) A higher sweep gas flow rate decreases the overall P_{O_2} at the permeate side of the membrane, thus increasing the oxygen flux, which makes the P_{O_2} on the membrane surface less homogenous. This influence is relatively small compared with the geometry change of the setup and sweep gas composition.

The study in **Chapter 4 and 5** is focused on the development of CO_2 tolerant

membranes. CO_2 tolerance is very important in a membrane-integrated fossil fuel fired oxy-fuel combustion process, because highly concentrated CO_2 is used as sweep gas for the membrane module. **Chapter 4** describes the development of a CO_2 stable membrane, namely $Sr(Co_{0.8}Fe_{0.2})_{0.9}Ta_{0.1}O_{3-\delta}$ (SCFTa), which is derived from $SrCo_{0.8}Fe_{0.2}O_{3-\delta}$ (SCF). SCF is a high oxygen permeable membrane with very low CO_2 tolerance. The reaction between SCF and CO_2 leads to a decline in oxygen flux to 0 within 100 hours. When 10 % of Co/Fe is replaced by Ta, it is shown that the reaction between SCF and CO_2 is almost prevented. XPS analysis shows that the basicity of SCFTa is less than that of SCF, which may be contributed to the enhanced stability of SCFTa in CO_2 atmosphere. Ta^{5+} also increases the perovskite phase stability of SCF at low oxygen partial pressure ($pO_2 < 10^{-2}$ atm), which was proven by the disappearance of a strong shrinkage signal during thermal expansion measurements. In the oxygen permeation measurement, the oxygen flux of SCFTa was slightly lower than that of SCF when an air/helium gradient was applied over the membrane, but it remained almost the same when pure CO_2 was introduced as sweep gas.

A further study on the CO_2 tolerance of SCF is given in **Chapter 5**. It is found that the CO_2 tolerance of SCF improves by increasing the oxygen partial pressure in the CO_2-containing gas. Long term oxygen permeation experiments, at 950 ºC, showed that mixing 5 % of oxygen into the CO_2 sweep gas effectively prevents degradation of the SCF membrane. XPS analysis indicates that the increase in CO_2 tolerance of SCF is caused by a decrease in basicity of the material with increasing oxygen partial pressure, which is in agreement with the studies as given in chapter 4. Based on these experimental results, a modified oxy-fuel combustion process is proposed. In this process a mixture of 5% O_2 and 95% CO_2 is used instead of pure CO_2 as sweep gas. The required membrane area for operating a 50 MW coal-fired power plant is calculated based on this design, which shows that only 17 % additional membrane area is needed for oxygen production, compared to the case

where pure CO_2 is used as sweep gas. However, it should be pointed out that the latter case is not realistic, because SCF membranes are not stable in a pure CO_2 atmosphere.

Chapter 6 discusses the design of the whole process for a membrane-integrated oxy-fuel combustion process. Simulation results, using UniSim®, indicate for this process an overall net efficiency of 32.1 % for a coal-fired power plant where 20 tonne/h of coal is burned for electric power generation. This efficiency is higher than that for an oxy-fuel combustion process using oxygen from cryogenic distillation of air (29.6 %). The specific electrical energy demand for CO_2 capture in this oxy-fuel process, including oxygen production and CO_2 compression (to 100 bar), is calculated to be ~ 159 kWh_e / t_{CO_2} . The required membrane area for the power plant is approximately 71,000 m^2 based on Ta-doped $SrCo_{0.8}Fe_{0.2}O_{3-\delta}$ (SCFTa) membranes. Inspired by the results of the research as described in chapter 5, a modified process is proposed, in which un-doped SCF membranes are used for air separation and an extra O_2/CO_2 loop is introduced to protect the SCF membranes from CO_2 poisoning. This modified process shows a net efficiency of 31.9 %, which is very closed the net efficiency of unmodified process 32.1 %, but a considerably lower amount of membrane area (49,000 m^2) is necessary.

Finally, in **chapter 7**, some conclusions are made and recommendations for future research are provided. More research should be done towards: (1) membrane stability in a SO_2-containing atmosphere; (2) membrane stability in a water vapor containing atmosphere and (3) process development for a 3-end mode membrane configuration.

Samenvatting

In dit proefschrift zijn materiaalkundige studies van keramische, zuurstof selectieve, membranen beschreven en worden proces simulaties gemaakt, waarbij deze membranen gebruikt worden in het verbrandingsproces van steenkool voor elektriciteitsopwekking, geïntegreerd met CO_2 opslag. Het zuurstof transport door deze gasdichte membranen is in de vorm van zuurstof ionen. Daarom hebben deze zuurstof transport membranen (OTMs = Oxygen Transport Membranes) een oneindige selectiviteit voor zuurstof en zijn interessant voor het scheiden van zuurstof uit lucht en voor andere zuurstof gerelateerde processen.

In **hoofdstuk 1** wordt een algemene inleiding gegeven over OTMs en daarnaast wordt een kort overzicht gegeven van de verschillende methodes om CO_2 af te vangen (CO_2 capture) bij fossiele brandstof gestookte elektriciteitscentrales. Tenslotte wordt het basisconcept behandeld van het gebruik van OTMs in het "oxy-fuel process", waarbij zuurstof van lucht wordt gescheiden, voordat het de verbrandingskamer in gaat.

De **hoofdstukken 2 en 3** geven zowel experimentele als mathematische beschrijvingen voor het bepalen van de eigenschappen van de membranen. in **hoofdstuk 2** wordt een nieuwe en eenvoudige methode beschreven voor het bepalen van de afwijking (δ) van de (ideale) zuurstof stoichiometrie in de perovskiet kristalstructuur ABO_3. De methode is gebaseerd op de volledige ontleding van het perovksiet poeder (met algemene formule: $ABO_{3-\delta}$) tot het stoichiometrisch metaal oxide en/of metaal-carbonaat door deze poeders te laten reageren in CO_2. De afwijking (δ) van de (ideale) zuurstof stoichiometrie kan dan berekend worden aan de hand van de verandering van de massa ten gevolge van deze ontledingsreactie. De toepasbaarheid van deze methode voor het bepalen van δ is aangetoond door gebruik te maken van $SrCoO_{3-\delta}$, $BaCoO_{3-\delta}$, $BaFeO_{3-\delta}$ en $BaCeO_{3-\delta}$ als zijnde representatieve OTM materialen.

De zuurstof doorlaatbaarheid (permeabiliteit) van OTMs is een andere belangrijke membraan eigenschap. De zuurstof permeabiliteit van dichte keramische membranen wordt meestal bepaald in een laboratorium opstelling. Door concentratie gradiënten in een dergelijke opstelling kan er aan het oppervlak van het membraan een andere gassamenstelling zijn dan bij de uitlaat/afvoer. Dit houdt in dat de zuurstof partiaaldruk (P_{O_2}), die gemeten wordt aan de uitlaat van de opstelling niet altijd dezelfde hoeft te zijn als de P_{O_2} aan het oppervlak van het membraan. Dit resulteert in een onnauwkeurige berekening van de zuurstof ionen geleidbaarheid van het membraan, wat een belangrijke intrinsieke parameter is voor deze materialen. Voor het bepalen van concentratie gradiënten in de meetopstelling is een "Computational Fluid Dynamics" (CFD) model ontwikkeld, wat wordt beschreven in **hoofdstuk 3**. Bij het uitwerken van dit model is met name aandacht besteed aan het exact berekenen van de zuurstof partiaaldruk aan het oppervlak van de permeaat kant van het membraan. Met dit CFD model is de zuurstof ionen geleiding van het $SrCo_{0.8}Fe_{0.2}O_{3-\delta}$ (SCF) membraan berekend. Tevens is de invloed bestudeerd van verschillende aanpassingen in de meetopstelling op de concentratie gradiënt aan de permeaat kant, zoals de afstand van de inlaat van het spoelgas tot het membraan oppervlak, de gas stroom snelheid en het soort spoelgas, wat gebruikt wordt, met de volgende resultaten:

1) Bij toenemende afstand tussen spoelgas inlaat en membraan oppervlak wordt de P_{O_2} aan het membraan oppervlak meer homogeen, maar als de afstand te groot wordt, is de totale P_{O_2} aan het oppervlak veel hoger dan de gemeten zuurstof partiaaldruk aan de uitlaat van de opstelling.

2) De binaire diffusie coëfficiënt van het zuurstof-spoelgas mengsel heeft een grote invloed op de variaties van gas samenstelling in de opstelling. Hogere waarden van de diffusie coëfficiënt resulteren in een betere/snellere menging van zuurstof en

spoelgas en daardoor in een meer homogene P_{O_2} in de opstelling. Helium heeft, in vergelijking met N_2, Ar, of CO_2, de hoogste diffusie coëfficiënt en resulteert daarom in de meest homogene P_{O_2} in de opstelling.

3) Door gebruik te maken van een hogere spoelgassnelheid neemt de totale P_{O_2} aan de permeaat kant van het membraan af, waardoor ook de P_{O_2} aan het membraanoppervlak minder homogeen word. De invloed van deze procesparameter is relatief klein ten opzichte van de eerder genoemde parameters.

De studie in **hoofdstuk 4 en 5** is gericht op de ontwikkeling van membranen die stabiel zijn in een CO_2 atmosfeer. Dit is van groot belang voor het membraan-geïntegreerde oxy-fuel verbrandingsproces van fossiele brandstoffen, omdat puur CO_2, of een gasmengsel met hoge CO_2 concentratie, als spoelgas voor de membraan module wordt gebruikt. **Hoofdstuk 4** beschrijft de ontwikkeling van een CO_2 stabiele membraan, $Sr(Co_{0.8}Fe_{0.2})_{0.9}Ta_{0.1}O_{3-\delta}$ (SCFTa), wat is afgeleid van het bekende membraan materiaal $SrCo_{0.8}Fe_{0.2}O_{3-\delta}$ (SCF). SCF vertoont een hoge zuurstof permeatie, maar in een CO_2 atmosfeer neemt de permeatie snel af om na verloop van tijd (ca 100 muur) volledig zuurstof impermeabel te zijn. De reactie tussen SCF en CO_2 wordt bijna volledig tegengegaan als 10 % van het Co of Fe vervangen wordt door Ta. XPS analyse toont aan dat SCFTa minder basisch is dan SCF, waardoor het minder snel reageert met CO_2. Daarnaast verhoogt het doteren van SCF met Ta^{5+} de stabiliteit van de perovskiet kristalstructuur bij lagere zuurstof partiaaldruk ($P_{O_2} < 10^{-2}$ atm). Bij een lucht/helium gradiënt over het membraan is de zuurstof permeabiliteit van SCFTa iets lager dan die van SCF, maar de SCFTa blijft dezelfde, constante, permeabiliteit houden als CO_2 als spoelgas wordt gebruikt.

In **hoofdstuk 5** is een verdere studie uitgevoerd naar de tolerantie van SCF in een CO_2 rijke atmosfeer. Aangetoond is dat de CO_2 tolerantie van SCF beter wordt als er wat zuurstof aan het CO_2 wordt toegevoegd. Een SCF membraan blijft stabiel

wat betreft zuurstof flux inden er 5 % zuurstof aan het CO_2 spoelgas wordt toegevoegd. XPS analyses lieten zien dat de toename in CO_2 tolerantie veroorzaakt wordt doordat het SCF minder basisch is bij toenemende zuurstof partiaaldruk. Met de kennis, verkregen uit deze experimentele resultaten is een aangepast oxy-fuel verbrandingsproces voorgesteld, waarbij een mengsel van 5 % O_2 en 95 % CO_2 als spoelgas wordt gebruikt in plaas van puur CO_2. Gebaseerd op dit ontwerp is uitgerekend dat slechts 17 % extra membraan oppervlak nodig is voor zuurstof productie voor een 50 MW kolen gestookte elektriciteitscentrales in vergelijking met het gebruik van puur CO_2 als spoelgas. Er moet wel op gewezen worden dat dit laatste geval (puur CO_2 als spoelgas) niet realistisch is, omdat SCF membranen niet stabiel zijn in een 100 % CO_2 atmosfeer.

Hoofdstuk 6 bediscussieerd het volledige proces van een membraan-geïntegreerde oxy-fuel verbrandingsproces. Simulatie resultaten, met gebruik making van UniSim®, geeft voor dit proces een totale netto efficiëntie van 32.1 % voor een kolen gestookte elecriciteitscentrale waar 20 ton/uur steenkool wordt verbrand voor de opwekking van elektriciteit. Deze efficiëntie is hoger in vergelijking met een oxy-fuel proces waarbij zuurstof verkregen wordt door cryogene destillatie van lucht (29,6 %). De elektrische energie, die noodzakelijk is voor afvangen van CO_2, inclusief CO_2 compressie tot 100 bar, is berekend op 159 kWh_e / t_{CO_2}. Indien Ta-gedoteerd $SrCo_{0.8}Fe_{0.2}O_{3-\delta}$ (SCFTa) als membraan gebruikt wordt, is voor deze elektriciteitscentrale een totaal membraan oppervlak van 71.000 m^2 nodig. Geïnspireerd door de resultaten, die in hoofdstuk 5 zijn beschreven, is een alternatief proces voorgesteld waarbij niet gedoteerd SCF is gebruikt voor het scheiden van zuurstof van lucht. Hierbij is een extra lus ("loop") van O_2/CO_2 geïntroduceerd in het proces schema om de SCF membranen te beschermen tegen degradatie ten gevolge van CO_2. Dit gemodificeerde proces geeft dezelfde netto efficiënte als voor het proces zonder "loop" en met SCFTa membranen, maar er is minder membraan oppervlak nodig (49.000 m^2).

Tenslotte worden in **hoofdstuk 7** de belangrijkste conclusies samengevat en worden aanbevelingen gegeven voor toekomstig onderzoek. De belangrijkste aanbevelingen zijn, dat er meer onderzoek gedaan moet worden naar de stabiliteit van deze membraan in SO_2 en/of water bevattende atmosferen. Daarnaast zal bij een proces design ook nagegaan moeten worden wat de netto efficiëntie en het benodigde membraanoppervlak is bij gebruik making van de zogenaamde 3-end mode voor de membraan module (in plaats van de in dit proefschrift beschreven 4-end mode).

Acknowledgements

When I learnt how to complain about the Dutch weather, it is almost time to leave. Four and half years' living in Enschede, a beautiful small city in the Netherlands, has given me a lot of wonderful memories. At this moment of leaving, it is so emotional.

There are many people that have helped me in the last few years, and I want to thank all of them.

The first person I want to thank is my promotor, Arian Nijmeijer. Arian, thanks very much for giving me the opportunity to carry out the PhD research in Inorganic Membranes groups. You have given me a lot of valuable advices during my PhD research, and that really helped me a lot.

I would also like to thank Louis Winnubst, my daily supervisor, for guiding me in the research and taking care of me in all other aspects in the past few years. I still remember that the first day I arrived in the Netherlands, Louis and Shumin pick me up from the Schiphol airport, it was something like yesterday but actually 1630 days ago. Yes, 1630, what a huge number! Louis, thanks a lot.

This thesis cannot be finished without the help from my colleagues/friends in the Inorganic Membranes (IM) group. I want to thank Henny Bouwmeester for many fruitful scientific discussions in material science and electrochemistry, Nieck Benes for the discussion on process simulation, Frank Morssinkhof, Mieke Luiten-olieman, Cindy Huiskes for many technical supports. I would also like to thank all other present/left IM members, Susanne Van Rijn, Bas ten Donkelaar, Marcel ten Hove, Emiel Kappert, Tan Phung, Hammad Qureshi, Michiel Raaijmakers, Saim Saher, Cheryl Tarnadi, Patrick de Wit, Evelien Maaskant, Bo Wang, Can Aran, Chung-yul Yoo, Chunlin Song, Martin Wolf, Roland Blanch Ojea, Shumin Fang, Tingfang Tian, Weihua Zhou. I wish you all the best and we keep in touch in the future.

During the PhD research, I got a lot of help from people outside the IM group.

Part of the experiments in chapter 4 was performed in University of Science and Technology of China (USTC) with the help of Professor Chusheng Chen, the process design and simulation in chapter 6 was done with a lot of help from Dr. Louis van de ham from Sustainable Process Technology group, here I want to express my gratitude to them.

The life of living abroad becomes easier with my Chinese friends in Twente, I want to thank all of them, Lei Hui, Zhou Di, Wang Min, Liu Haiying and Zhang Chunhong, Zhu Dan, Tian Ye, Fang Shumin and Pan Yan, Zhou Weihua and He Qiwei, Zhao Yingnan and Jiayin, Ni Yunyun, Feng Xueling, Tan Lianghui, Chen Yanting and Liu Fei, Li Xiaohua, Chang Lantian and Du Ying, Zhang Yali and Zhao Jie, Sui Xiaofeng and Gao Yuying, Chen Songyue and He Yifan, Sun Chao and Han Tingting, Gang Tian and Wan Xin, Xu Lixian and Luo Hongping, Zhang Jingwei and Chen zhonghua. Thank you all, my friends, I wish you all the best for your future life.

Finally, I want to express my thanks to my family:

我要感谢父母对我的养育之恩和这么多年来对我的支持和帮助，父爱如山，母爱如水，当我有了自己的孩子之后才真正懂的这份爱。 如今常年在外，不能陪伴爸妈，只希望他们能健健康康的我便满足了。我也要感谢我的妻子岳玉梅，谢谢你辞掉国内的工作来到荷兰团聚，我们在一起已经十年了，虽然生活中也有磕磕碰碰，但是我们对彼此的爱却是永恒的。最后我要感谢我亲爱的女儿，谢谢你的到来，你给爸爸妈妈的生活中增添了无穷的欢乐，你咿咿呀呀的说话让家里热闹非凡，祝你健康快乐成长。

<div align="right">
Wei Chen

April 21, 2014

Enschede
</div>

Curriculum Vitae

Wei Chen was born in on December 19th, 1982 in Henan province, China. After the graduation from the first high school of Yancheng county in 2002, he started his study in University of Science and Technology of China (USTC), majored in material science and engineering. In 2006, he obtained his bachelor's degree in natural science, and then he continued his study/research in USTC as a master student. The master program was done with the supervision of Professor Chusheng Chen and in 2010 Wei Chen obtained the master degree in material science and engineering. From the end of 2009 he joined the Inorganic Membrane Group, as a PhD student. His research interests are: fundamental researches on solid state ionics, solid state electrochemistry; design and simulation on membrane related chemical process.